

# **NAVAL POSTGRADUATE SCHOOL MONTEREY, CALIFORNIA**



**19960517 070      THESIS**

**PARAMETRIC X-RADIATION  
FROM MOSAIC GRAPHITE:  
NEW RESULTS AND RECONCILIATION  
OF PREVIOUS EXPERIMENTS**

**by**

**James Edward Barrows**

**March, 1996**

**Thesis Advisor:**

**Xavier K. Maruyama**

**Approved for public release; distribution is unlimited.**

## REPORT DOCUMENTATION PAGE

Form Approved OMB No. 0704-0188

Public reporting burden for this collection of information is estimated to average 1 hour per response, including the time for reviewing instruction, searching existing data sources, gathering and maintaining the data needed, and completing and reviewing the collection of information. Send comments regarding this burden estimate or any other aspect of this collection of information, including suggestions for reducing this burden, to Washington Headquarters Services, Directorate for Information Operations and Reports, 1215 Jefferson Davis Highway, Suite 1204, Arlington, VA 22202-4302, and to the Office of Management and Budget, Paperwork Reduction Project (0704-0188) Washington DC 20503.

1. AGENCY USE ONLY ( <i>Leave blank</i> )	2. REPORT DATE March, 1996	3. REPORT TYPE AND DATES COVERED Master's Thesis
4. TITLE AND SUBTITLE <b>PARAMETRIC X-RADIATION FROM MOSAIC GRAPHITE: NEW RESULTS AND RECONCILIATION OF PREVIOUS EXPERIMENTS</b>		5. FUNDING NUMBERS
6. AUTHOR(S) BARROWS, JAMES E.		
7. PERFORMING ORGANIZATION NAME(S) AND ADDRESS(ES) Naval Postgraduate School Monterey CA 93943-5000		8. PERFORMING ORGANIZATION REPORT NUMBER
9. SPONSORING/MONITORING AGENCY NAME(S) AND ADDRESS(ES)		10. SPONSORING/MONITORING AGENCY REPORT NUMBER
11. SUPPLEMENTARY NOTES The views expressed in this thesis are those of the author and do not reflect the official policy or position of the Department of Defense or the U.S. Government.		
12a. DISTRIBUTION/AVAILABILITY STATEMENT Approved for public release; distribution is unlimited.		12b. DISTRIBUTION CODE
13. ABSTRACT ( <i>maximum 200 words</i> )  This thesis explores the effects of mosaic graphite on the yield of parametric x-radiation (PXR). PXR is the Bragg scattering of virtual photons associated with the Coulombic field of relativistically charged particles interacting with the atomic planes of a crystal. PXR was measured from three samples of mosaic graphite crystals with differing mosaicitics. The number of photons per electron was calibrated with the fluorescent x-ray yield from a thin silver foil backing on each of the mosaic crystals. The detector angular field of view was narrowed from previous experiments. Improvements were made in the re-analysis of previous experiments by considering the thick target effects of the x-ray absorption. Previous experiments had erroneously assumed that the calibration fluorescent targets were thin. Re-analysis of previous data using corrections for solid angle, crystal absorption factors and effective thickness resulted in yields similar to those obtained in this work.		
14. SUBJECT TERMS parametric x-radiation, mosaic spread, absorption factors		15. NUMBER OF PAGES 108
		16. PRICE CODE
17. SECURITY CLASSIFICATION OF REPORT Unclassified	18. SECURITY CLASSIFICATION OF THIS PAGE Unclassified	19. SECURITY CLASSIFICATION OF ABSTRACT Unclassified
		20. LIMITATION OF ABSTRACT UL

NSN 7540-01-280-5500

Standard Form 298 (Rev. 2-89)

Prescribed by ANSI Std. Z39-18 298-102



**Approved for public release; distribution is unlimited.**

**PARAMETRIC X-RADIATION FROM MOSAIC GRAPHITE:  
NEW RESULTS AND RECONCILIATION  
OF PREVIOUS EXPERIMENTS**

James E. Barrows  
Lieutenant, United States Navy  
B.S., University of Idaho, 1988

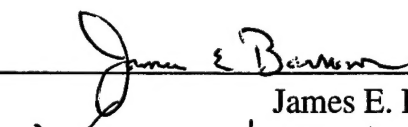
Submitted in partial fulfillment  
of the requirements for the degree of

**MASTER OF SCIENCE IN APPLIED PHYSICS**

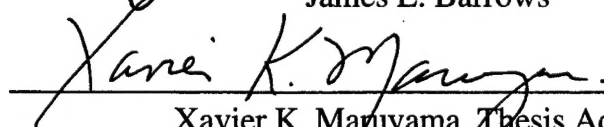
from the

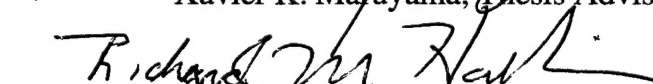
**NAVAL POSTGRADUATE SCHOOL**  
**March 1996**

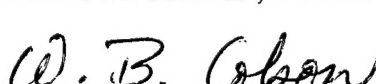
Author:

  
James E. Barrows

Approved by:

  
Xavier K. Maruyama, Thesis Advisor

  
Richard M. Harkins, Second Reader

  
William B. Colson, Chairman  
Department of Physics



## **ABSTRACT**

This thesis explores the effects of mosaic graphite on the yield of parametric x-radiation (PXR). PXR is the Bragg scattering of virtual photons associated with the Coulombic field of relativistically charged particles interacting with the atomic planes of a crystal. PXR was measured from three samples of mosaic graphite crystals with differing mosaicitics. The number of photons per electron was calibrated with the fluorescent x-ray yield from a thin silver foil backing on each of the mosaic crystals. The detector angular field of view was narrowed from previous experiments. Improvements were made in the re-analysis of previous experiments by considering the thick target effects of the x-ray absorption. Previous experiments had erroneously assumed that the calibration fluorescent targets were thin. Re-analysis of previous data using corrections for solid angle, crystal absorption factors and effective thickness resulted in yields similar to those obtained in this work.



## TABLE OF CONTENTS

I.	INTRODUCTION.....	1
II.	THEORETICAL BACKGROUND.....	3
III.	PXR EXPERIMENTAL DESCRIPTION.....	11
	A. UCAR GRAPHITE MONOCHROMATORS.....	11
	B. LINEAR ACCELERATOR.....	12
	C. EXPERIMENTAL SETUP.....	14
	D. SPECTROSCOPY ELECTRONICS.....	16
	E. SOFTWARE AND ENERGY CALIBRATION.....	18
IV.	DATA AND ANALYSIS.....	21
	A. PXR PEAK AREA DETERMINATION.....	21
	B. PXR PEAK AREA UNCERTAINTY CALCULATION.....	24
	C. PXR YIELD CALCULATION.....	25
	D. PXR INTENSITY RATIO CALCULATION.....	27
V.	DISCUSSION OF PREVIOUS RESULTS.....	55
VI.	DISCUSSION OF MOSAIC SPREAD.....	63
VII.	CONCLUSIONS AND RECOMMENDATIONS.....	65
APPENDIX A.	AVERAGE PEAK ENERGY APPROXIMATION.....	67
APPENDIX B.	TALES OF PXR MEASUREMENTS.....	69
APPENDIX C.	YIELD COMPARISON BETWEEN PREVIOUS AND CURRENT EXPERIMENTS.....	85
APPENDIX D.	TABLES OF EXPERIMENT AND THEORY INTENSITY RATIOS.....	91
LIST OF REFERENCES.....	95	
INITIAL DISTRIBUTION LIST.....	97	



## **ACKNOWLEDGMENTS**

I would like to thank all the individuals involved with this thesis. At times I thought the experiment was not producing the results I expected, but with your help and patience I was able to complete this thesis.

Don Snyder and Harold Rietdyk spent many hours operating and repairing the linear accelerator in the pursuit of data collection. I am sure they look forward to further experiments on PXR once the LINAC is repaired.

Ralph Fiorito of the Naval Surface Warfare Center and Mel Piestrup of Adelphi Technology were instrumental in making the thesis interesting and enhancing my level of knowledge on the theory of parametric x-rays.

Lastly, with sincere appreciation, I would to thank my thesis advisor X.K. Maruyama for making this thesis possible. Although I did not see much of him during the initial phase of my thesis, I was able to make up the lost time through many "brainstorming" sessions after his year long vacation in Washington, D.C. I am extremely grateful for his knowledge, understanding and support in making this thesis a very challenging and rewarding experience. I still wonder if there is sufficient shelf space available in his office for my thesis.

## I. INTRODUCTION

Parametric x-radiation (PXR) results from charged particle refraction through a crystalline material. PXR can be interpreted as the coherent Bragg scattering of virtual photons associated with the electric field of a relativistic charged particle passing through a crystal. [Ref. 1] From this process, these diffracted virtual photons appear as a uniquely shaped x-ray beam that is generated about the Bragg angle measured relative to the velocity vector of the charged particle. A polarized radiation pattern of PXR from a silicon crystal is shown in the following figure [Ref. 20]:

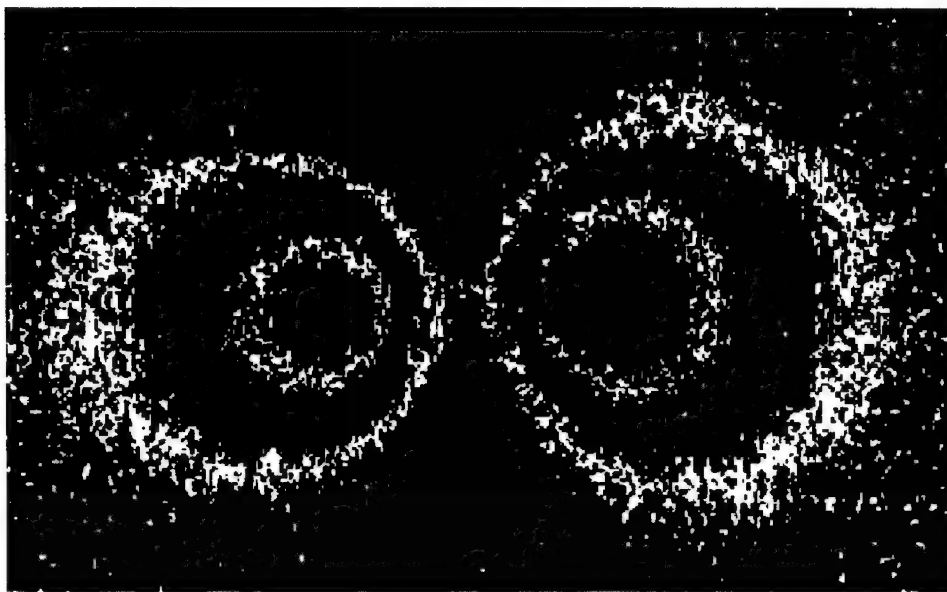


Figure 1: Polarized Radiation Pattern from 230 MeV Electrons Interacting with the (022) Planes of a 20  $\mu\text{m}$  Thick Silicon Crystal Target at a Bragg Angle of 45 Degrees

The PXR theory was developed by Ter-Mikaelian (1971) as resonant radiation that is produced in a thin crystal (absorption could be neglected). [Ref. 2] Experimental confirmation of the theory was made by Baryshevsky in 1985. [Ref. 3] Starting in the early 1990's the first PXR experiments outside of the former Soviet Union began at the

Naval Postgraduate School (NPS), Monterey, California. These experiments were conducted at the Naval Postgraduate School electron linear accelerator (LINAC) to explore the basic properties of PXR in order to assess its potential application as a compact tunable x-ray source. [Ref. 4] It has been shown that PXR is a tunable source. Rotating the target crystal, in order to change the target orientation relative to an incident 95 MeV electron beam, resulted in narrow bandwidth x-rays with multiple order energies. The type of crystal selected, Bragg angle, angular aperture and electron beam parameters determines the PXR energy, yield measurements as well as bandwidth.

Recent theoretical work on photon yields due to the influence of mosaic spread has been done by Rule et al at the Naval Warfare Center in Silver Spring, Maryland. [Ref. 5] In a perfect crystal, where mosaicity is zero, the arrangement of the atoms is identical throughout the material. Thus, the mosaic spread (or mosaicity) of a non-perfect crystal has an effect on the photon yield. The theory attempts to explain the discrepancies seen between previous experiments and theories. Initial experimental work to verify the theory was conducted by DiNova at the NPS LINAC on a thick mosaic graphite crystal with a mosaicity of 0.45 degrees. [Ref. 6] Additional experiments were conducted by Buckingham and Ivey using the same graphite crystal in addition to graphite crystals with mosaicities of 1.31 and 2.5 degrees. [Ref. 7]

For this thesis, the same three crystals were used to further explore the effects of mosaicity by narrowing the detector angular field of view and by using a silver foil backing instead of a tin foil backing on the graphite crystals. Also, corrections to previous experimental data [Ref. 6,7] were done in an attempt to reconcile the differences in apparent yield due to the experimental setups used in each experiment. A 95 MeV electron beam incident upon each of the crystals about a Bragg angle of 22.5 degrees yielded PXR radiation energies in the range of 4 to 26 keV. Analysis of the spectra from this experiment yielded unexpected results on the angular distributions and the Bragg angle coherence conditions.

## II. THEORETICAL BACKGROUND

Parametric x-radiation (PXR) is a highly directional, quasi-monochromatic, tunable, polarized and spectrally intense source of hard x-rays. PXR is generated by a relativistic charged particle interacting with a single crystal. The unique feature of PXR, compared to other radiation mechanisms, is the generation of photons at large angles relative to the incident relativistic particle direction. [Ref. 3,8] The photons are emitted from the crystal at an angle not dependent on the energy, but at an angle defined by the particle's angle relative to the crystallographic plane. When a relativistic electron ( $E \gg mc^2$ ) enters a crystal its electromagnetic field can be represented as a superposition of virtual photons. [Ref. 9] This electromagnetic interaction is equivalent to the interaction of a photon beam within a crystal, so we can use the results from the theory of x-ray diffraction. When the Bragg condition,  $2dsin\theta_B = n\lambda$ , is satisfied real photons are scattered at twice the incoming angle with respect to the crystal plane since the angle of reflection is the same as the angle of incidence,  $\theta_B$ :

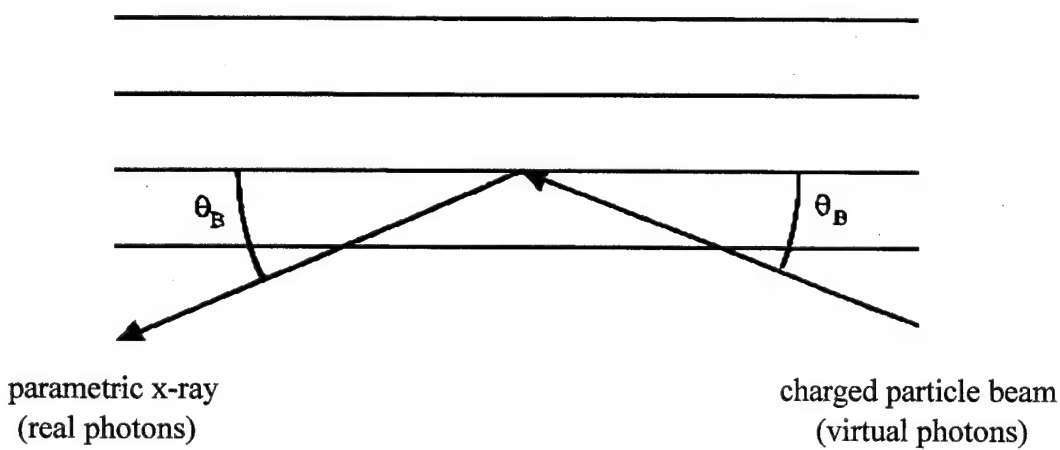


Figure 2. Parametric X-rays Produced by Diffraction of Virtual Photons by the Planes of the Crystal Lattice

The Bragg condition defines the coherence condition of the crystal that affects the production of PXR. The coherence condition of the crystal will change due to deviations (mosaic spread) from a perfect microcrystallite structure. [Ref. 4] The emitted photon energy (keV) for an ideal crystal is calculated using Bragg's Law as follows:

$$n\lambda = 2dsin\theta_B, \quad E = \frac{hc}{\lambda}, \quad (1)$$

$$\begin{aligned} E &= \frac{nhc}{2dsin\theta_B} \\ &= \frac{6.2n}{dsin\theta_B}, \end{aligned} \quad (2)$$

where,  $n$  is the spectral order,  $d$  is the interplaning spacing and  $\theta_B$  is the angle between the electron beam and the crystal plane. The second expression for Equation (2) may be used when the spacing is expressed in Angstroms with energy in units of keV.

Parametric x-radiation, as with x-ray diffraction, can be explained by dynamic or kinematic theory. The dynamic approach is used for ideal (perfect) crystals, whereas the kinematic approach is used for real crystals. Kinematic diffraction is appropriate for experimental observation of PXR and is most easily applied since the angular and spectral distributions of PXR are simplified and have a universal form for different crystals. The spectral-angular distribution for a perfect crystal is written as [Ref. 1,8]:

$$\frac{\partial^3 N}{\partial \theta_x \partial \theta_y \partial \omega} = \frac{1}{\pi^2} \cdot \frac{e^2}{\hbar c} \cdot \frac{I}{\omega_B} \cdot |\chi_{10}|^2 \cdot e^{-2M} \cdot \frac{\theta_y^2 \cos^2(2\theta_B) + \theta_x^2}{(\gamma^{-2} + \theta_x^2 + \theta_y^2 + |\chi_0|)^2} \cdot (1 - e^{-L/L_a}) \cdot \frac{I}{16 \sin^4 \theta_B (\theta_y / \tan \theta_B - \Delta \omega / \omega_B)^2 + \rho_s^2}, \quad (3)$$

where  $N$  is the number of photons per electron,  $\theta_B$  is the Bragg angle,  $\theta_x$  and  $\theta_y$  are the angular displacements away from  $\theta_B$  in and out of the incident plane respectively,  $\chi_{10}$  is the structure factor and  $\chi_0$  is the mean dielectric susceptibility.  $\gamma$  is the Lorentz factor and is equal to  $I/\sqrt{I-(v/c)^2}$ .  $e^{-2M}$  is the squared Debye-Waller factor and accounts for the increased thermal vibration of the atoms as the result of increased temperature. The frequency of the emitted photon at the Bragg condition is:  $\omega_B = n\pi c/d\sin\theta_B$ . The spectral bandwidth,  $\Delta\omega$ , is the difference between the emitted photon and  $\omega_B$ .  $L_a$  and  $L$  are the photon absorption length and path length, respectively. The factor  $\rho_S$  is defined as  $\lambda/(2\pi L_a)$ . The following paragraphs discuss the effects of multiple scattering, beam divergence, mosaicity and finite apertures.

When a virtual photon encounters the crystal atom, each electron in it scatters part of the radiation. The structure factor describes how the atom arrangement affects the scattered beam. The structure factor,  $\chi_{10}$ , is obtained by adding together all the waves scattered by the individual atoms within the unit cell [Ref. 10]:

$$\chi_{10} = \sum_I f_n e^{2\pi i(hu_n + kv_n + lw_n)}, \quad (4)$$

where  $u v w$  are the indices of a line drawn from the unit cell origin and  $h k l$  are the Miller indices which describe the orientation of the planes within a unit cell.  $f_n$  is called the atomic scattering factor and describes the amplitude of each wave. The atomic scattering factor depends on the wavelength of the incident beam and on the angle of the incident beam,  $\theta$ , with respect to the crystal face. For a fixed value of  $\theta$ ,  $f$  will be smaller for a shorter wavelength since the path differences will be larger relative to the wavelength. The result is a greater interference between the scattered beams. The atomic scattering factor is a function of  $(\sin\theta)/\lambda$  and the net effect is that  $f$  decreases as the quantity

$(\sin\theta)/\lambda$  increases. The atomic scattering factor and structure factor for the (002) planes of the mosaic graphite crystal are further discussed in Section IV. The intensity of the PXR diffracted by the atoms of the unit cell, in a direction predicted by the Bragg law, is proportional to the square of the amplitude of the resultant beam.  $|\chi_{10}|^2$  is obtained by multiplying the expression given in Equation (4) by its complex conjugate. Thus, Equation (4) is very important since it permits intensity calculations of any  $hkl$  reflection from a knowledge of the atomic positions within the crystal.

Equation (3) assumes an infinite detector aperture, which does not approximate the real conditions of the experiment, and neglects the effect of the aperture on the PXR spectrum. The spectral distribution for real experimental conditions must take into account detector size and distance from the crystal to the detector. The solid angle subtended by the detector,  $d\Omega = \Delta\theta_x \Delta\theta_y$ , where  $\Delta\theta_x$  and  $\Delta\theta_y$  are the angular fields of view in and out of the plane of observation, respectively. Also, the last term in Equation (3) can be approximated by:  $(\pi/\rho_S)\delta[\theta_y - \tan\theta_B(\Delta\omega/\omega)]$ , which correlates  $\theta_x$  and  $\Delta\omega$ , and also connects the finite aperture of the detector,  $\Delta\theta_x$ , with the observed spectral bandwidth,  $\Delta\omega$ . For the aperture limited bandwidth regime, as is the case for this thesis, the delta function approximation is still correct if  $\Delta\theta_x \gg \rho_S$ . Integrating Equation (3) over the solid angle above, with  $\Delta\theta_x$  finite and  $\Delta\theta_y$  infinite, results in a spectral distribution for the mosaic crystal and is given by [Ref. 1,4]:

$$\frac{\partial N}{\partial \omega} = \frac{2e^2}{\hbar c} \frac{|\chi_{10}|^2 e^{-2M}}{(4 \sin\theta_B \cos\theta_B)} \frac{L_a(1 - e^{IL_a})}{\lambda\omega\theta_p} J_2(\alpha_x u) S(\alpha_x - |u|), \quad (5)$$

where  $\theta_p = (\gamma^{-2} + |\chi_0|^2 + \theta_S^2)^{1/2}$  and  $\theta_S^2 = \theta_d^2 + \theta_{scat}^2 + \theta_{mos}^2$ . This is the characteristic angular spread of PXR, which approximates the effects of beam divergence, multiple scattering and mosaicity. [Ref. 1,8] The step function,  $S(\alpha_x - |u|)$ , which is unity when

the argument is positive and is zero otherwise, describes the effect of  $\Delta\theta_x$ . The function  $J_2(\alpha_x, u)$  is defined as:

$$J_2(\alpha_x, u) = \cos^2(2\theta_B)u^2 \left[ \frac{\alpha_x}{1+u^2} \frac{1}{\alpha_x^2 + 1 + u^2} + \tan^{-1} \left( \frac{\alpha_x}{(1+u^2)^{1/2}} \right) \frac{1}{(1+u^2)^{3/2}} \right] , \\ + \left[ \tan^{-1} \left( \frac{\alpha_x}{(1+u^2)^{1/2}} \right) \frac{1}{(1+u^2)^{1/2}} - \frac{\alpha_x}{(\alpha_x^2 + 1 + u^2)} \right] \quad (6)$$

with,  $\alpha_x = \theta_x/\theta_P$  and  $u = \left( \frac{\Delta\omega}{\omega} \right) \frac{\tan\theta_B}{\theta_P} = \frac{\theta_x}{\theta_P}$ .

Since the measurements described in the thesis deal with the aperture limited bandwidth regime, the spectral bandwidth,  $\Delta\omega$ , is determined by the value of  $\Delta\theta_x$  and the full width at half maximum (FWHM) of  $J_2(\alpha_x, u)$ . If  $\Delta\theta_x$  is larger than the FWHM of  $J_2(\alpha_x, u)$ , then the bandwidth is the FWHM of  $J_2(\alpha_x, u)$ . This region is called the “near field”, and there is very little finite aperture effects and most of the PXR is within the field of view of the detector,  $\Delta\theta_x$ . If  $\Delta\theta_x$  is smaller than the FWHM of  $J_2(\alpha_x, u)$ , then the bandwidth is proportional to  $\Delta\theta_x$  and is relatively insensitive to the form of  $J_2(\alpha_x, u)$ . This region is called the small aperture regime or referred to as the “far field”. The spectral bandwidth for the small aperture regime is:

$$\Delta\omega = \frac{\Delta\theta_x \omega}{\tan\theta_B} \quad (7)$$

The “far field” region is the region applicable to this thesis. Figures (3,4) illustrate the function  $J_2(\alpha_x, u)$  with  $\Delta\theta_x > \text{FWHM}$  of  $J_2(\alpha_x, u)$  for the “near field” and  $\Delta\theta_x < \text{FWHM}$  of  $J_2(\alpha_x, u)$  for the “far field” case, respectively.

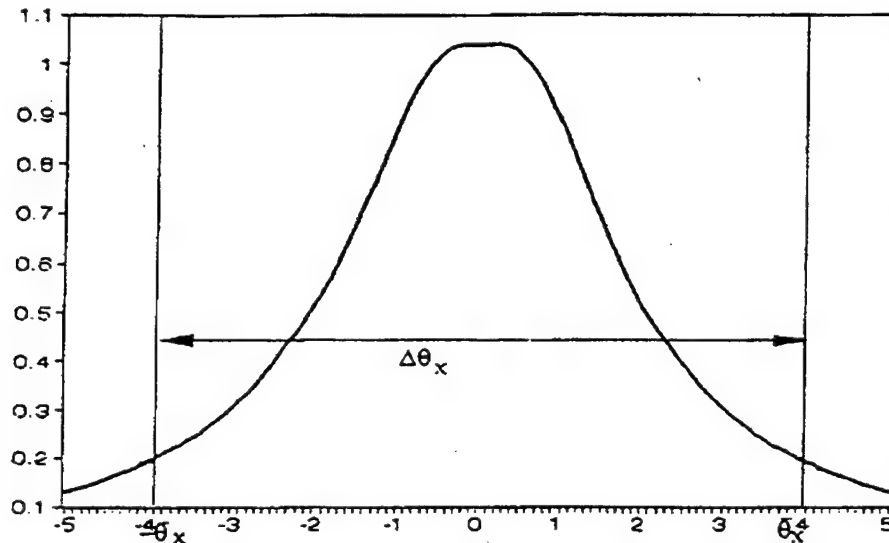


Figure 3. Near Field Case

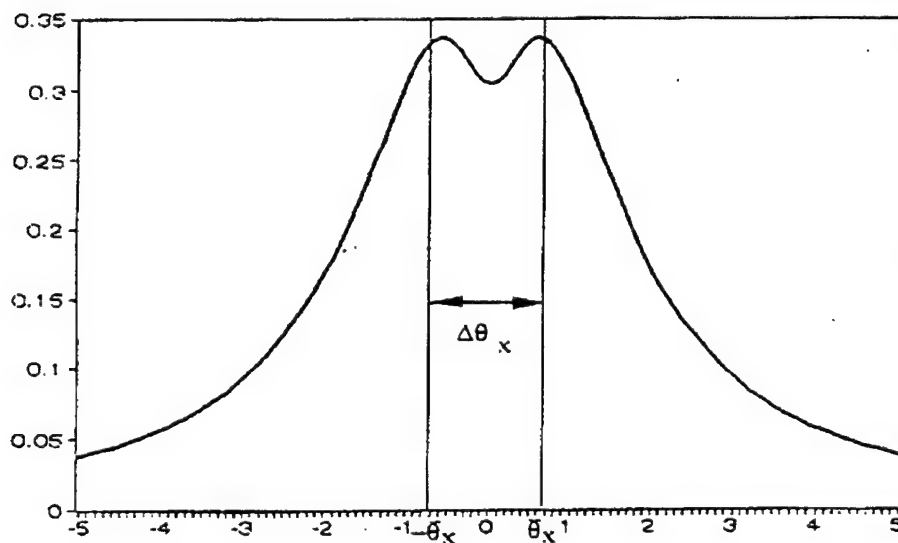


Figure 4. Far Field Case

The angular distribution of emitted photons can be derived by integrating Equation (3) over  $\omega$  [Ref. 1,8], with the following result:

$$\frac{\partial^2 N}{\partial \theta_x \partial \theta_y} = \sum_{n=1}^{\infty} \frac{e^2}{4\pi} \omega_B^{(n)} L_a \left( 1 - e^{-L/L_a} \right) \frac{|\chi_{10}|^2 e^{-2M}}{\sin^2 \theta_B} \frac{\theta_y^2 \cos^2(2\theta_B) + \theta_x^2}{(\theta_x^2 + \theta_y^2 + \theta_P^2)^2}, \quad (8)$$

This can be put into dimensionless form by means of the normalized amplitude  $J = N/N_0$  and  $\alpha_{x,y} = \Delta\theta_{x,y}/\theta_P$ :

$$\frac{\partial^2 N}{\partial x \partial y} = N_0 J(x, y), \quad J(x, y) = \frac{y^2 \cos^2 2\theta_B + x^2}{(x^2 + y^2 + 1)^2}, \quad (9)$$

$$N_0 = \sum_{n=1}^{\infty} \frac{e^2}{4\pi} \frac{\omega_B^{(n)}}{c} L_a \left( 1 - e^{-L/L_a} \right) \frac{|\chi_{10}|^2 e^{-2M}}{\sin^2 \theta_B} \quad (10)$$

The number of photons detected in an angular width of  $\theta_D$  about  $\theta_B$  is defined by the following [Ref. 8]:

$$\begin{aligned} N_D &= \pi N_0 \left( 1 + \cos^2 2\theta_B \right) \int_0^{\rho_D} \frac{\rho^3 d\rho}{(\rho + 1)^2} \\ &= N_0 \left( 1 + \cos^2 2\theta_B \right) \left( \ln \frac{\theta_D^2 + \theta_P^2}{\theta_P^2} - \frac{\theta_D^2}{\theta_D^2 + \theta_P^2} \right) \end{aligned} \quad (11)$$

$$\text{where, } \rho_D = \frac{\theta_D}{\theta_P}.$$

The value of  $N_D$  depends on the detector angular size even for  $\theta_D \gg \theta_P$ . This does not occur in channeling or Bremsstrahlung radiation. However, this circumstance is conditioned by the slow decrease  $\approx \theta^{-1}$  of the PXR intensity.



### **III. PXR EXPERIMENTAL DESCRIPTION**

Several parametric x-radiation measurements were made using three separate targets of pyrolytic graphite with differing mosaicities. The Naval Postgraduate School Linear Accelerator (LINAC) was used to produce electron beam energies of approximately 95 MeV. Initial energy calibration was performed using three fluorescent x-ray sources, copper (Cu), tin (Sn) and yttrium (Y). The PXR yield (photons per electron) was obtained by simultaneously monitoring the x-ray fluorescence from a silver foil, placed directly behind the mosaic crystal, which was used to determine the LINAC current. The PXR observation angle was set at 45 degrees with respect to the electron beam direction and the detector was placed 100 centimeters from the target. The detector angular field of view was narrowed from previous experiments to 1 mrad to enhance the angular resolution of PXR. This configuration corresponded to a Bragg angle of 22.5 degrees with respect to the (002) atomic planes of the crystals. Each crystal was rotated about the nominal Bragg Angle in small incremental angles in the range 20.5° to 24.25°. The photon yields of the spectral orders at each angle were obtained to generate “rocking curves” for each crystal. This allowed for comparison of the  $n^{\text{th}}$  order peaks between each crystal and showed the yield dependence of the various order x-rays when the Bragg condition was not satisfied.

#### **A. UCAR GRAPHITE MONOCHROMATORS**

The mosaic crystals used in this experiment are known as Union Carbide (UCAR) Graphite Monochromators. [Ref. 11] These monochromators are highly oriented forms of high purity, pyrolytic graphite which diffract x-rays with greater efficiency than any other material. In x-ray analysis, intensity is increased 3 to 15 times over that obtained with conventionally used crystals such as the lithium fluoride. Mosaic spread is defined as the half maximum height peak width of the Cu-K $\alpha$  rocking curve and is measured in degrees. In perfect crystals, where mosaicity is zero, the periodic structure of the

crystal is such that the placement of the atoms and the spacing between crystal planes are equal throughout the material. The mosaic graphite crystals used in this experiment were the ZYA, ZYD and ZYH grades. The mosaic spread specifications were  $0.4 \pm 0.1^\circ$ ,  $1.2 \pm 0.2^\circ$  and  $3.5 \pm 1.5^\circ$ . The tolerances were quite large, so the crystals were sent to the Naval Surface Warfare Center (NSWC) for determination of the actual mosaic spreads. Buckingham and Ivey's thesis [Ref. 7] contain the x-ray diffraction curves used to determine the actual spreads. The resulting spreads were  $0.45^\circ$ ,  $1.31^\circ$  and  $2.5^\circ$  for the ZYA, ZYD and ZYH crystals, respectively. Other than the mosaic spread differences, each of the crystals have identical properties. The (002) reflecting plane spacing is  $3.357 \pm 0.002$  Angstroms and the crystal density is  $2.260 \pm 0.005$  grams per cubic centimeter. [Ref. 11] The measured thicknesses of each crystal are  $0.1389 \pm 0.0001$  cm,  $0.1659 \pm 0.0001$  cm and  $0.1789 \pm 0.0001$  cm for the ZYA, ZYD and ZYH crystals, respectively.

[Ref. 7]

## B. LINEAR ACCELERATOR

The Naval Postgraduate School LINAC is shown on the next page in Figure (5). Operation of the LINAC took place in the control room and remote cameras were used in the end station to assist in obtaining desired electron beam alignment. The accelerator portion consists of three ten foot sections, each with a separate klystron connected by waveguides. Acceleration of dark current electrons to energies of approximately 95 MeV took place in the accelerator section. Dark current refers to using the LINAC with zero gun grid voltage, so that only stray electrons are accelerated. The accelerated electron beam is steered by a series of electro-magnets into the vacuum target chamber. The target chamber houses a vertically positionable ladder and dual axis goniometer. This arrangement was used to hold and orient the mosaic crystals. The LINAC is operated at 2856 Mhz with a pulse repetition rate of 60 Hz. The beam pulse length is

approximately 1  $\mu$ sec. Thus, the LINAC duty cycle requires the ability to count at 60 Mhz with a single photon being detected during each LINAC pulse. [Ref. 6]

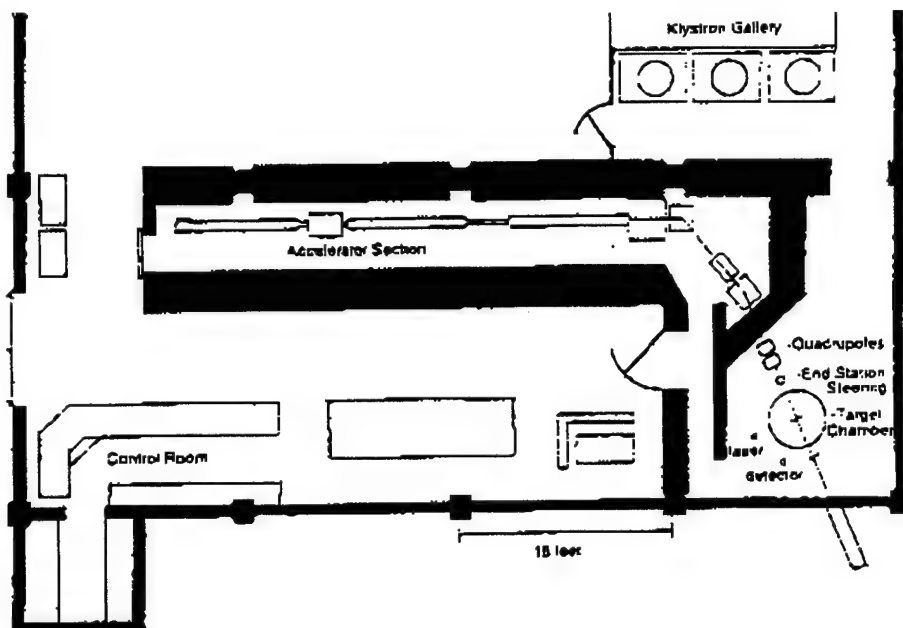


Figure 5. Naval Postgraduate School Linear Accelerator Showing Klystrons, Quadrupole Magnets and End Station Steering Magnets

The detector used was the Canberra Si(Li) model SI200250, which has a nominal resolution time of 12  $\mu$ sec, so the LINAC was adjusted to limit the average count rate including background to one count per three to five machine pulses. By limiting the LINAC beam to dark current double counting by the detector could be avoided. In other words, if two photons were stopped by the detector at the same time (within the peak shaping time of the detector) then the result would appear to be a single photon with an energy equivalent to the sum of the two coincident photons. This is of concern since PXR peaks are integral multiples of one another with respect to energy and could result in erroneous results of the higher order peaks. Maintaining a constant dark current was difficult and required attentive operators.

### C. EXPERIMENTAL SETUP

The vacuum target chamber housed the target ladder to which the three crystals, a phosphorescent screen with a copper foil backing and sandwiched Sn-Y foils were attached in a vertical coplanar arrangement. The Cu and Sn-Y foils were used for energy calibration purposes (discussed in part E.). The phosphorescent screen contained a pin hole in the center which was used to position the electron beam. The target ladder could be raised, lowered, rotated and tilted to position the crystals to the desired geometry. A 0.0052 inch silver foil backing was placed on each mosaic graphite crystal to determine LINAC beam current (discussed in IV.C.). Previous experiments [Ref. 6,7] used a tin foil backing in which the  $K_{\alpha}$  line at 25.27 keV overlapped the fifth spectral order line of the PXR. This led to errors in determining beam current. Figure (6) shows the experimental setup:

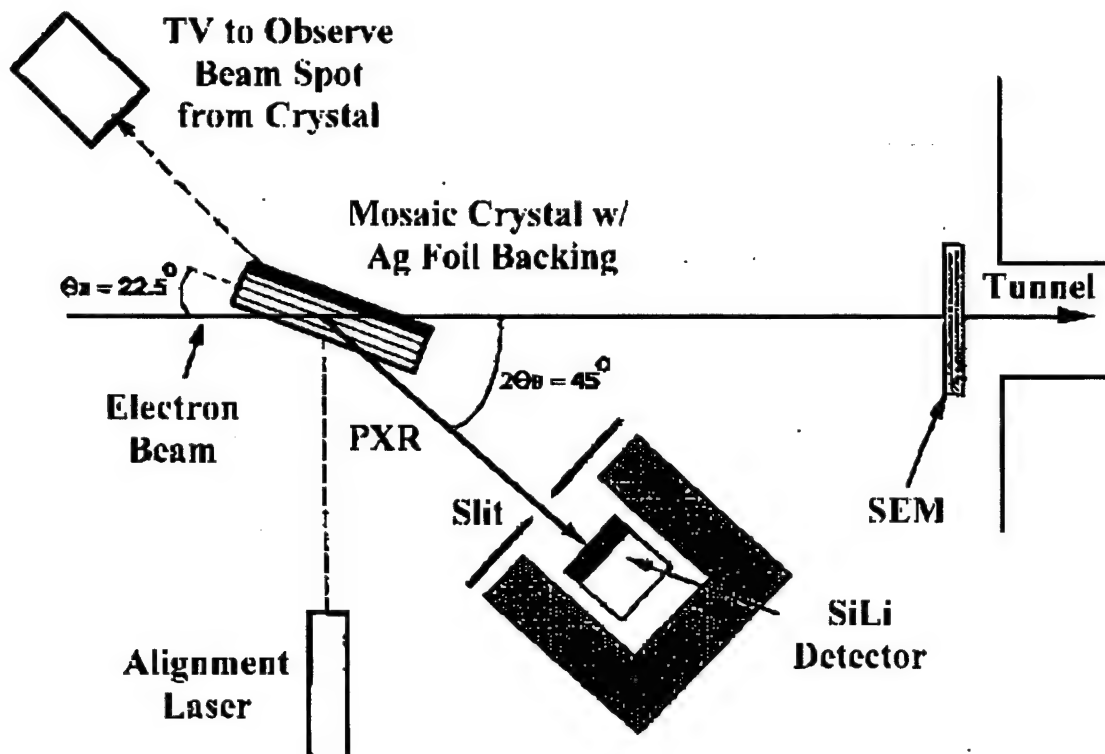


Figure 6. PXR Experimental Setup in the LINAC End Station

The alignment laser was used to establish the orientation and position of the crystal with respect to electron beam. The alignment laser was initially adjusted so that it went through the geometric center of the chamber. The ladder was then positioned so that the laser was able to pass through the pin hole in the phosphorescent screen and remain within the pin hole upon rotation of the ladder through 360 degrees. Since the crystals and phosphorescent screen were coplanar it was assured the electron beam would remain in the same position on the crystal as the ladder was rotated. The laser also established a zero degrees or "home" position by the reflection of the laser back onto itself from the face of each of the crystals. The sharpness of the reflected laser was very dependent on the mosaicity of the crystal. The ZYH crystal returned a very diffuse reflection which made it hard to determine the zero position, whereas the ZYA had a very focused reflection and the "home" position was easily determined.

The electron beam was adjusted so that it passed through the center of the quadrupole magnets, so that adjustments in klystron frequency and phase during the experiment would not affect the location of the beam on the crystal. Use of the end station steering magnets positioned the electron beam through the pin hole in the phosphorescent screen.

The Si(Li) detector was placed on the 45 degree viewing port. The Bragg condition for this position was 22.5 degrees. The crystal was initially positioned perpendicular to the laser ("home" position) and then rotated clockwise to 22.5 degrees. Data was collected at this position and then the crystal was rotated counter-clockwise to 20.5 degrees where data was collected again. Subsequent readings were collected at 21.0, 21.5, 22.0, 22.25, 22.75, 23.25, 23.75 and 24.25 degrees by rotating the crystal clockwise. The same procedure was used for the remaining crystals.

A measured 1 mm wide slit was placed in front of the Si(Li) detector to narrow the angular field of view of the detector to 1 mrad. This was to allow for better angular resolution of the PXR from prior experiments. DiNova's [Ref. 6] far field case and near field case had angular field of views of 16 mrad and 55 mrad., respectively. Buckingham and Ivey's [Ref. 7] near field case had an angular field of view of approximately 23 mrad.

The peak energy cones for the PXR with respect to the horizontal plane are located at a peak angle, which is equal to  $\gamma^{-1}$ , of approximately 5.4 mrad (for a 95 MeV electron beam). [Ref. 19] The 0.5 degree step size, used to obtain “rocking curves” in the previous experiments, effectively swept large fields of view over the detector washing out the details of the PXR distribution.

#### D. SPECTROSCOPY ELECTRONICS

The end station was close enough to the klystrons such that the Si(Li) detector was susceptible to ground loops and radiated noise from the klystrons. Lead bricks were used around the Si(Li) detector to reduce background radiation and the end station was enclosed in a metal mesh cage to reduce the interference of radiated noises. In addition, a gating system was established and the electronics setup is shown in Figure (7). All of the system components were located in the control room with the exception of detector and amplifier.

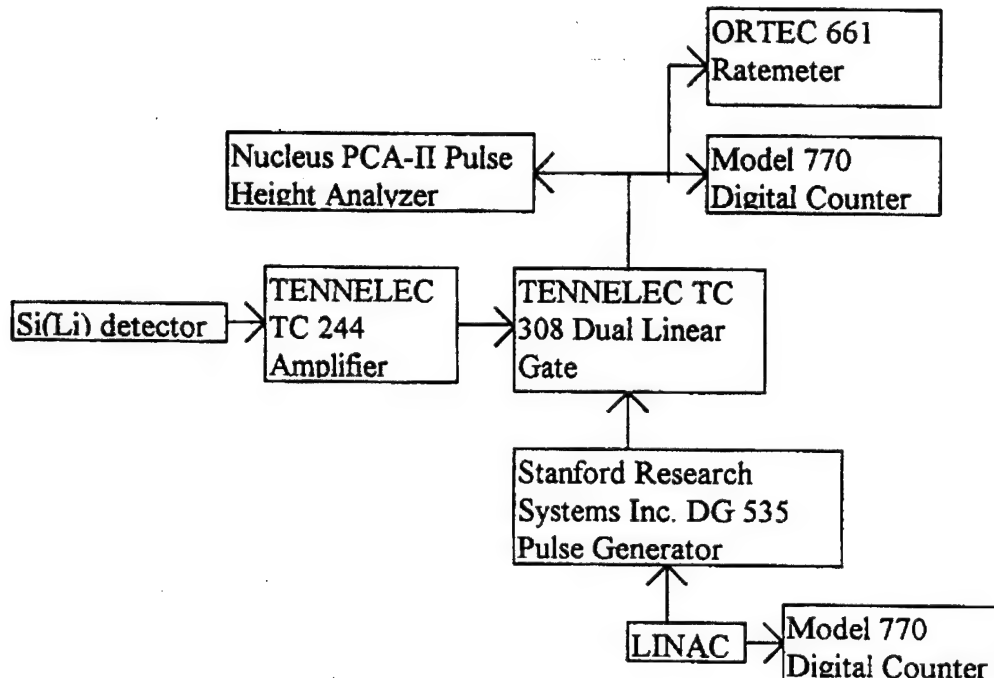


Figure 7. Electronics Setup

The Si(Li) detector signal was sent to the Tennelec TC 244 amplifier. The Tennelec TC 308 dual linear gate reduced undesired signals by providing a 25  $\mu$ sec gate during which the desired signal could be received. This effectively made the system only active during the LINAC machine pulse. The dual linear gate was triggered by the Stanford Research Systems DG 535 pulse generator. Introduction of a delay time with respect to the LINAC's start sequence time adjusted the gate to coincide with the arrival of the beam pulse. The ideal delay time for the gating was determined by using an oscilloscope along with the Pulse Height Analyzer (PHA) and the fluorescent signal from Sn-Y foils. The delay time was determined to be the time at which maximum signal was observed. Shorter and longer delay times resulted in no signal.

Klystron noise on the signal affects the energy calibration and the noise varies day to day. The klystron RF noise adds negative bias to the pulse signal energy calibration which tends to be non-random with respect to LINAC's start sequence time, thus shifting the energy calibration to that obtained using radioactive sources. The klystron noise was typically in the negative voltage portion during the system gating as shown in Figure (8):

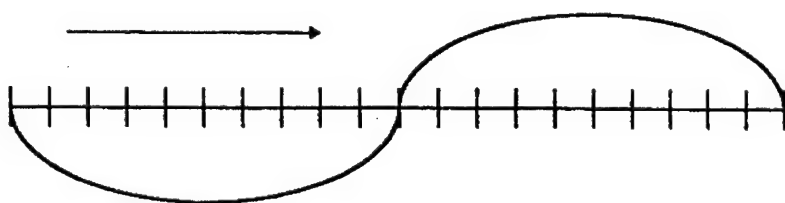


Figure 8. Typical Shape of Klystron Noise during PXR Data Collection. The Arrow Indicates the Approximated Gated Portion

This negative signal is added to the positive voltage of the detected PXR, thus reducing the output voltage. Since the PHA determines the channel (or energy) based on the energy deposited in the active detector region the lower pulse height is interpreted by the PHA as a lower photon energy. For this reason the calibration must be obtained during

the same portion of the machine cycle as the PXR spectrum to get the same klystron noise effect for both PXR and calibration fluorescent x-rays. Thus, calibration spectra were taken prior to each day's data run using known fluorescent lines of Cu, Sn and Y to eliminate this source of error.

## E. SOFTWARE AND ENERGY CALIBRATION

The PCA-II Pulse Height Analyzer software [Ref. 12] was used to record the number of counts per channel detected. The spectrum was divided into 2048 channels and prior to each day's experiment an energy calibration spectrum was obtained by measuring the x-ray fluorescence from the Cu and Sn-Y foils. Figure (9) is an example of the calibration spectrum of the Y, Cu and Sn K<sub>α</sub> peaks:

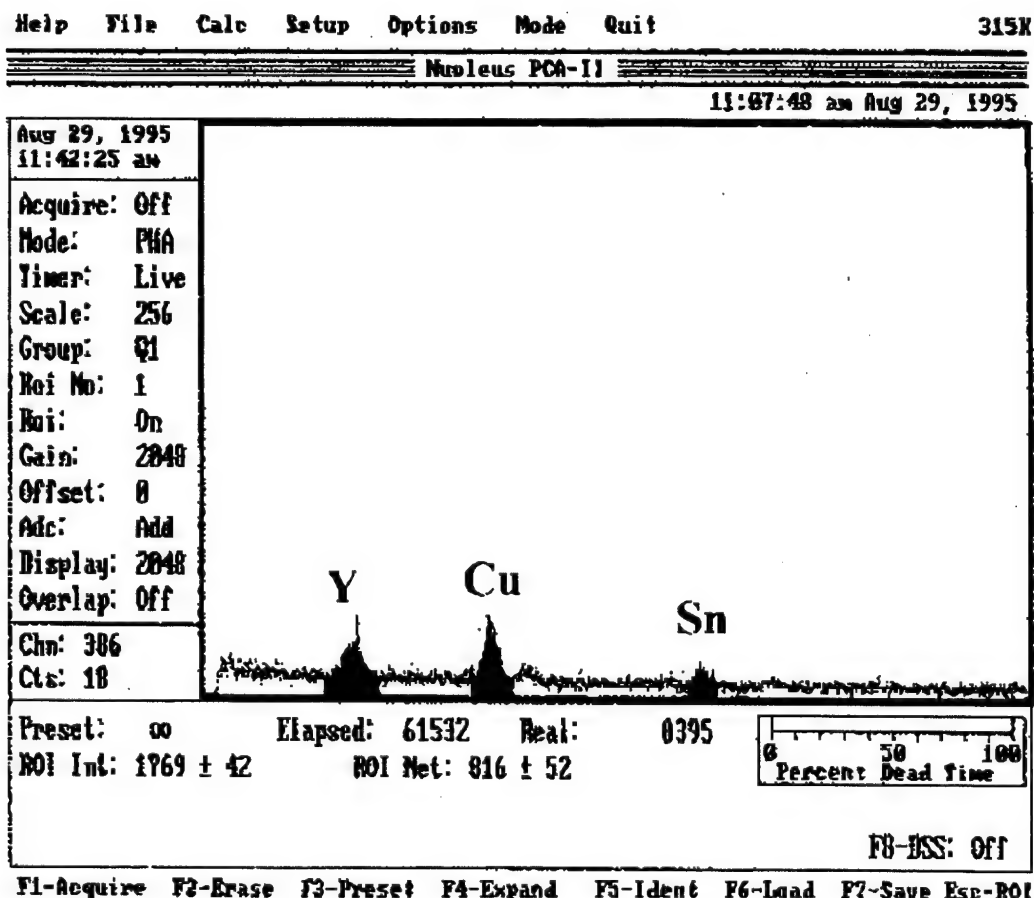


Figure (9). PCA-II PHA Software Calibration Spectra

The LINAC was operated at full gun grid voltage and the electron beam was made to strike the sandwiched foils of Sn and Y and the Cu foil on the phosphorescent screen to observe the  $K_{\alpha}$  fluorescent lines at 25.27 keV, 14.96 keV and 8.04 keV, respectively. The calibration was obtained using the centroid channel for each of the fluorescent peaks. The PCA-II PHA software determined the relationship between channel position and energy and with the following equation:

$$E(\text{keV}) = a_0 + a_1(\text{channel}) + a_2(\text{channel})^2, \quad (12)$$

where,  $a_0$ ,  $a_1$  and  $a_2$  are constants determined by performing Gaussian fits of the counts received in each region of interest, selected by the operator, surrounding the Cu, Sn and Y peaks. The values of these constants and whether all were used changed daily with each calibration due to variances in the equipment. The energy calibration was verified by ensuring the Ag  $K_{\alpha}$  line near 22.16 keV appeared on the crystal spectrum. Figure (10), shown on the next page, is an example of a crystal spectrum showing the PXR integral spectral orders and the Ag  $K_{\alpha}$  peak. The last peak, which is not highlighted, in the figure is an overlapped peak composed of the 5<sup>th</sup> spectral order of the PXR and the silver  $K_{\beta}$  line. The results of the spectrum were saved as ASCII files for further analysis. These analysis are described in greater detail in following sections of this thesis.

Help File Calc Setup Options Mode Quit

325K

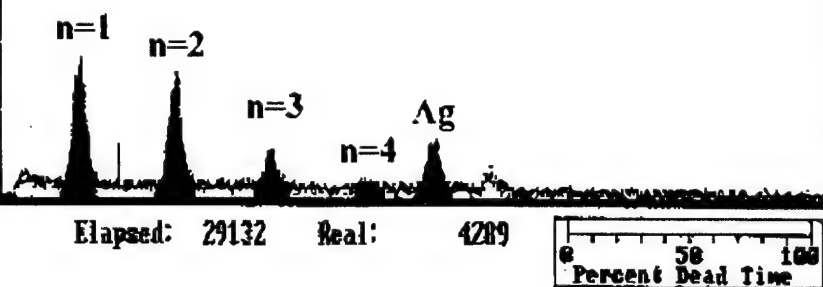
Nucleus PCA-11

Id: zya2225.spm

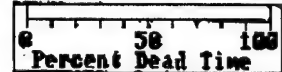
12:34:45 pm Aug 29, 1995

Aug 29, 1995  
4:18:56 pm

Acquire: Off  
Mode: PHA  
Timer: Live  
Scale: 256  
Group: Q1  
Roi No: None  
Roi: On  
Gain: 2048  
Offset: 0  
Adc: Add  
Display: 2048  
Cm: 292  
keV: 6.39  
Cts: 5



Preset: on Elapsed: 29132 Real: 4289



Filename: a:zya2225.spm

F8-DSS: Off

ROI: F9-Start F10-End Alt R-On/Off Del-Clear Alt F9-Set Colors Esc-Main

Figure (10). ZYA Crystal Spectrum at 22.25°

## IV. DATA AND ANALYSIS

ASCII format data was collected from the Si(Li) detector using the Pulse Height Analyzer PCA-II software. The raw data spectra for the Cu-Sn-Y calibration and the ZYA, ZYD and ZYH crystals at each of the angles listed in the previous section was imported into a spectrum analyzing program called PeakFit v3.0. [Ref. 13] The net areas with uncertainties of the PXR spectral order peaks and the silver peak were determined and then corrected for attenuation losses using Photcoef. [Ref. 14] The corrected net peak areas were then used to calculate the yield (number of photons per electron) and the intensity ratios between the spectral order peaks.

### A. PXR PEAK AREA DETERMINATION

PeakFit was used to remove the background noise and produce a Gaussian fit for each peak in the spectrum. An example of the peakfit for the raw calibration data is shown in Figure (11). The Gaussian fit was chosen since it gave the best fit to the raw data. The background and curve-fit parameters with uncertainties were generated by the program. The energy calibration, correlating channels to energies in keV, from the peakfit was calculated in the same manner as discussed previously. The calibration equation for a three peak fit (Cu, Sn and Y) of Figure (11) was found to be:

$$E(\text{keV}) = 0.7244 + 0.0194 \cdot (\text{Channel}). \quad (13)$$

The  $a_2$  coefficient of Equation (12) was negligible. This equation was used to calculate the peak centroid energies for the crystal spectrums following the calibration. The centroid channels were taken from the curve fits of the crystal and the energies were easily calculated. Figure (12) is an example of a peak fit, following the calibration in Figure (11), of the ZYD crystal at an angle of 22.5°. The values obtained for the  $n=1$ ,  $n=2$ ,  $n=3$ ,  $n=4$  and silver peaks were 4.67, 9.39, 14.13, 18.90 and 21.80 keV, respectively.

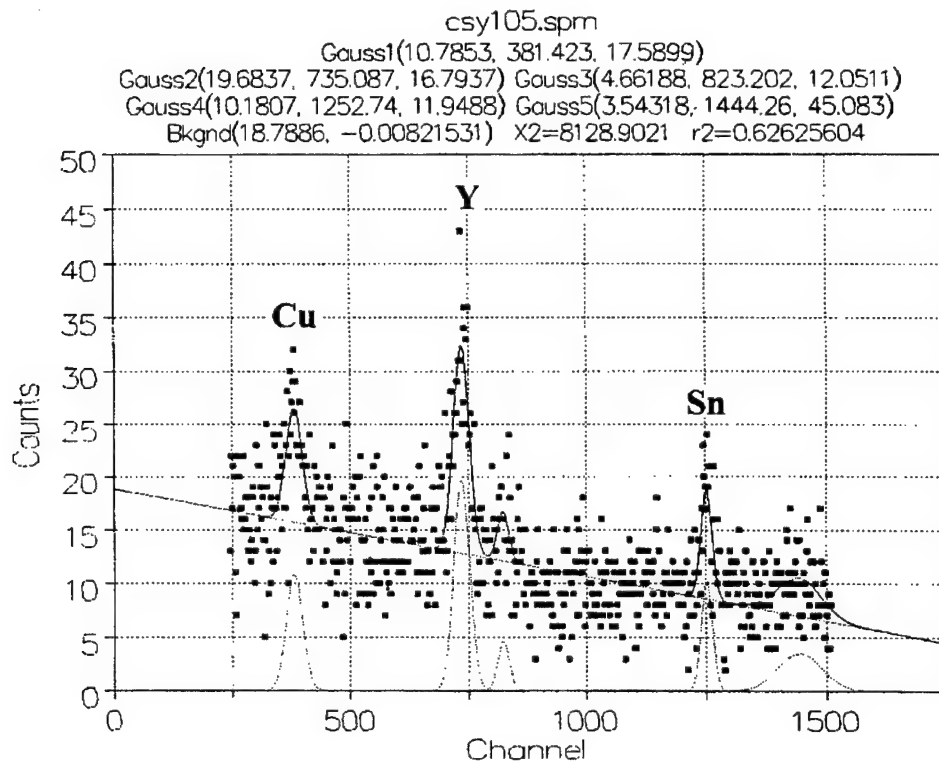


Figure (11). PeakFit Spectrum of Cu-Sn-Y Raw Data

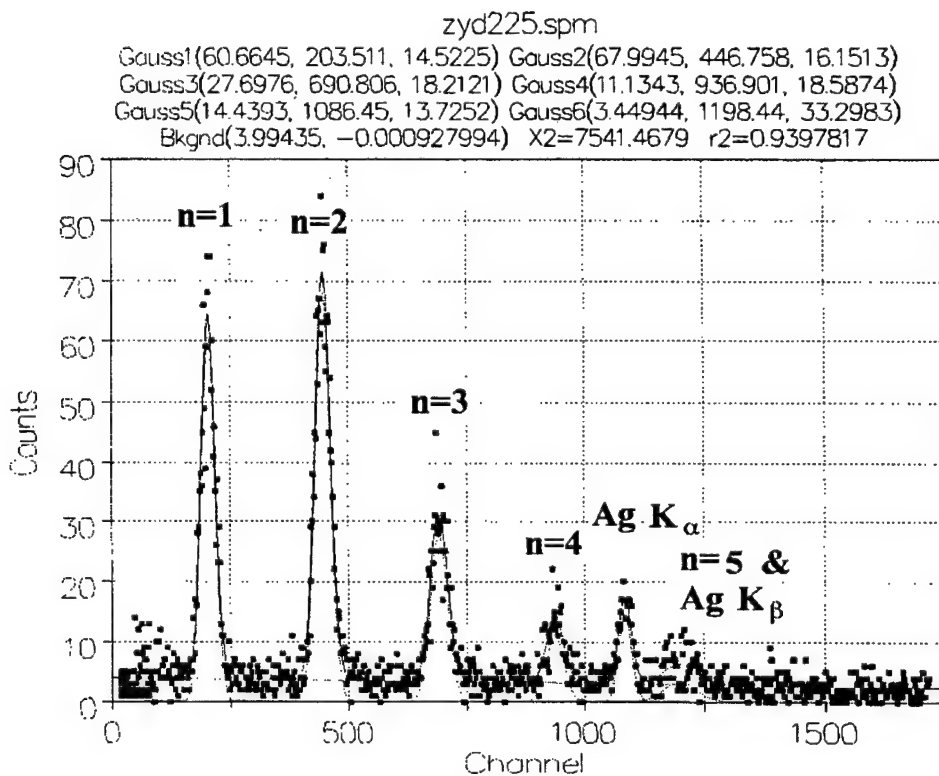


Figure (12). PeakFit Spectrum of ZYD Crystal Raw Data

Figure (11) shows two other peaks near the Y and Sn K <sub>$\alpha$</sub>  lines. These are the Y and Sn K <sub>$\beta$</sub>  lines at 16.7 keV and 28.5 keV, respectively. Also note in Figure (12) the spectral orders roughly follow integral multiples of one another and that the silver peak energy is near to the expected K <sub>$\alpha$</sub>  line at 22.16 keV. Also, the last peak is the overlap of the PXR fifth spectral order line and the silver K <sub>$\beta$</sub>  line. The theoretical Bragg Energy using Equation (2) results in a value of 4.83 keV for the first spectral order which is higher than the observed value obtained using Equation (12). These discrepancies can be attributed to several factors such as determination of the “home” position (see previous section for discussion), errors associated with the PeakFit program and inherent instrument inaccuracies. However, the observed energy values are within 3% of the theoretical values and were consistent for all peak fits.

In addition to obtaining centroid energies, the PeakFit program integrated each peak to produce a net area and the full width at half maximum values for each peak. The resultant areas were based on what the Si(Li) detector received. Attenuation of the PXR occurred through the kapton (C<sub>22</sub>O<sub>5</sub>N<sub>2</sub>H<sub>10</sub>) window in the target chamber, the beryllium (Be) window of the detector and the air gap between kapton window and the detector. Measured thicknesses,  $t$ , for each of these were 0.0025 cm, 0.005 cm and 1.8 cm, respectively. PhotCoef was used to calculate the attenuation coefficients at each energy. At low energies the attenuation coefficients varied across each peak, whereas the coefficients were approximately constant across the higher energy peaks. Assuming a linear behavior of the attenuation coefficient across the lower energy peaks, which were fitted with a Gaussian distribution, the centroid energy could be used as the average energy across the peak. This turned out to be a good approximation and is shown to be in Appendix A. The net corrected areas for the crystal and silver peaks were calculated as follows [Ref. 15]:

$$A_{peak}^{corr} = A_{peak}^{net} \frac{1}{\epsilon} \exp \left[ \mu_{air} \rho_{air} t_{air} + \mu_{Be} \rho_{Be} t_{Be} + \mu_{Kap} \rho_{Kap} t_{Kap} \right], \quad (14)$$

where  $\mu_{air}$ ,  $\mu_{Be}$  and  $\mu_{Kap}$  are the attenuation coefficients ( $\text{cm}^2/\text{g}$ ) at each centroid peak energy,  $\rho_{air} = 1.21 \times 10^{-3} \text{ g/cm}^3$ ,  $\rho_{Be} = 1.848 \text{ g/cm}^3$ ,  $\rho_{Kap} = 1.42 \text{ g/cm}^3$  and  $\epsilon$  is the detector efficiency and varies with the energy of the PXR. The efficiency curve for the Canberra Si(Li) detector at various energies [Ref. 16] is given in Figure (13):

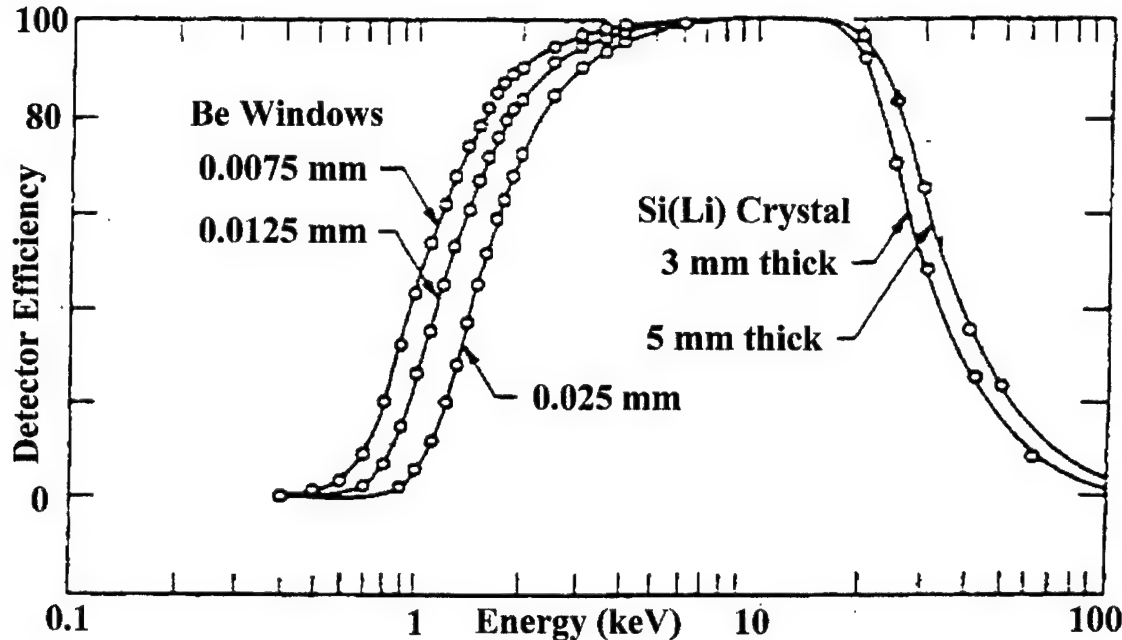


Figure (13). Efficiency Curves for the Canberra Si(Li) Detector

## B. PXR PEAK AREA UNCERTAINTY CALCULATION

Uncertainties existed in the net peak areas given by PeakFit which did not provide the area uncertainty values. To estimate the uncertainty a triangular peak was assumed. The background area for each peak was calculated as follows:

$$A_{Bkgd} = 2 \cdot FWHM \cdot [a_0 + a_1(\text{peak channel})], \quad (15)$$

where  $a_0$  and  $a_1$  are the background coefficients taken from the PeakFit parameters,  $FWHM$  is the number of channels of the full width at half maximum for each peak and

*peak channel* is the centroid value of each peak. The area uncertainty for each peak is then:

$$\delta A = \sqrt{A^{net} + 2 \cdot A_{Bkgd}}, \quad (16)$$

where  $A^{net}$  is net uncorrected area obtained from the PeakFit results. Since the calculation of the number of photons per electron,  $N$ , involves the division of the  $A_{cry}$  by  $A_{Ag}$  (discussed in next section) a total uncertainty was calculated in quadrature:

$$\delta A_{Tot} = \sqrt{\left(\delta A_{cry}\right)^2 + \left(\delta A_{Ag}\right)^2}, \quad (17)$$

where the terms inside the square root are calculated using Equation (16). The total uncertainty values obtained varied from about 4.6% at the Bragg condition to approximately 18.6% at the furthest angle away from the Bragg condition. Appendix B. lists the area uncertainty values for all peaks. Also, the uncertainties were larger for higher mosaicities as expected.

### C. PXR YIELD CALCULATION

The corrected peak areas were used to calculate the number of photons per electron as follows [Ref. 15]:

$$N = \frac{A_{cry}^{Corr}}{I_{LINAC}}, \quad (18)$$

where

$$I_{LINAC} = \frac{A_{Ag}^{Corr}(AW_{Ag})}{\sigma_{Ag}\left(\frac{\Omega_{Det}}{4\pi}\right)\rho_{Ag}(N_A)f_{dex}(t_{eff})a_{cry}}.$$

$I_{LINAC}$  is the electron beam current determined by the yield of the silver fluorescent peak.  $AW_{Ag}$  is the atomic weight of Ag (107.9 g/mol),  $N_A$  is Avagadro's number ( $6.023 \times 10^{23} \text{ mol}^{-1}$ ),  $\sigma_{Ag}$  is the electron interaction cross section ( $1.05 \times 10^{-22} \text{ cm}^2$  for a 95 MeV electron beam) [Ref. 17],  $f_{dex}$  is the de-excitation transition probability (0.692)[Ref. 17], and  $\rho_{Ag}$  is the density of silver (10.5 g/cm<sup>-3</sup>). The fluorescent x-rays from the silver undergo absorption through the crystal and is calculated as follows:

$$a_{cry} = \exp \left[ - \left( \frac{t_{cry}}{\sin \theta_B} \right) \rho_{cry} \mu_{cry} \right], \quad (19)$$

where  $\mu_{cry}$  is the attenuation coefficient of the crystal at the silver K<sub>α</sub> energy,  $\rho_{cry}$  is the density of the crystal and the term in the parenthesis is the effective thickness of the crystal through which the fluorescent x-rays pass through.

The effective thickness of the silver,  $t_{eff}$ , through which the electrons pass through was calculated by dividing the thickness of the silver,  $t_{\perp}$ , by the sin of the angle of incidence of the electron beam as shown in Figure (14):

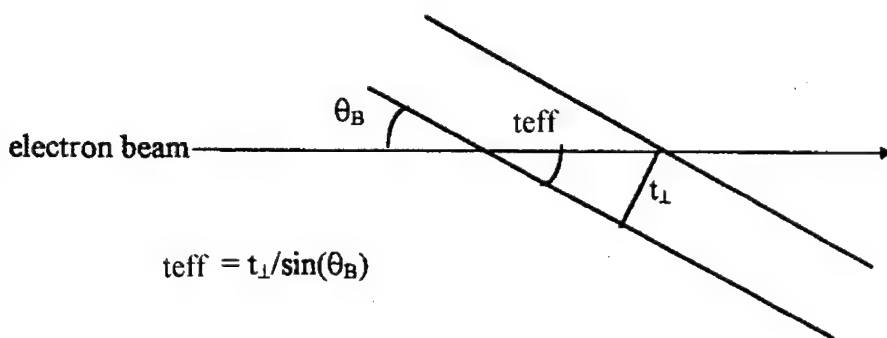


Figure (14). Configuration of Silver Foil to Determine Silver Effective Thickness.  $\theta_B$  is the Bragg Angle or the Angle between the Target Face and the Electron Beam Direction.  $t_{\perp}$  is the Normal Target Thickness

The detector solid angle,  $\Omega_{Det}$ , was calculated based on the 1 mm wide by 16 mm long slit placed on the detector window. The solid angle is calculated by:

$$\Omega_{Det} = \frac{A_{Slit}}{Dist^2}, \quad (20)$$

where the  $Dist^2$  is the distance from the crystal to the detector (1000 mm).

The calculation for the effective silver thickness must be further modified to account for the attenuation of the fluorescent x-rays by the silver foil. Section V. discusses this effect in further detail to explain the differences in PXR yield from previous experiments. The following equation accounts for this [Ref. 15]:

$$t_{eff} = \frac{\left\{ 1 - \exp \left[ - \left( \frac{t_{\perp}}{\sin \theta_B} \right) \rho_{Ag} \mu_{Ag} \right] \right\}}{\rho_{Ag} \mu_{Ag}}, \quad (21)$$

where  $\mu_{Ag}$  is the attenuation coefficient at the silver  $K_{\alpha}$  energy. The resultant yields for each of the crystals at the angles listed earlier were plotted to obtain the “rocking curves.” The observed yield versus the crystal orientation angle is shown in Figures (15-17) for the ZYA, ZYD and ZYH crystals. Included on the plots are the spectral orders. Figures (18-20) shows the first spectral order comparison between the crystals. Figures (21-23) depict the uncertainty error bars with the yield on semi-log plots. Discussion of these plots will occur later in the thesis.

#### D. PXR INTENSITY RATIO CALCULATION

The amount of PXR can be calculated using Equation (11), however, this equation does not provide results that can be easily compared to experimental data. The PXR theory can be compared to the experimental results by calculating the ratios between the

$n = 2, 3, \dots$  peaks (in Equation (10)) to the first order peak. The factors of Equation (10) that are variables of the spectral order  $n$  have the relationship:

$$N_0 \propto \omega_B^{(n)} L_a (1 - e^{-L/L_a}) |\chi_{10}|^2 e^{-2M}, \quad (22)$$

where the terms of structure factor for graphite are given by [Ref. 10,19]:

$$\begin{aligned} \chi_{10} &= \frac{4r_e \lambda_B^2}{\pi V} f\left(\frac{\sin\theta}{\lambda}\right) \cos^2\left(\frac{\pi(h+2k)}{3}\right) & l = \text{even}; \\ \chi_{10} &= \frac{2r_e \lambda_B^2}{\pi V} if\left(\frac{\sin\theta}{\lambda}\right) \sin\left(\frac{2\pi(h+2k)}{3}\right) & l = \text{odd}. \end{aligned} \quad (23)$$

For the (002) planes in our mosaic graphite crystals, where  $h=k=0$  and  $l=\text{even}$ , the structure factor becomes:

$$\chi_{10} = \frac{4r_e \lambda_B^2}{\pi V} f\left(\frac{\sin\theta}{\lambda}\right), \quad (24)$$

where  $r_e$  is the classical electron radius,  $V$  is the volume of the unit cell of the crystal and the quantity in the parenthesis is based on the scattering angle and the wavelength of the incident beam. The squared wavelength term is a function of  $\omega_B(n)$  which is the frequency of the spectral orders at the Bragg condition. The structure factor describes how the atom arrangement, given by  $h$ ,  $k$  and  $l$  for each atom, affects the scattered beam. The variable  $f$  is referred to as the atomic scattering factor and is used to describe the “efficiency” of scattering of a given atom in a given direction and depends on the wavelength of the incident beam. For an atom undergoing thermal vibration [Ref. 10]:

$$f = f_0 e^{-M}, \quad (25)$$

where  $f_0$  is the same as  $f$ , but is for an atom at rest. The quantity  $M$  is hard to determine accurately and is a function of amplitude of the thermal vibration and the scattering angle. [Ref. 10] Since the intensity of any line depends on  $f^2$ , calculated intensities must be multiplied by  $e^{-2M}$  to allow for thermal vibration. The temperature factor,  $e^{-2M}$ , allows for thermal vibration of the atoms and is a function of  $\lambda$  and  $\theta$  for a particular material. The quantity  $M$  depends on the amplitude of the thermal vibration and the scattering angle,  $\theta$  [Ref. 10]:

$$M = B \left( \frac{\sin \theta}{\lambda} \right)^2, \quad (26)$$

where  $B$  is a function of temperature and is difficult to determine accurately.  $\lambda$  is the wavelength of the incident beam. Since  $\omega_B(n)$  and  $\lambda_B$  are functions of the spectral order:

$$\begin{aligned} \omega_B^{(n)} &= \frac{n\pi c}{d \sin \theta_B}, \\ \lambda_B^2 &= \left( \frac{2\pi c}{\omega_B^{(n)}} \right)^2, \end{aligned} \quad (27)$$

then Equation (22) can be rewritten in terms of the spectral order:

$$N_\theta \propto n L_a \left( 1 - e^{-L/L_a} \right) \left( \frac{1}{n^2} \right)^2 = \frac{1}{n^3} L_a \left( 1 - e^{-L/L_a} \right), \quad (28)$$

where  $e^{-2M}$  was left out of the proportionality since it was not a function of the spectral order as shown above. Taking the ratios of the  $n^{\text{th}}$  order peak to the first order peak results in:

$$\frac{N_{\theta}^{(n)}}{N_o^{(1)}} = \frac{1}{n^3} \frac{L_a^{(n)}}{L_a^{(1)}} \frac{\left(1 - e^{-L/L_a^{(n)}}\right)}{\left(1 - e^{-L/L_a^{(1)}}\right)}, \quad (29)$$

where  $L$  is the crystal thickness and  $n$  is the spectral order.  $L_a$  is the x-ray absorption length and is given by:

$$L_a = \frac{1}{\mu_{\text{cry}} \rho_{\text{cry}}}. \quad (30)$$

Figures (24-25) show comparisons of peak intensity ratios for the ZYA, ZYD and ZYH crystals. Equation (29) was solved for the mosaic crystals at each orientation angle and are listed in Appendix B. Although Equation (29) is for the Bragg condition, the calculations were made to see the effects of using the equation when the crystal position was not at the Bragg condition. Figures (26-28) show each crystal's data versus theory using Equation (29) and it is noted that the equation needs to be evaluated as a function of the crystal orientation angle, as well, when the Bragg condition is not met. Figures (29-31) are the peak intensities versus spectral order for the Bragg condition for each crystal. The Bragg condition was shifted for each crystal due to the alignment errors in determining the "home" position. Thus, the crystal orientation angle to plot the intensity ratios as a function of spectral order was chosen as the angle with the highest PXR yield. This turned out to be  $23.25^\circ$  for the ZYA,  $22.75^\circ$  for the ZYD and  $22.75^\circ$  for the ZYH crystals. The results show a significant deviation from calculation of the second order peak ratios whereas for the third and fourth order peak the experiment and

calculation are in agreement. The interpretation of this deviation is unclear at this time. Equation (8) can be used to calculate the PXR yield as a function of crystal orientation angle from the Bragg condition using a numerical equation solver. The resultant yields can then be used to solve the peak intensity ratios. Buckingham and Ivey [Ref. 7] used this method to solve the PXR yields with and without the effects of scattering and mosaic spread. Appendix D. lists the calculated intensity ratios for this experiment and theory intensity ratios from Buckingham and Ivey's method. Figures (32-37) are the comparison between the intensity ratio results from this experiment and the theory intensity ratios from Buckingham and Ivey's thesis as a function of crystal orientation angle. The results seem to follow their theoretical intensity ratios better than those using Equation (29).

## Photon Yield (0.45 Degree Mosaic Spread)

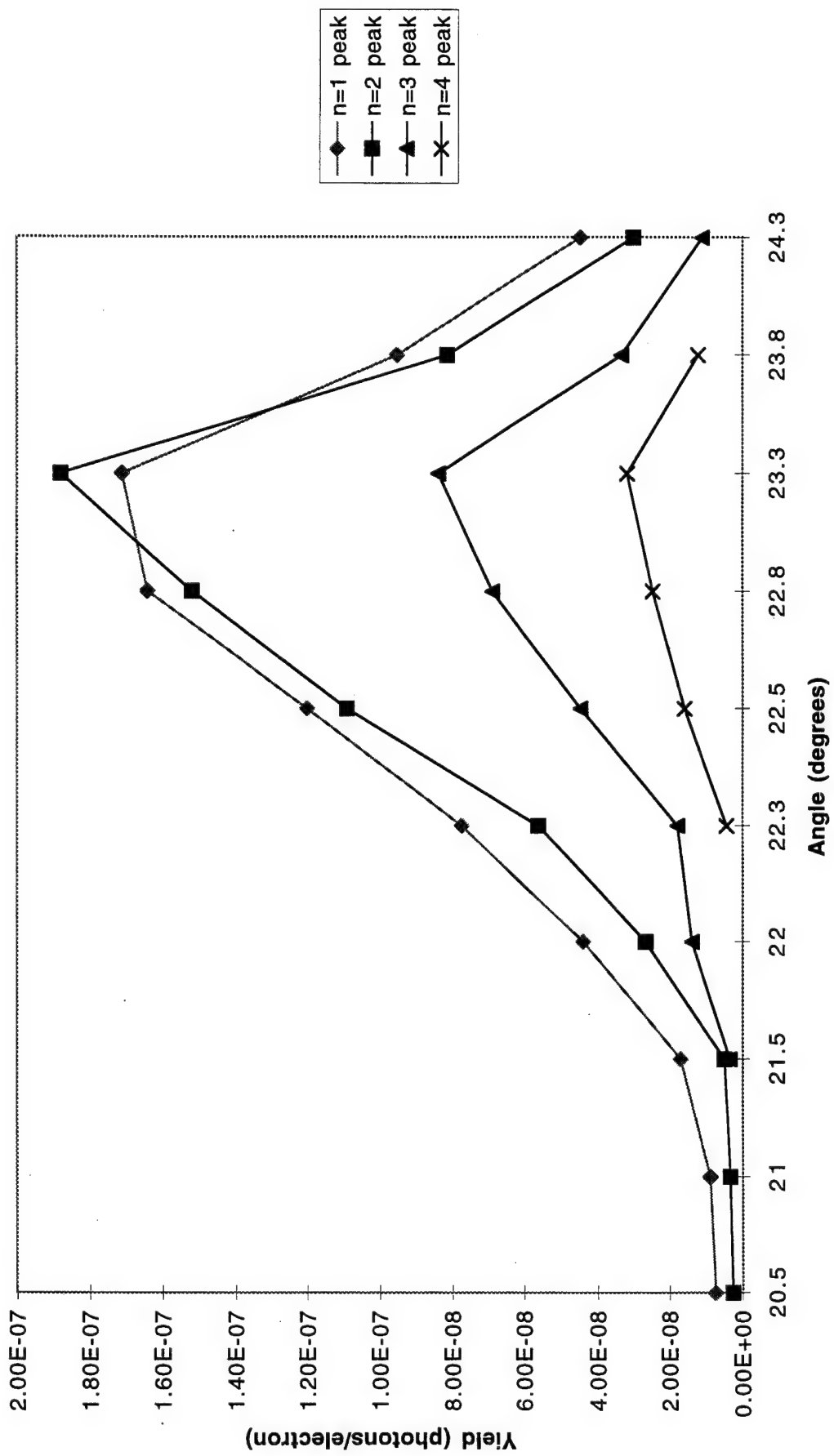


Figure (15). Observed Yield vs. Crystal Orientation Angle for the Spectral Orders of the ZYA Crystal

### Photon Yield (1.31 Degree Mosaic Spread)

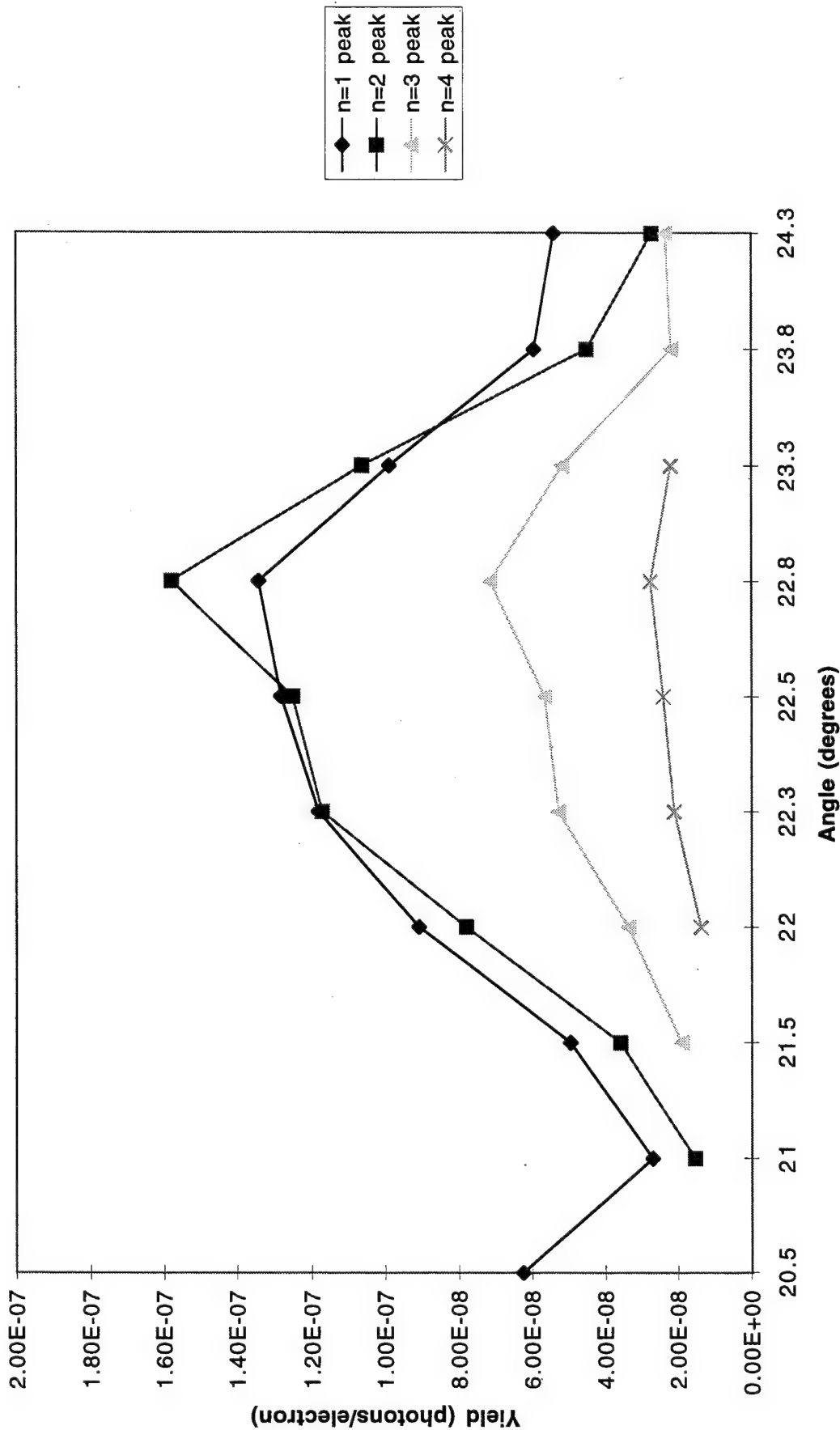


Figure (16). Observed Yield vs. Crystal Orientation Angle for the Spectral Orders of the ZYD Crystal

## Photon Yield (2.5 Degree Mosaic Spread)

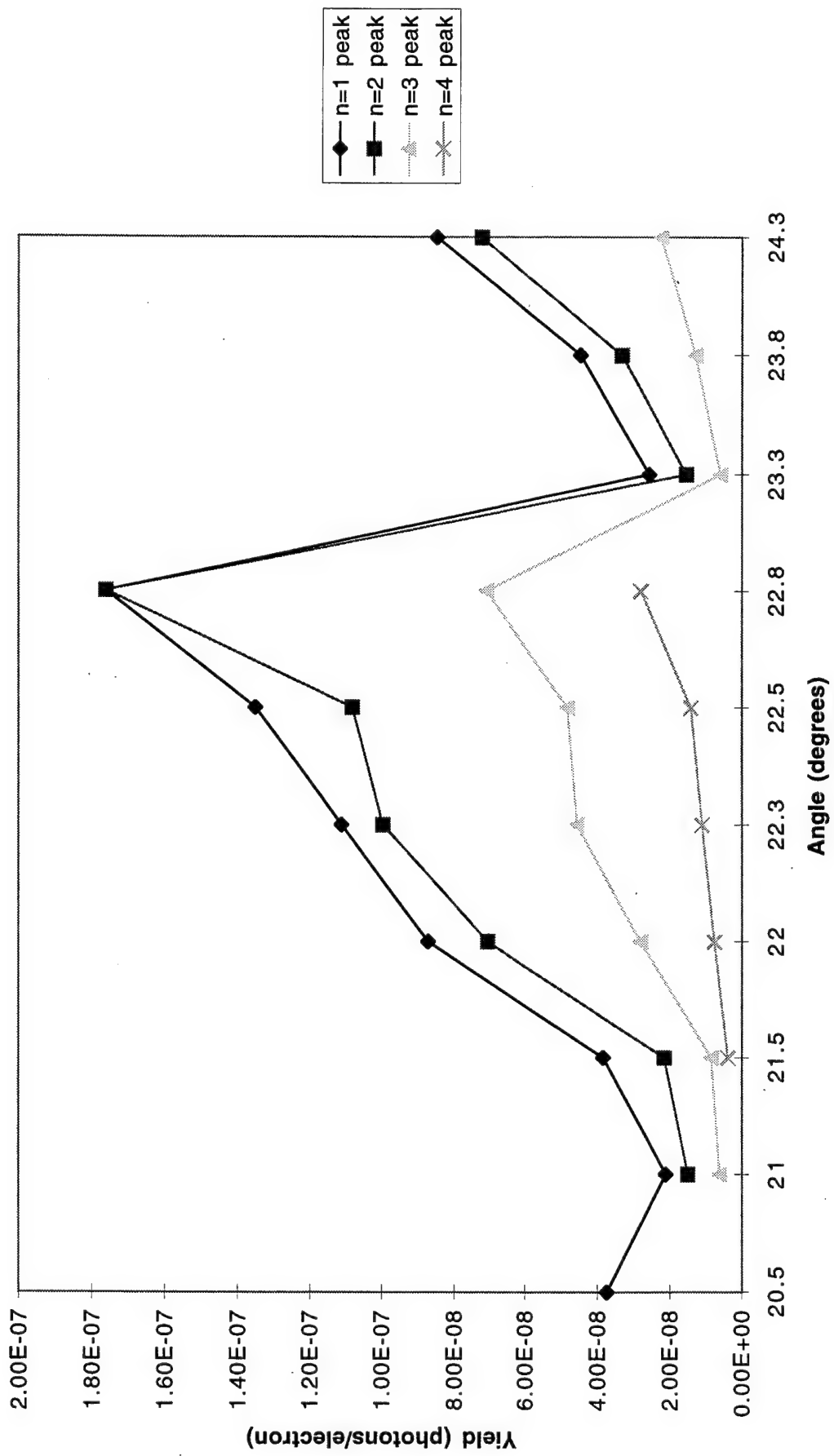


Figure (17). Observed Yield vs. Crystal Orientation Angle for the Spectral Orders of the ZYH Crystal

### Photon Yield Comparison (1st Order Peaks)

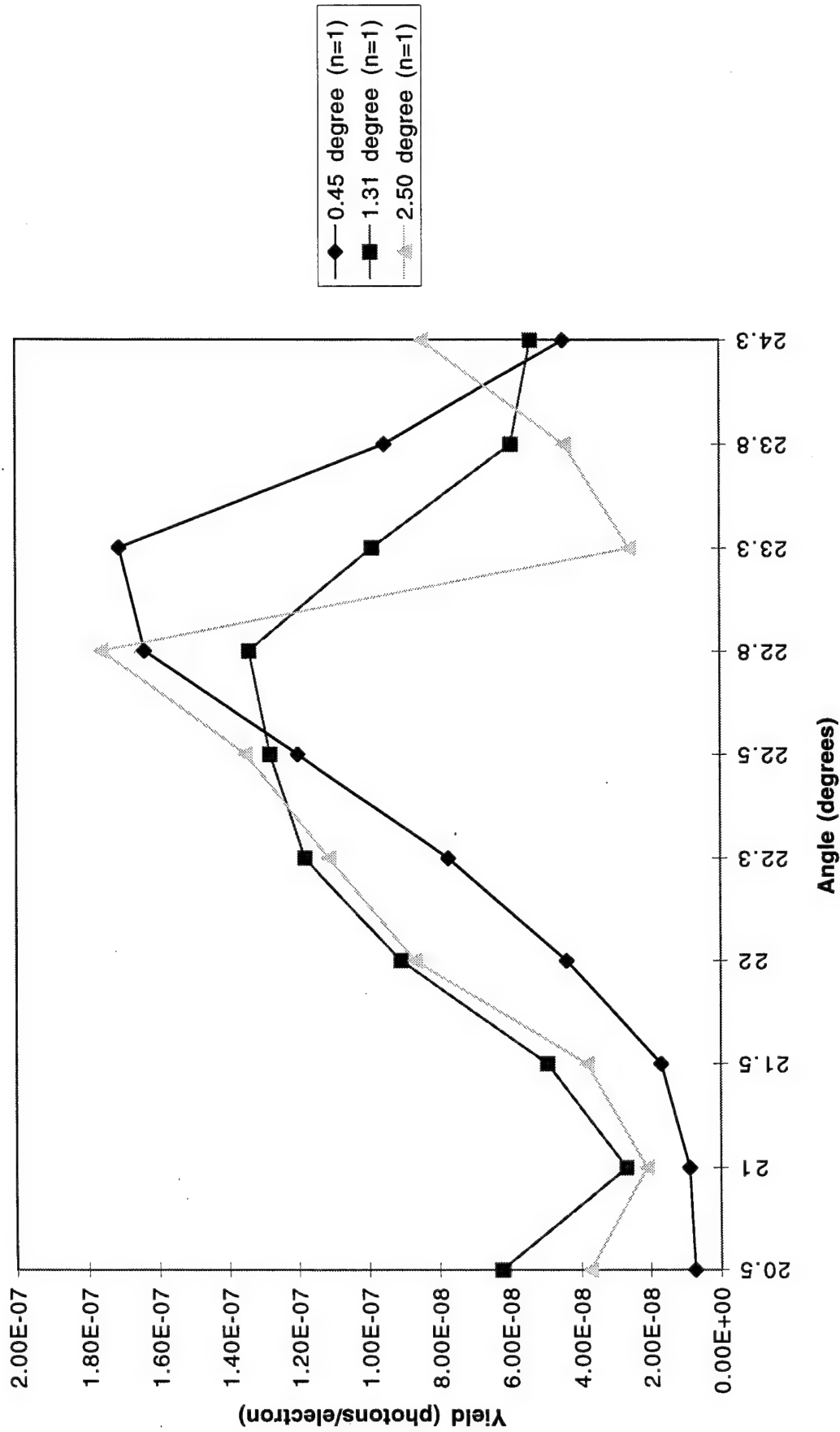


Figure (18). Observed Yield vs. Crystal Orientation Angle Comparisons for the First Spectral Order

## Photon Yield Comparison (2nd Order Peaks)

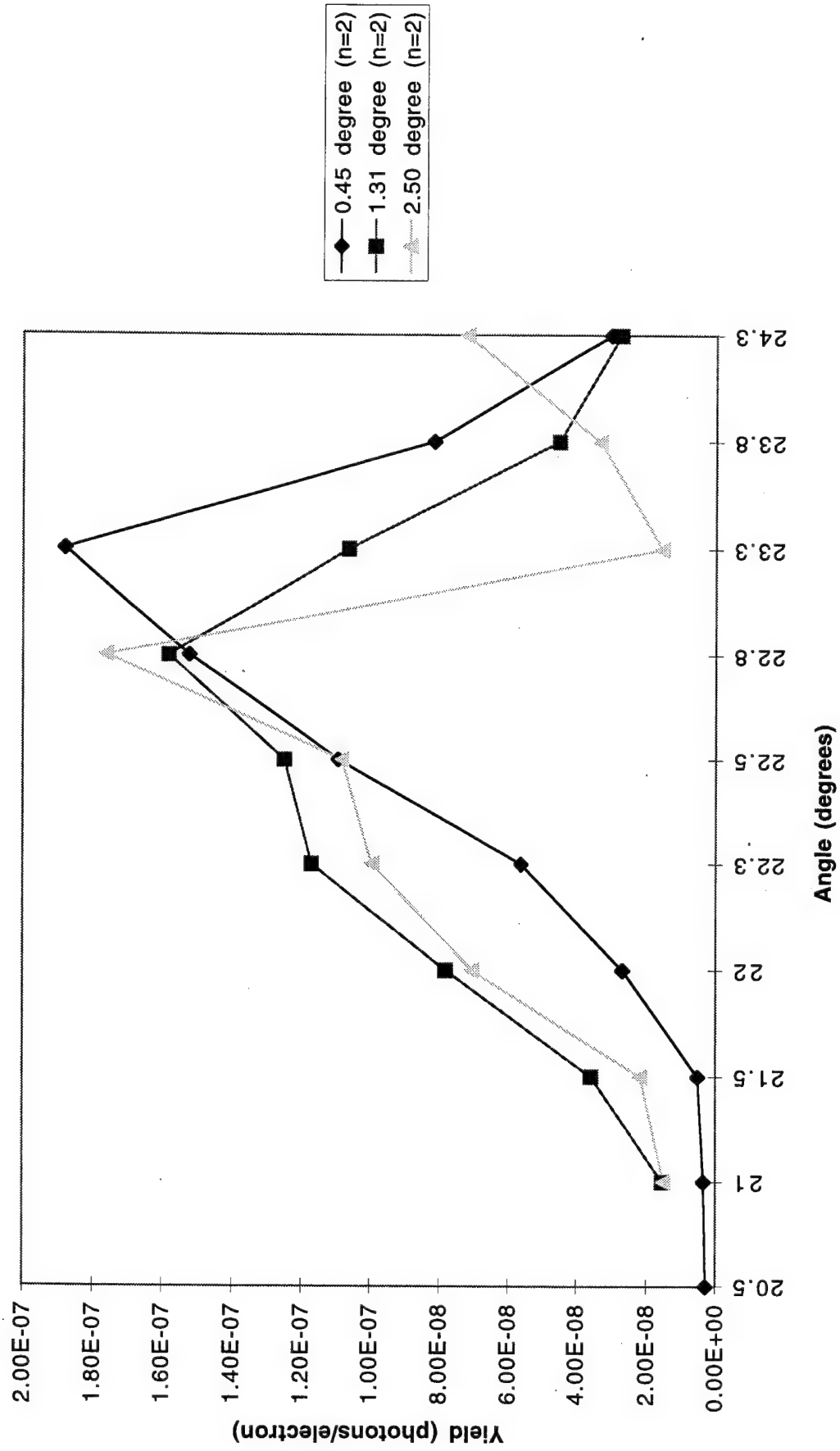


Figure (19). Observed Yield vs. Crystal Orientation Angle Comparisons for the Second Spectral Order

### Photon Yield Comparison (3rd Order Peaks)

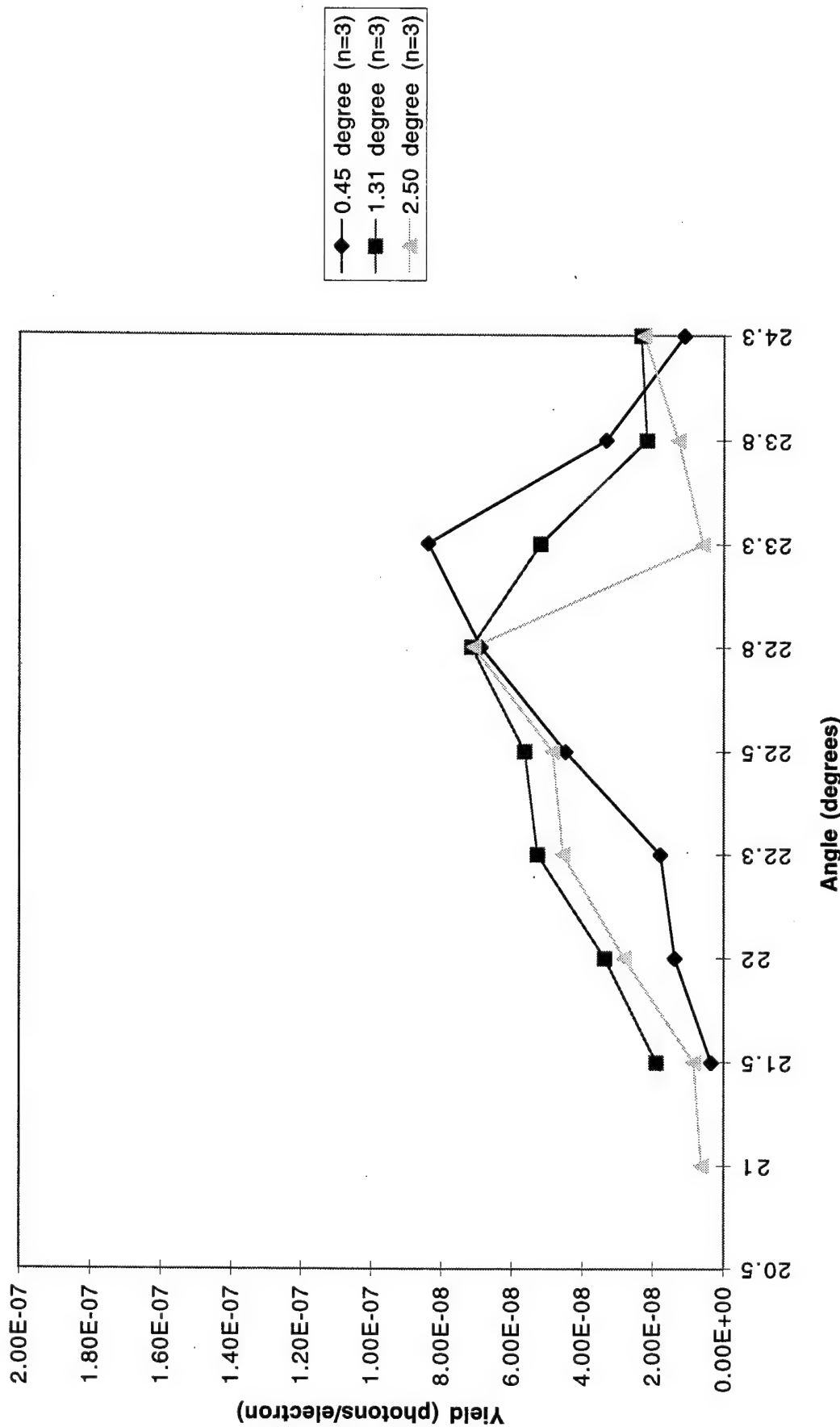


Figure (20). Observed Yield vs. Crystal Orientation Angle Comparisons for the Third Spectral Order

## Photon Yields w/ Uncertainties (0.45 Degree Mosaic Spread)

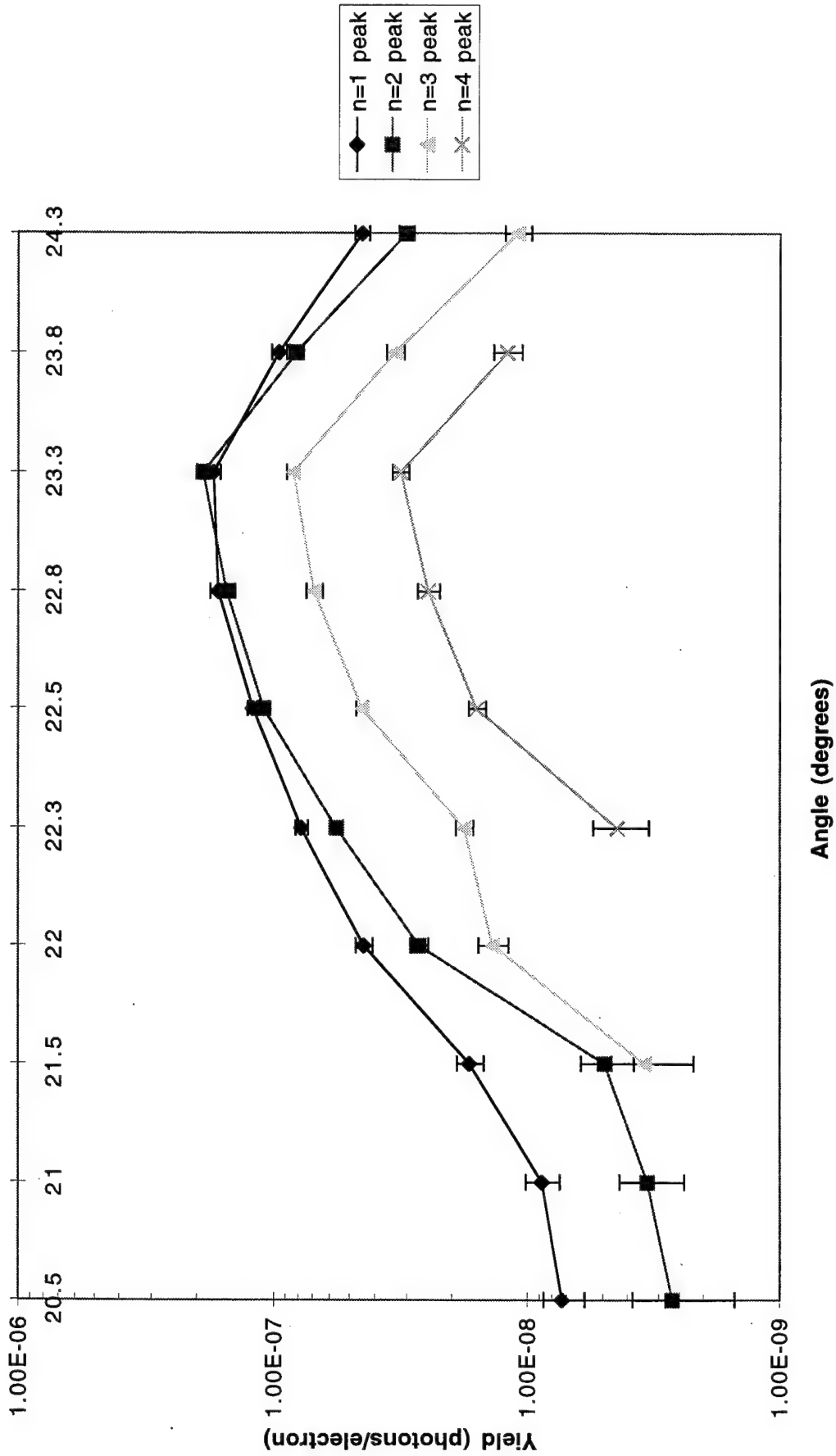


Figure (21). Semi-log Plot of Observed Yield vs. Crystal Orientation Angle with Measured Yield Uncertainties

## Photon Yields w/ Uncertainties (1.31 Degree Mosaic Spread)

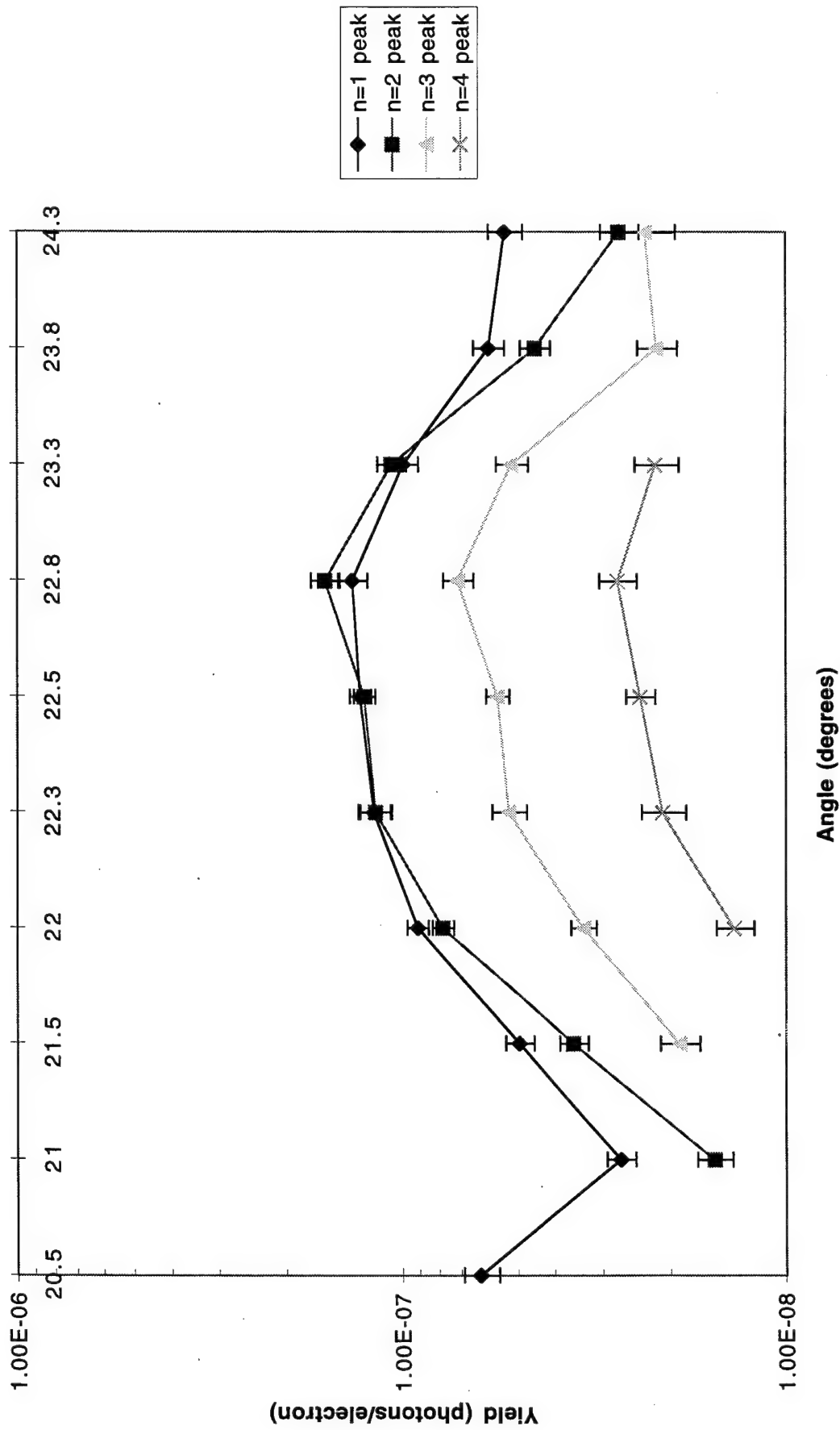


Figure (22). Semi-log Plot of Observed Yields vs. Crystal Orientation Angle with Measured Yield Uncertainties

## Photon Yields w/ Uncertainties (2.5 Degree Mosaic Spread)

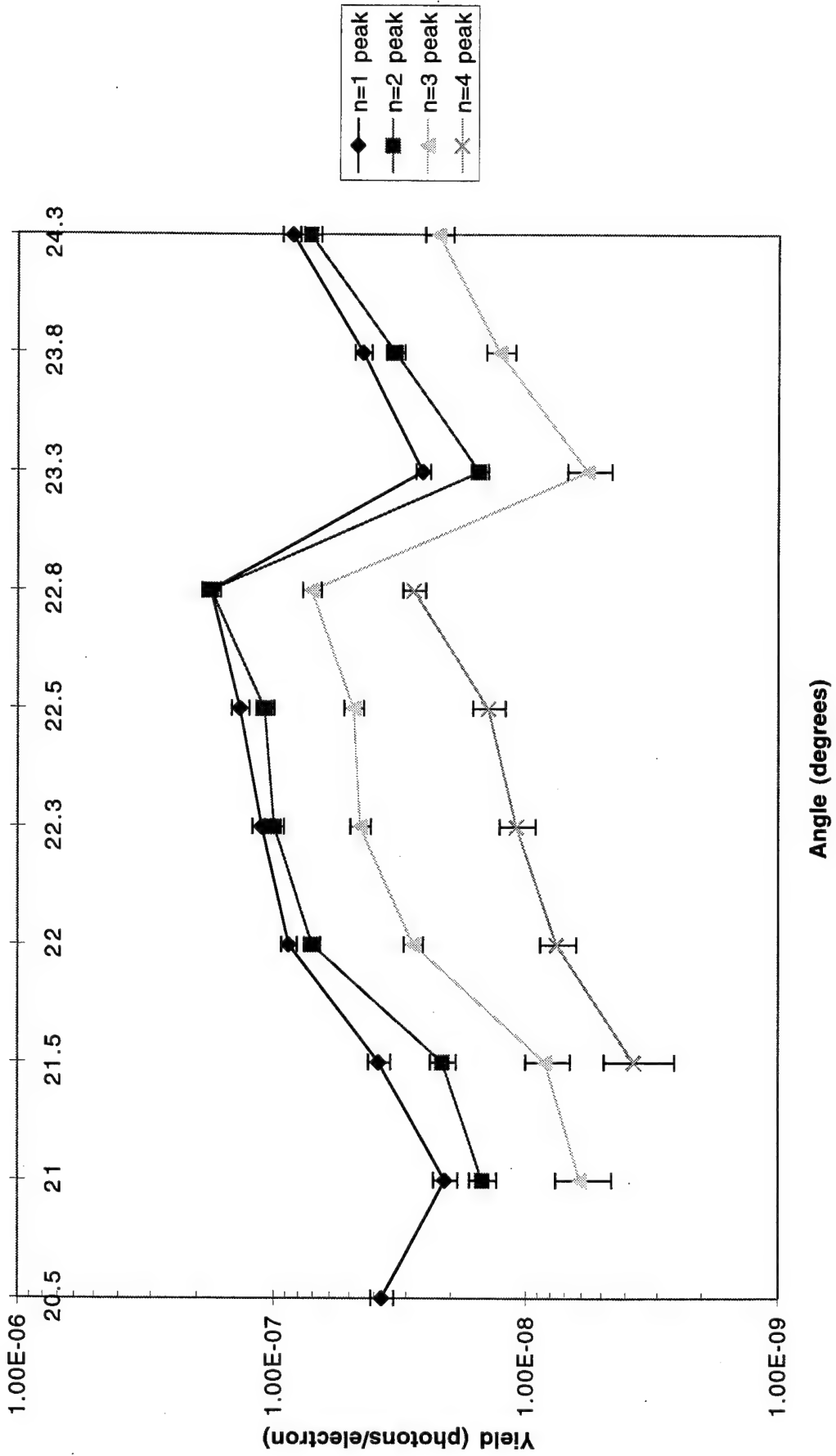


Figure (23). Semi-log Plot of Observed Yield vs. Crystal Orientation Angle w/ Measured Yield Uncertainties

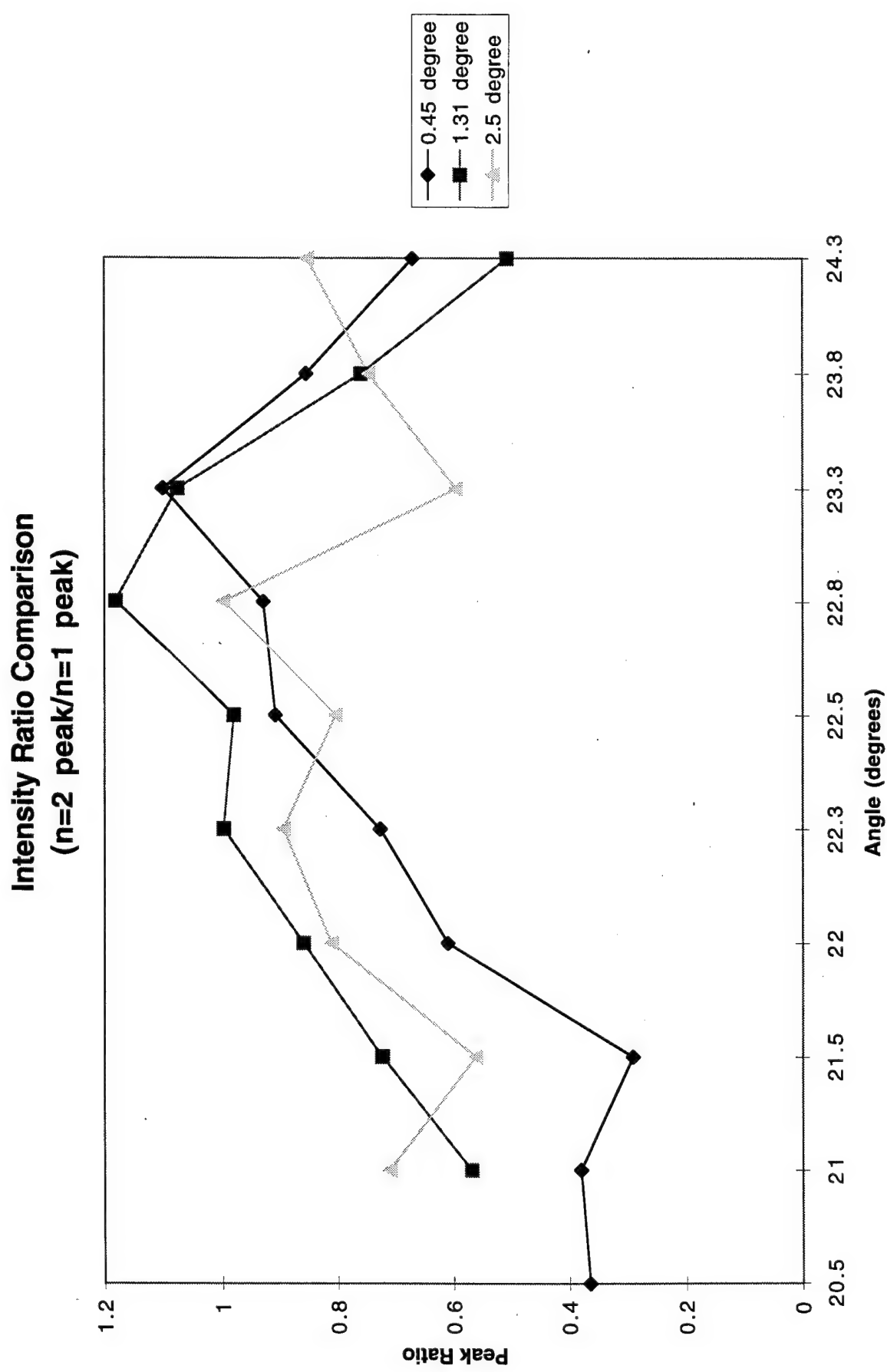


Figure (24). Comparison of PXR Intensity Ratios (Second Order Peak to the First Order Peak)

### Intensity Ratio Comparison (n=3 peak/n=1 peak)

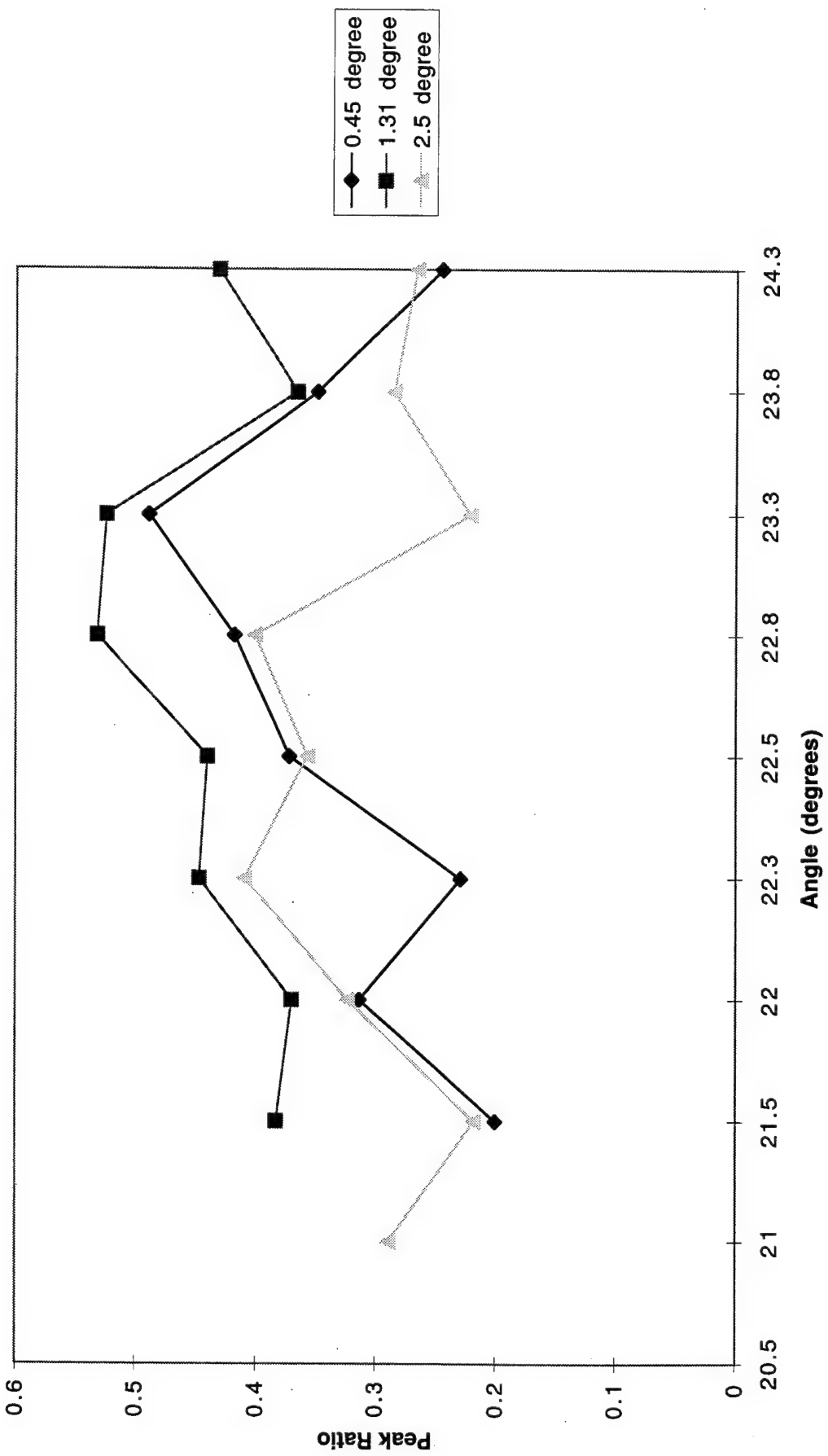


Figure (25). Comparison of PXR Intensity Ratios (Third Order Peak to the First Order Peak)

**Data vs. Theory Intensity Ratios; n=2 peak/n=1 peak  
(0.45 Degree Mosaic Spread)**

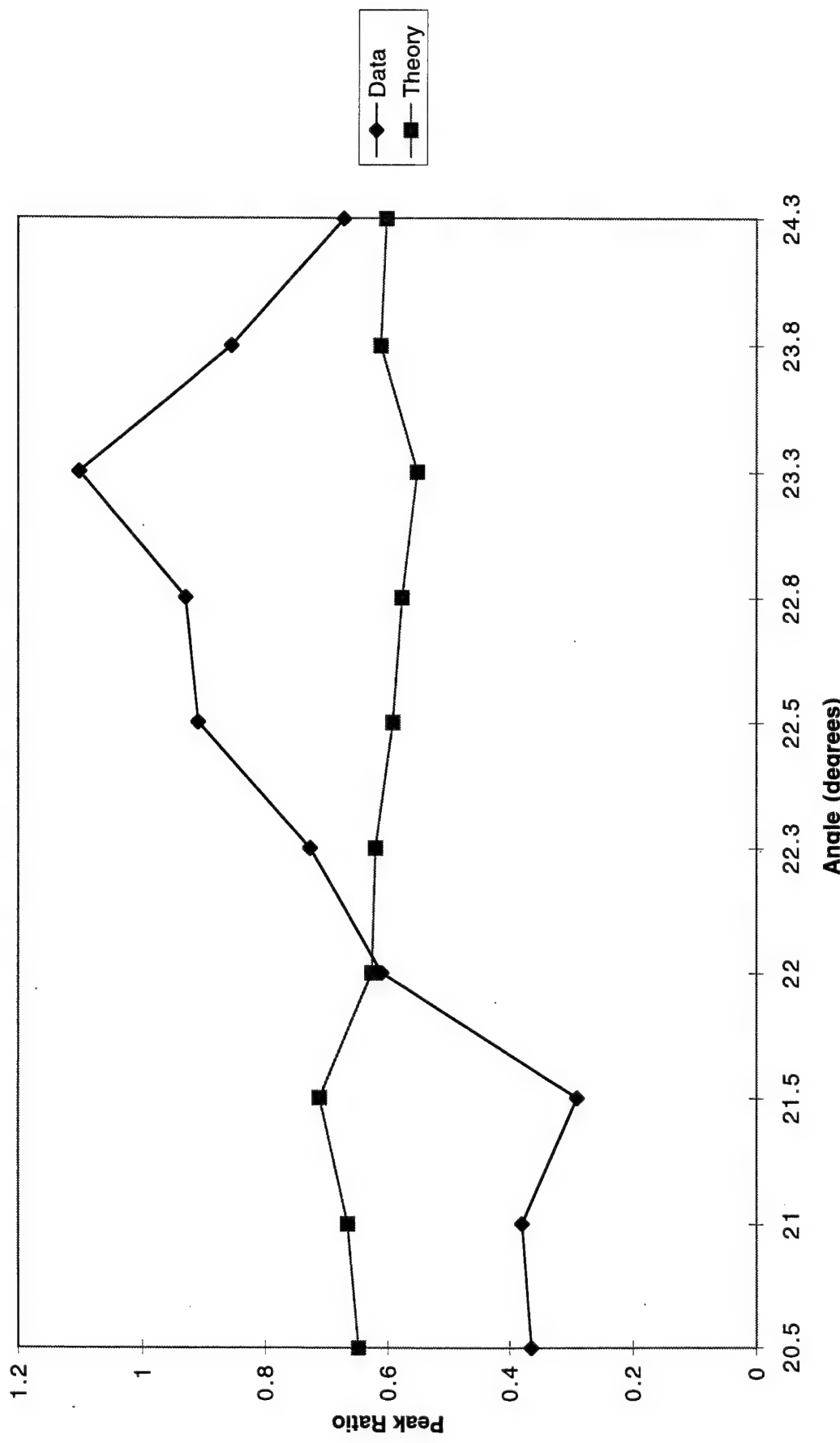


Figure (26). Second Order to First Order Peak Intensity Ratio. Data vs. Theory for ZYA Crystal Using Equation (28)

**Data vs. Theory Intensity Ratios; n=2 peak/n=1 peak  
(1.31 Degree Mosaic Spread)**

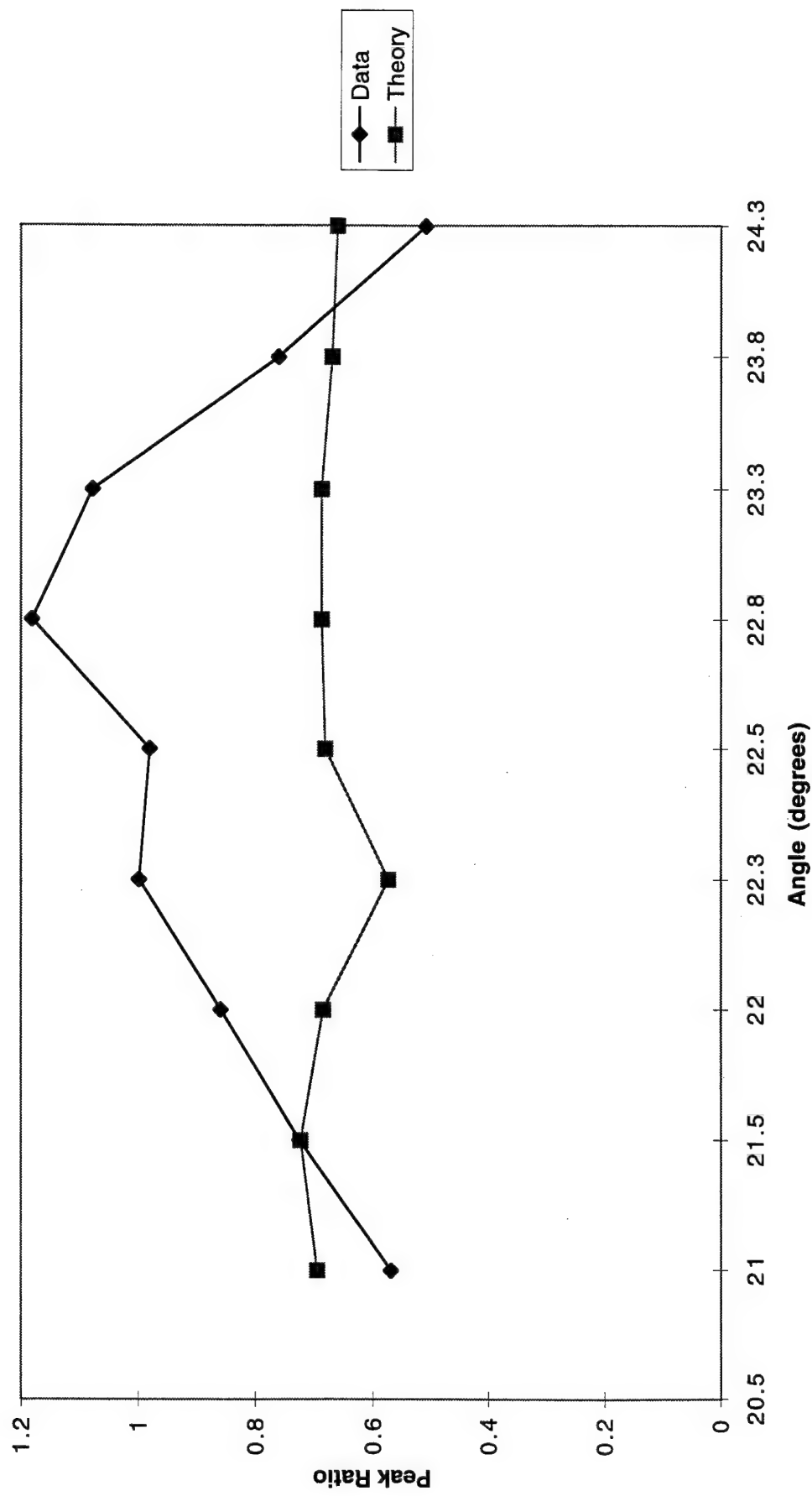


Figure (27). Second Order to First Order Peak Intensity Ratio. Data vs. Theory for ZYD Crystal using Equation (28)

**Data vs. Theory Intensity Ratios; n=2 peak/n=1 peak  
(2.5 Degree Mosaic Spread)**

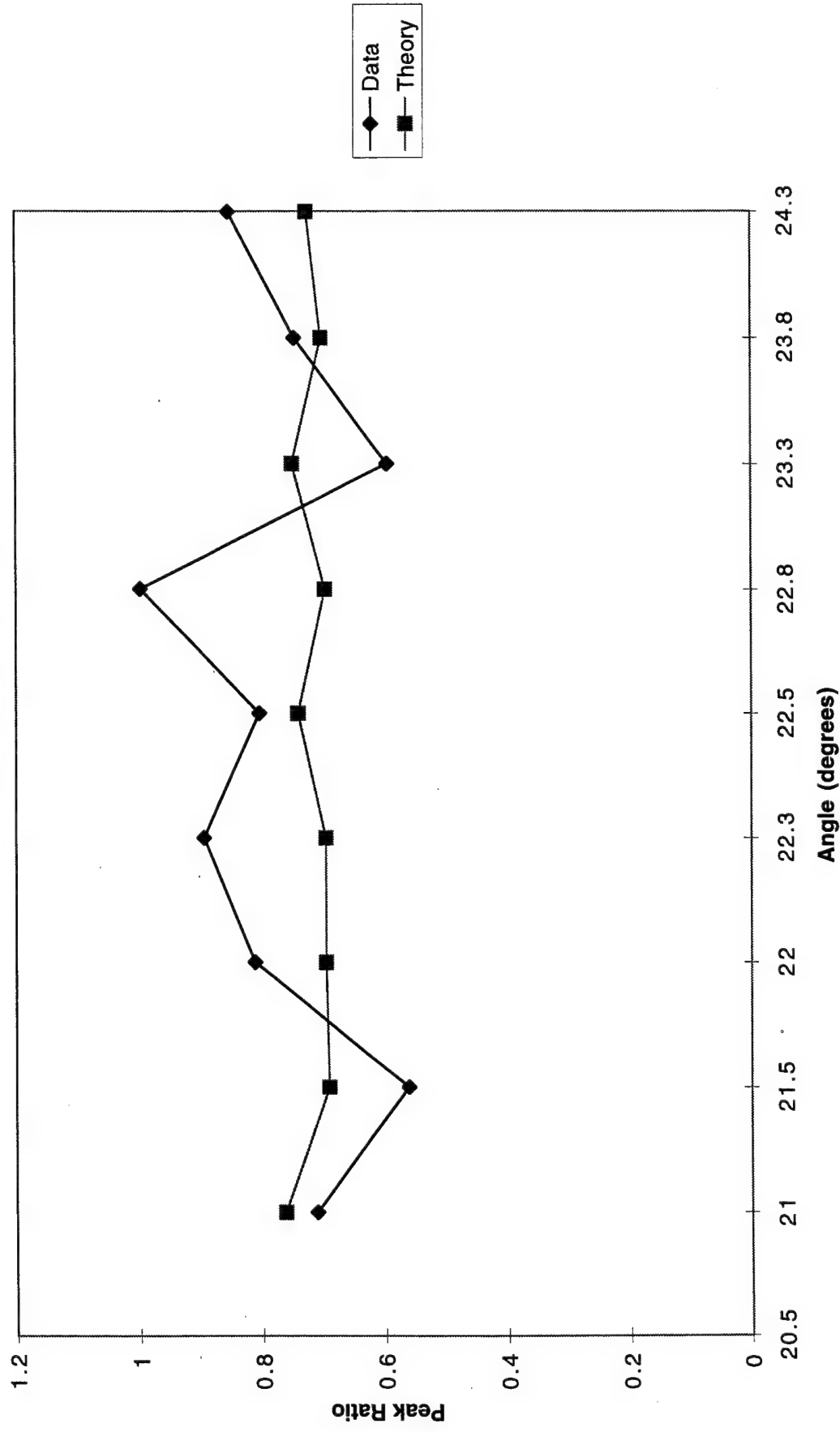


Figure (28). Second Order to First Order Peak Intensity Ratio. Data vs. Theory for ZYH Crystal Using Equation (28)

**Peak Intensity Ratios vs. Spectral Order @ 23.25 Degrees  
(0.45 Degree Mosaic Spread)**

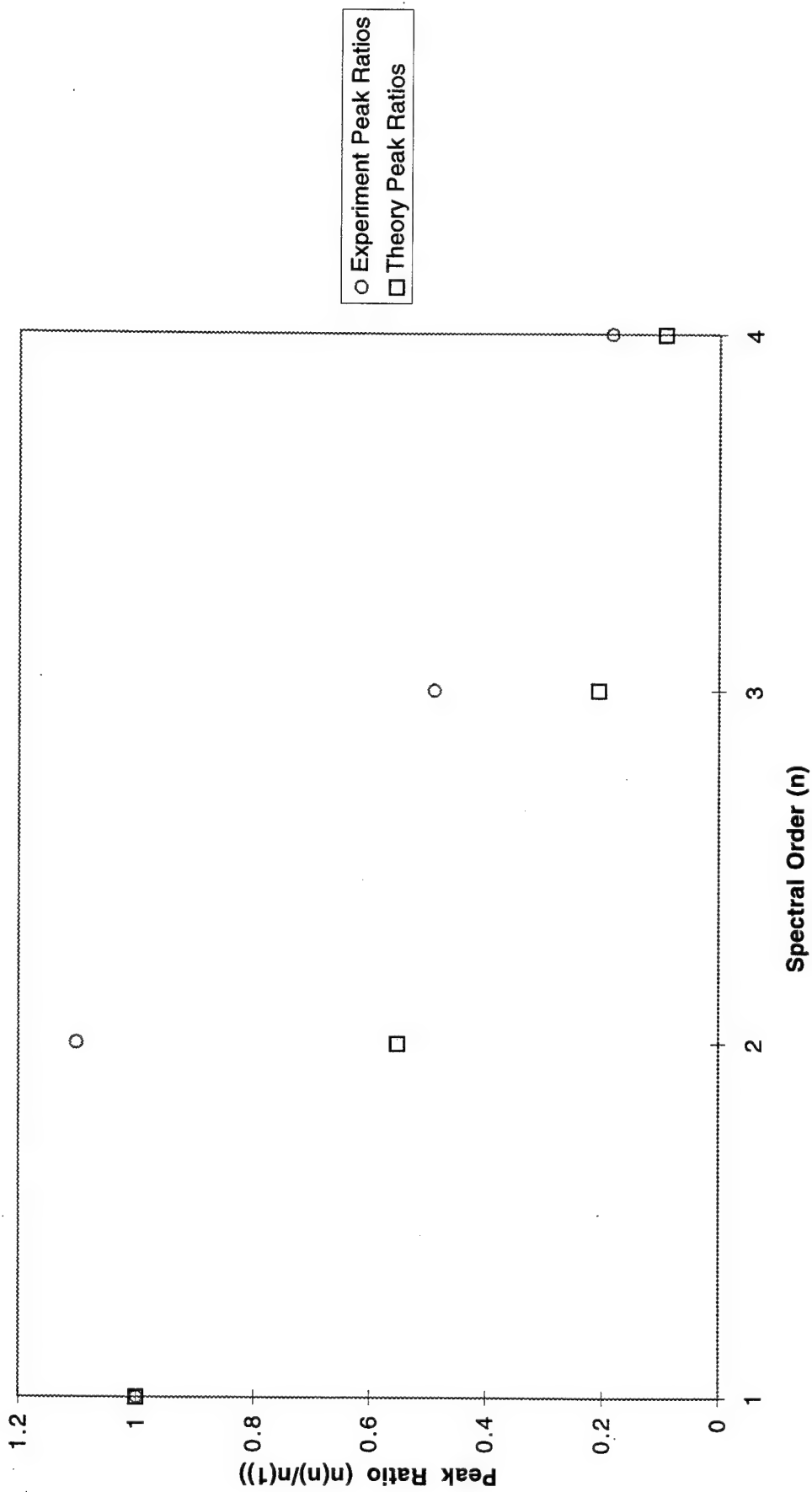


Figure (29). ZYA Peak Intensity Ratios vs. Spectral Order

**Peak Intensity Ratios vs. Spectral Order @ 22.75 Degrees  
(1.31 Degree Mosaic Spread)**

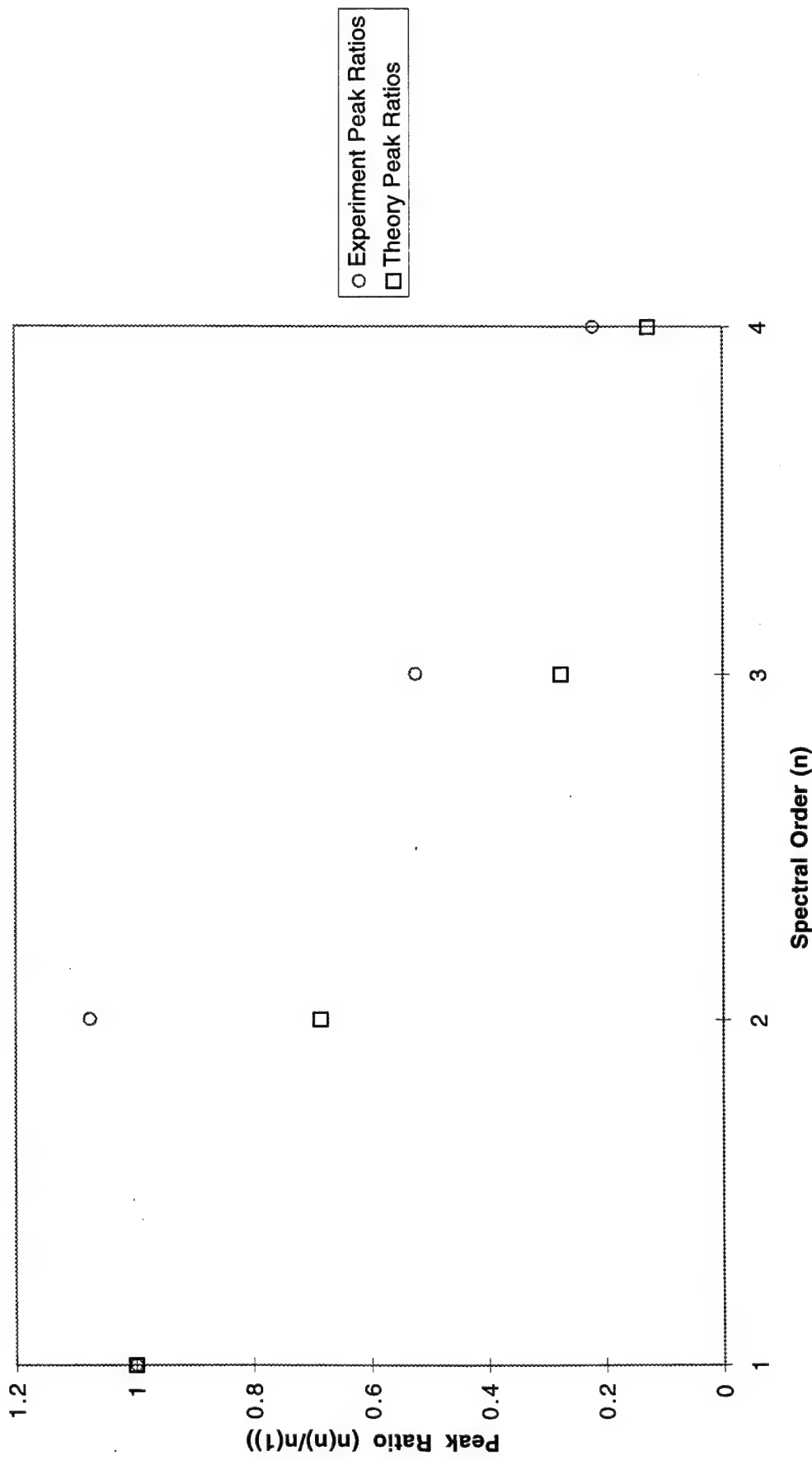


Figure (30). ZYD Peak Intensity Ratios vs. Spectral Order

**Peak Intensity Ratio vs. Spectral Order @ 22.75 Degrees  
(2.5 Degree Mosaic Spread)**

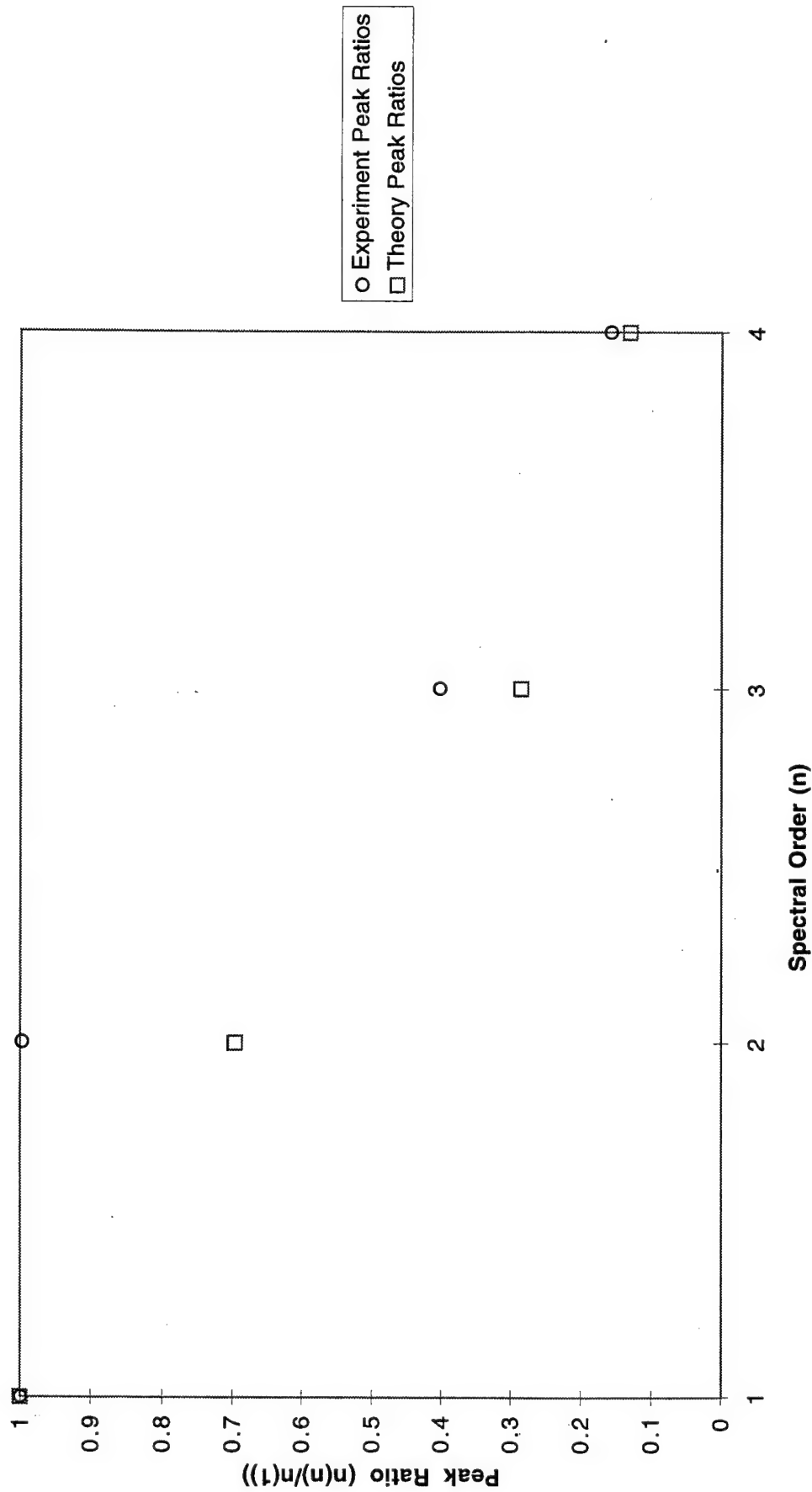


Figure (31). ZYH Peak Intensity Ratio vs. Spectral Order

**Data vs. Theory Intensity Ratios; n=2 peak/n=1 peak  
(0.45 Degree Mosaic Spread)**

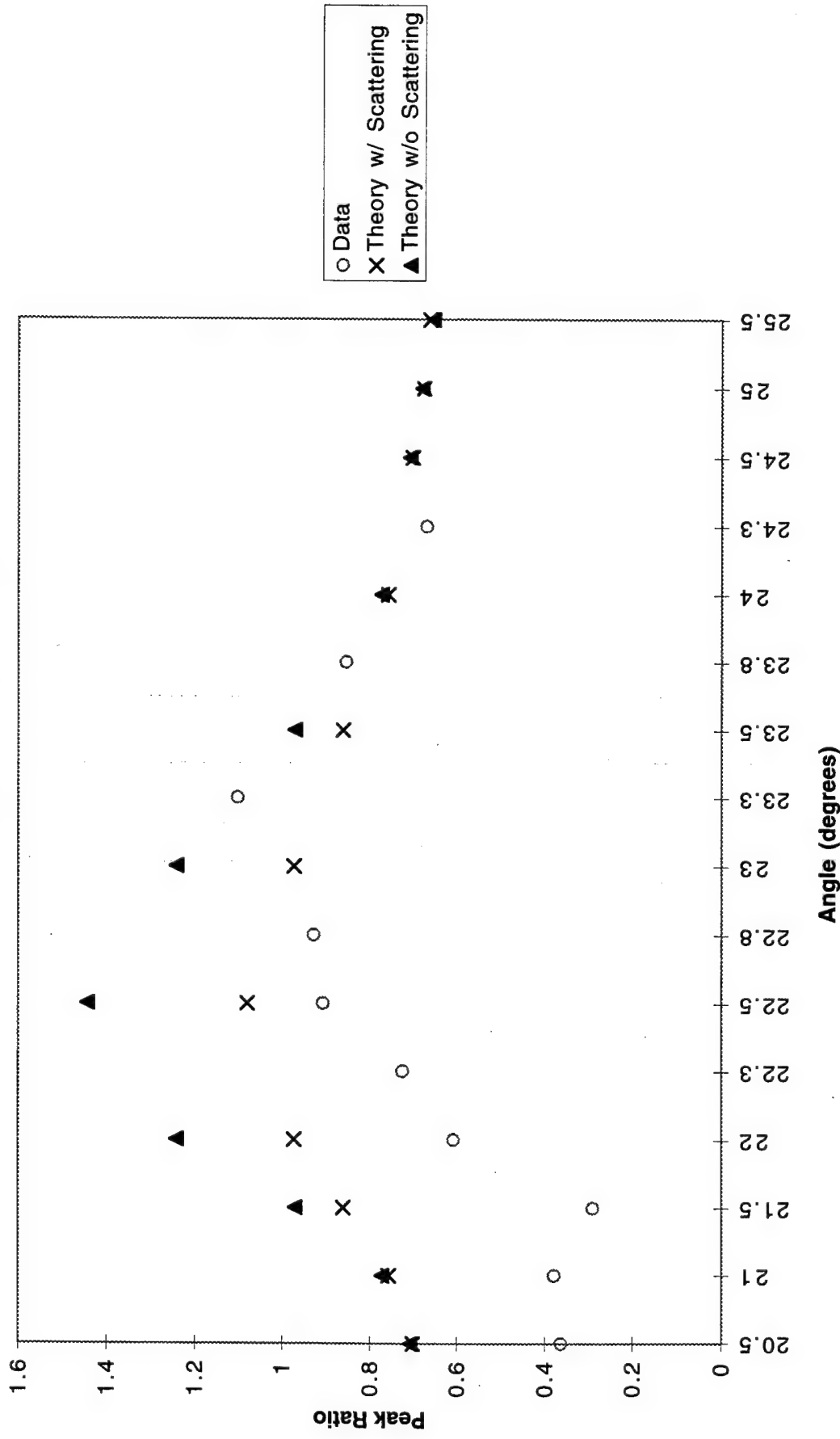
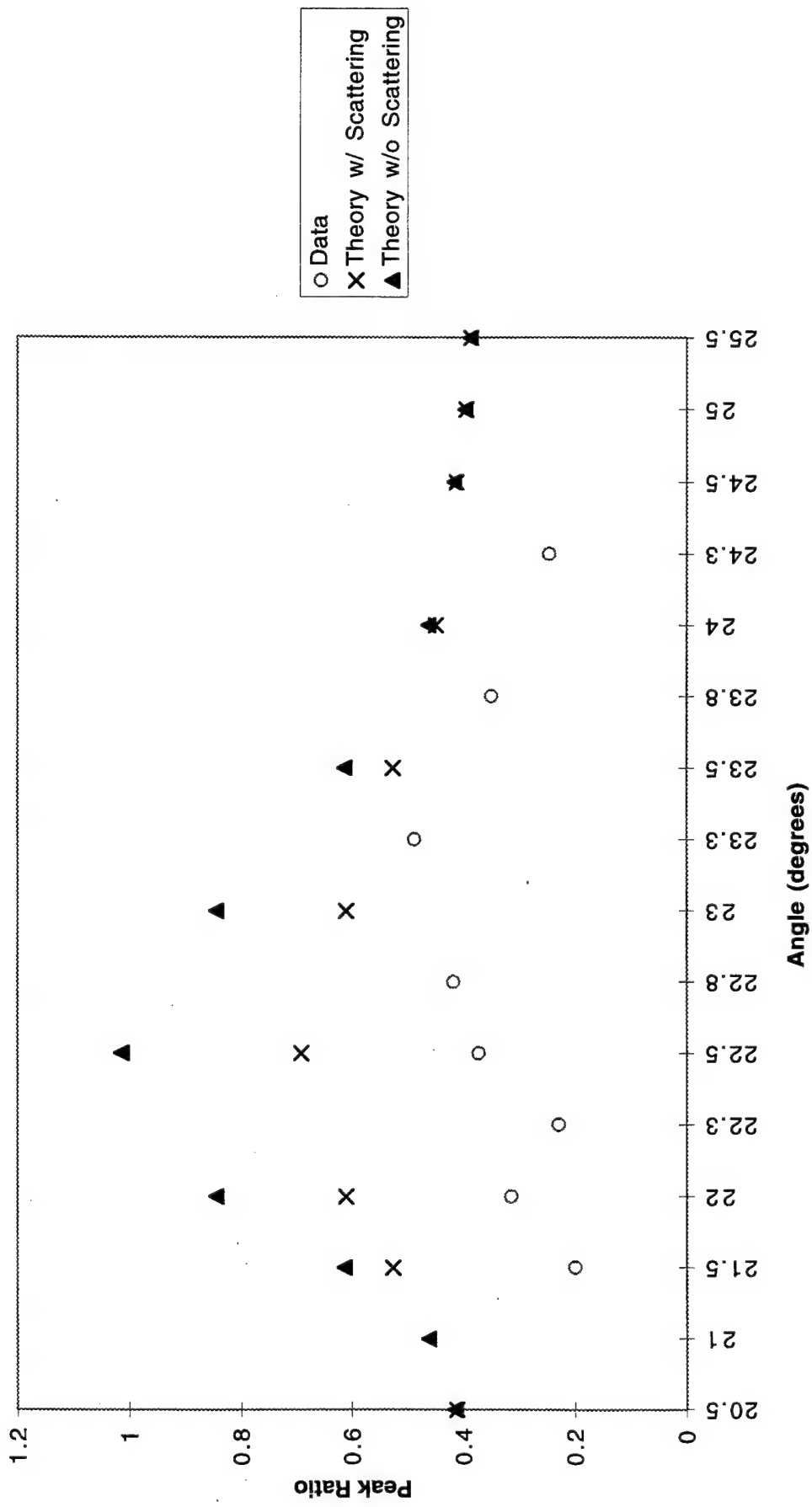


Figure (32). Data vs. Theory Intensity Ratios for the ZYA Crystal (Second Order Peak to the First Order Peak) Using Previous Experiment Peak Ratios

**Data vs. Theory Intensity Ratios; n=3 peak/n=1 peak  
(0.45 Degree Mosaic Spread)**



Figure(33). Data vs. Theory Intensity Ratios for the ZYA Crystal (Third Order Peak to the First Order Peak)  
Using Buckingham Ivey's Theoretical Peak Ratios

**Data vs. Theory Intensity Ratios; n=2 peak/n=1 peak  
(1.31 Degree Mosaic Spread)**

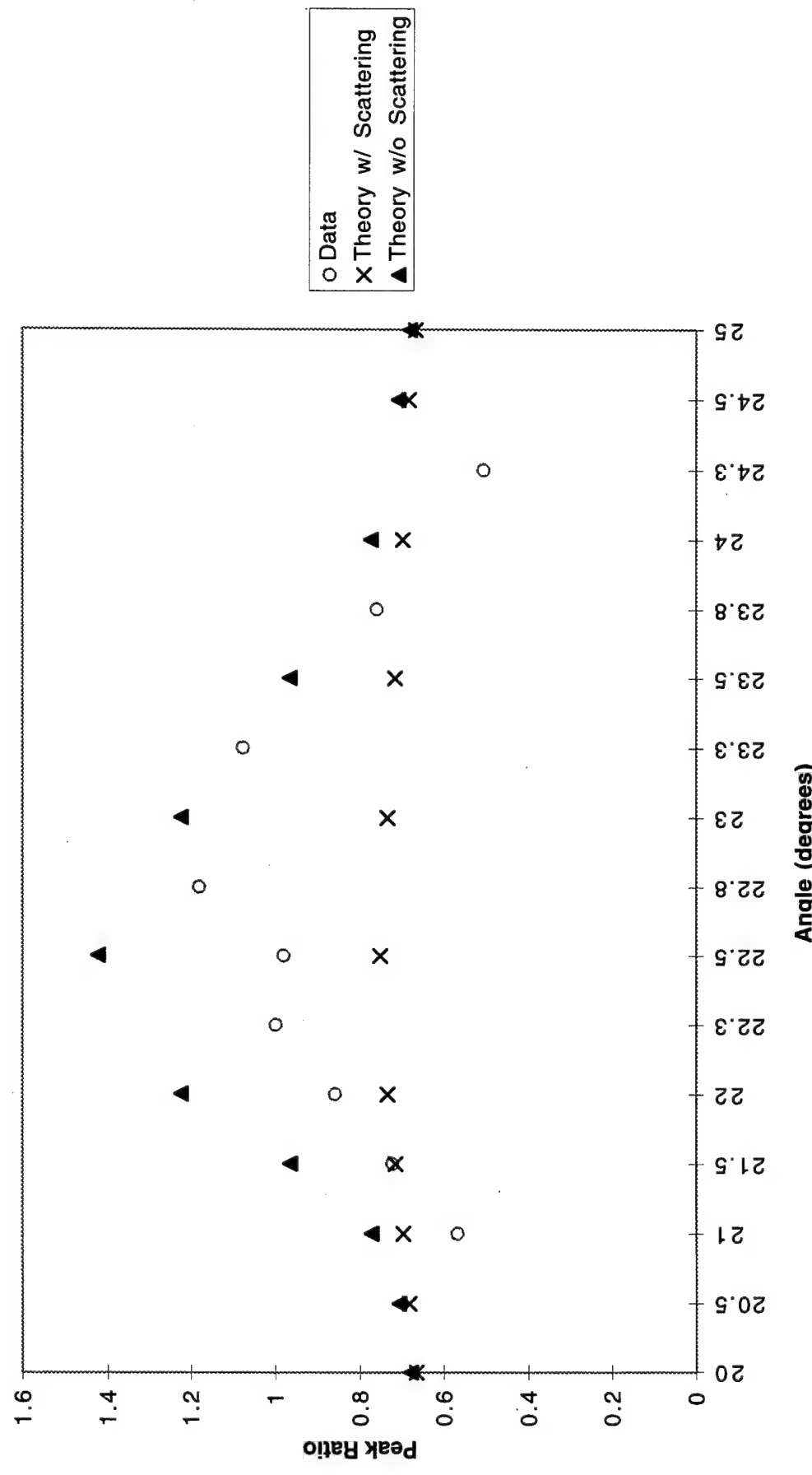


Figure (34). Data vs. Theory Intensity Ratios for the ZYD Crystal (Second Order Peak to the First Order Peak)  
Using Buckingham Ivey's Theoretical Peak Ratios

**Data vs. Theory Intensity Ratios; n=3 peak/n=1 peak  
(1.31 Degree Mosaic Spread)**

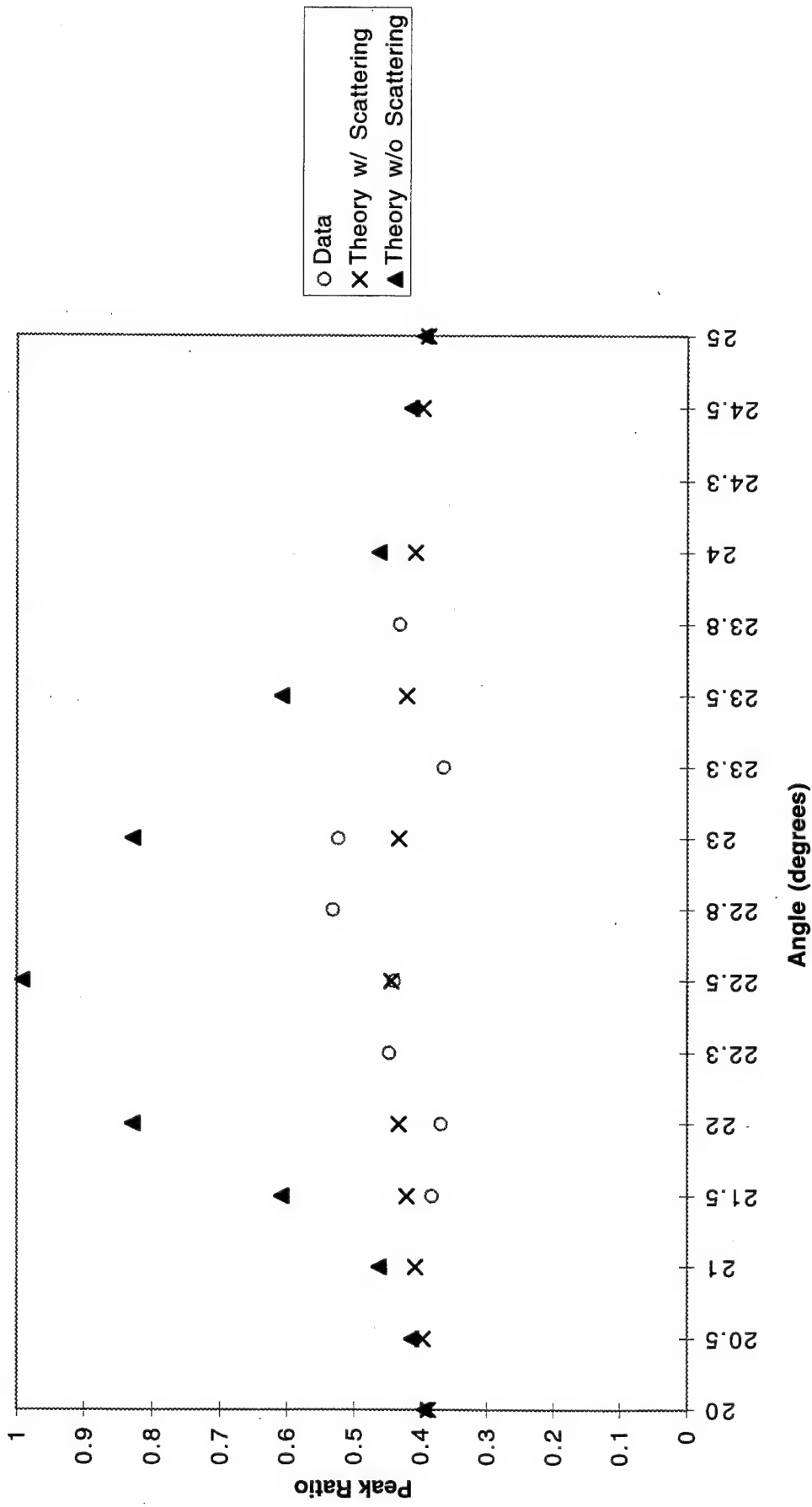


Figure (35). Data vs. Theory Intensity Ratios for the ZYD Crystal (Third Order Peak to the First Order Peak)  
Using Buckingham Ivey's Theoretical Peak Ratios

**Data vs. Theory Intensity Ratios; n=2 peak/n=1 peak  
(2.5 Degree Mosaic Spread)**

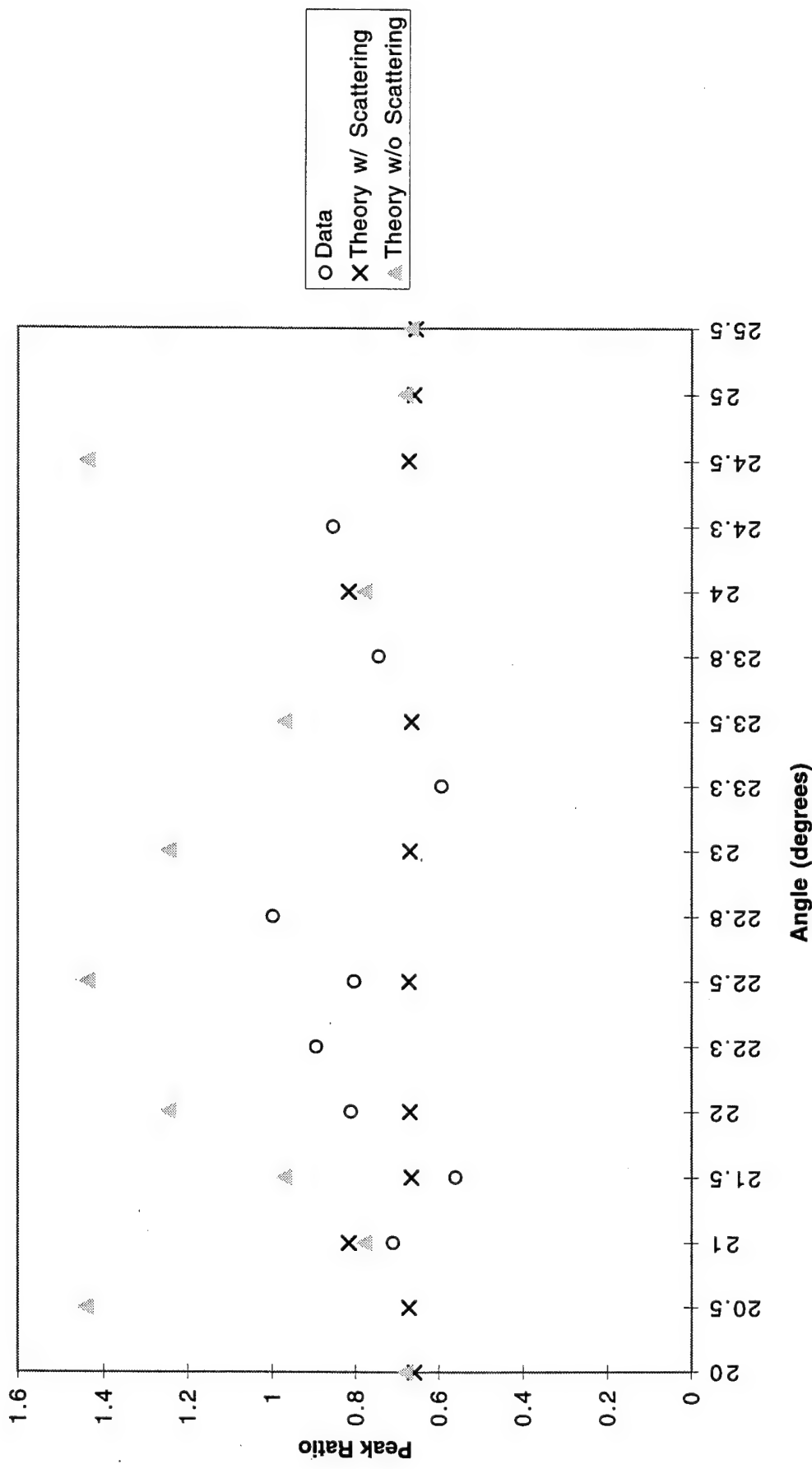


Figure (36). Data vs. Theory Intensity Ratios for the ZYH Crystal (Second Order Peak to the First Order Peak)  
Using Buckingham Ivey's Theoretical Peak Ratios

**Data vs. Theory Intensity Ratios; n=3 peak/n=1 peak  
(2.5 Degree Mosaic Spread)**

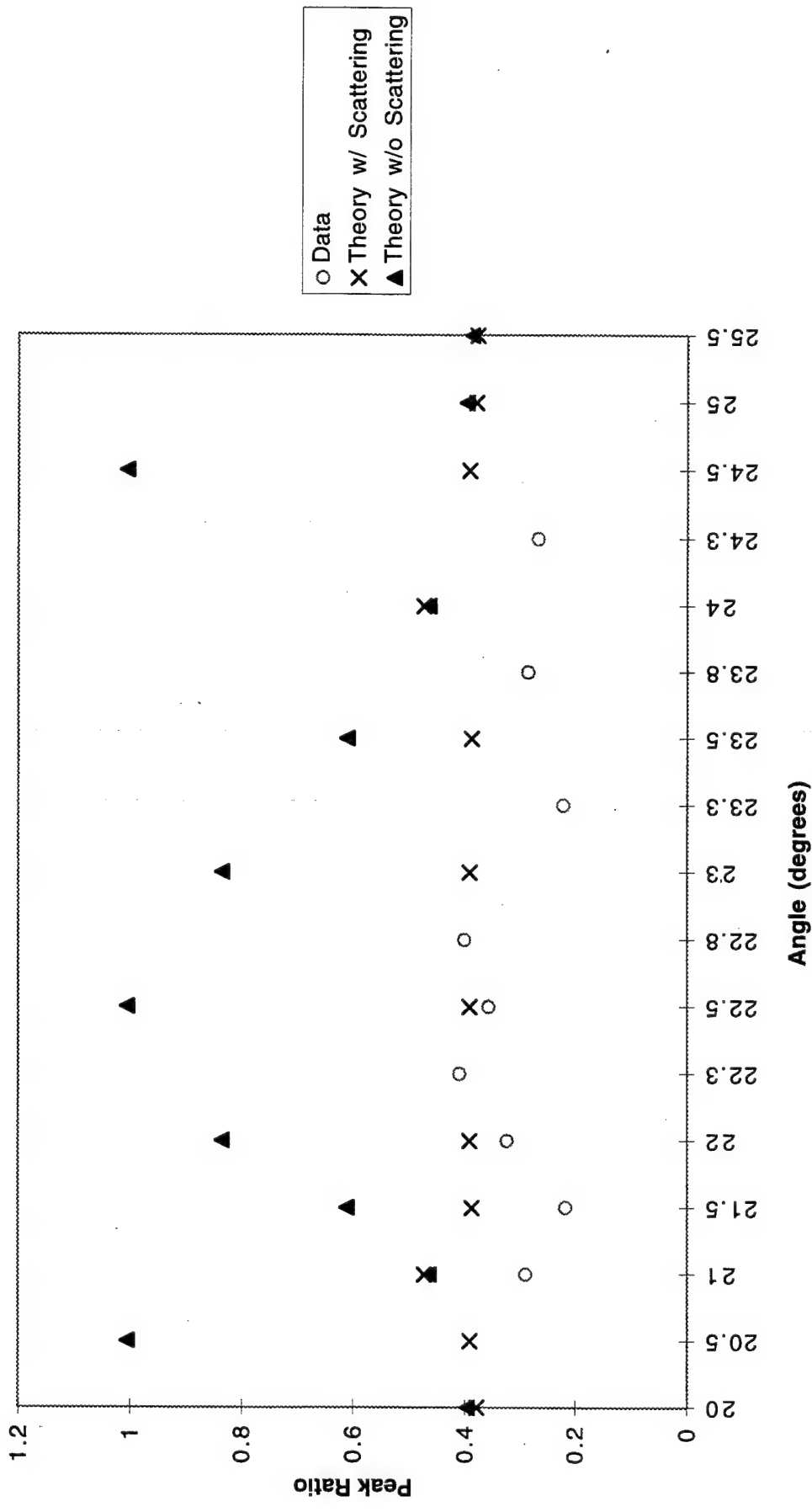


Figure (37). Data vs. Theory Intensity Ratios for the ZYH Crystal (Third Order Peak to the First Order Peak)  
Using Buckingham Ivey's Theoretical Peak Ratios

## V. DISCUSSION OF PREVIOUS RESULTS

A review of previous mosaic graphite experiments [Ref. 6,7] resulted in finding differences for calculating the PXR yield. Both DiNova's and Buckingham and Ivey's calculation for the effective thickness of tin was based on the assumption of a very thin target. Fluorescent x-rays are produced as the electron beam passes through the target and are simultaneously attenuated as the x-rays move through the foil. Equation (21) gives the effective thickness of the target foil based on the production and attenuation of the x-rays within the target. If the foil thickness is small compared to the inverse of  $(\mu\rho)_{Ag}$  then we can expand the exponential in Equation (21) and keep only the term linear in thickness,  $t$ :

$$t_{eff} \equiv \frac{t}{\sin\theta}, \quad t \ll \frac{1}{(\mu\rho)_{Ag}}. \quad (31)$$

Equation (31) which was used in Buckingham and Ivey's experiment was not a very good approximation. The wavelength corresponding to energy of 25.27 keV is  $4.91 \times 10^{-9}$  cm which is many orders of magnitude smaller than the tin foil thicknesses used in the previous experiments. Equation (21) was used to calculate the corrected effective thickness with  $\mu = 11.4 \text{ cm}^2/\text{g}$  (for a 25.3 keV x-ray),  $\rho = 7.3 \text{ g/cm}^3$  and  $t = 0.1389 \text{ cm}$ . Their yield was adjusted by direct multiplication of the ratio:  $t_{eff\,corr}/t_{eff\,prev}$ . As discussed in Buckingham and Ivey's thesis the effective thickness calculation in DiNova's thesis was  $t_{eff} = t/\cos\theta$ . For the geometry of the experiment dividing  $t$  by  $\sin\theta$  was the correct method. Her tin effective thickness was calculated and then divided out of her PXR yields. Appendix C. lists the previous and corrected tin effective thicknesses for the analysis. Also included are the other factors used in the previous yield calculations and the corrections required to adjust those yields. The additional factors are further discussed below. Table (1) shows the constants used to obtain the values listed in Appendix C.

	DiNova	DiNova	Buckingham & Ivey	Barrows
Solid Angle (sr.)	2.39E-03	2.00E-04	4.15E-04	15.96E-6
Solid Angle Correction (wrt Barrows)				
(wrt Ivey & Buckingham)	0.0067	0.0798	0.0385	N/A
Foil Thickness (cm)	Tin 2.75E-03	Tin 2.75E-03	Tin 1.52E-02(ZYA) 1.54E-02(ZYD) 1.56E-02(ZYH)	Silver 1.32E-02
Foil Density (g/cm <sup>3</sup> )	7.31	7.31	7.31	10.5
ZYA Thickness (cm)	0.1389	0.1389	0.1389	0.1389
ZYD Thickness (cm)	0.1659	0.1659	0.1659	0.1659
ZYD Thickness (cm)	0.1789	0.1789	0.1789	0.1789
Absorption Coefficients (cm <sup>2</sup> /g)				
Foil @ 25.27 keV	11.4	11.4	11.4	see Appendix B.
Crystal @ 25.27 keV	0.309	0.309	0.309	see Appendix B.

Table (1). Values of Constants Used for Appendix C. Results

DiNova's yield calculation included the tin attenuation factor,  $e^{-\mu p t_{eff}}$ , in the absorption term,  $a$ , and was calculated using the incorrect  $t_{eff}$ . Her tin attenuation factor was then divided out of the yield since it was accounted for in Equation (21).

Also, a corrected attenuation factor for the ZYA crystal was needed due a similar error in calculating the effective thickness of the crystal. Equation (19) was used to determine the corrected crystal absorption factor. It was also used for the previous

absorption factor by replacing the sine term with a cosine term. The PXR yield was further corrected by multiplication of the ratio: (corrected crystal attenuation factor)/(previous crystal attenuation factor).

Buckingham and Ivey's yield did not include a term for attenuation of the fluorescent x-rays due to the crystal. An attenuation factor was calculated using Equation (19) with  $\mu = 0.3 \text{ cm}^2/\text{g}$  (for a 25.3 keV x-ray),  $\rho = 2.26 \text{ g/cm}^3$  and  $t = 0.1389 \text{ cm}$  for each angle from the Bragg condition. Further correction to their previous yield was by multiplication of the calculated crystal absorption factor.

Solid angle corrections were made so as to compare the yields between the experiments. Figure (38) depicts DiNova's corrected near field and far field yields to Buckingham and Ivey's corrected near field yield. The yields are with respect to Buckingham and Ivey's solid angle of  $4.15 \times 10^{-4} \text{ sr.}$ . They are within a factor of two and exhibit the same behavior. Figure (39) shows the corrected ZYA crystal yields of the prior experiments and this experiment. The solid angles were corrected to that of the new data presented here. Again the yields are within a factor of two. Figures (40-42) show the yield comparison of the ZYA, ZYD and ZYH crystals for Buckingham and Ivey's results and this experiment. The ZYA and ZYD exhibit the same behavior and are very comparable in yields. It should be noted that the ZYD behavior from this experiment shows a deviation at the angles furthest from the Bragg condition. This deviation will be discussed in the next section. The ZYH yield comparison plot depicts large deviations in my results compared to the previous experiment and will be addressed in the next section.

Appendix C. presents the corrected yield, treated in the same manner as presented in this discussion, for the ZYA, ZYD and ZYH crystals for all experiments. DiNova's thesis used the ZYA crystal, whereas, Buckingham and Ivey's experiment and this thesis considered all three crystals.

## Photon Yield Comparison of Previous Experiments (0.45 Degree Mosaic Spread)

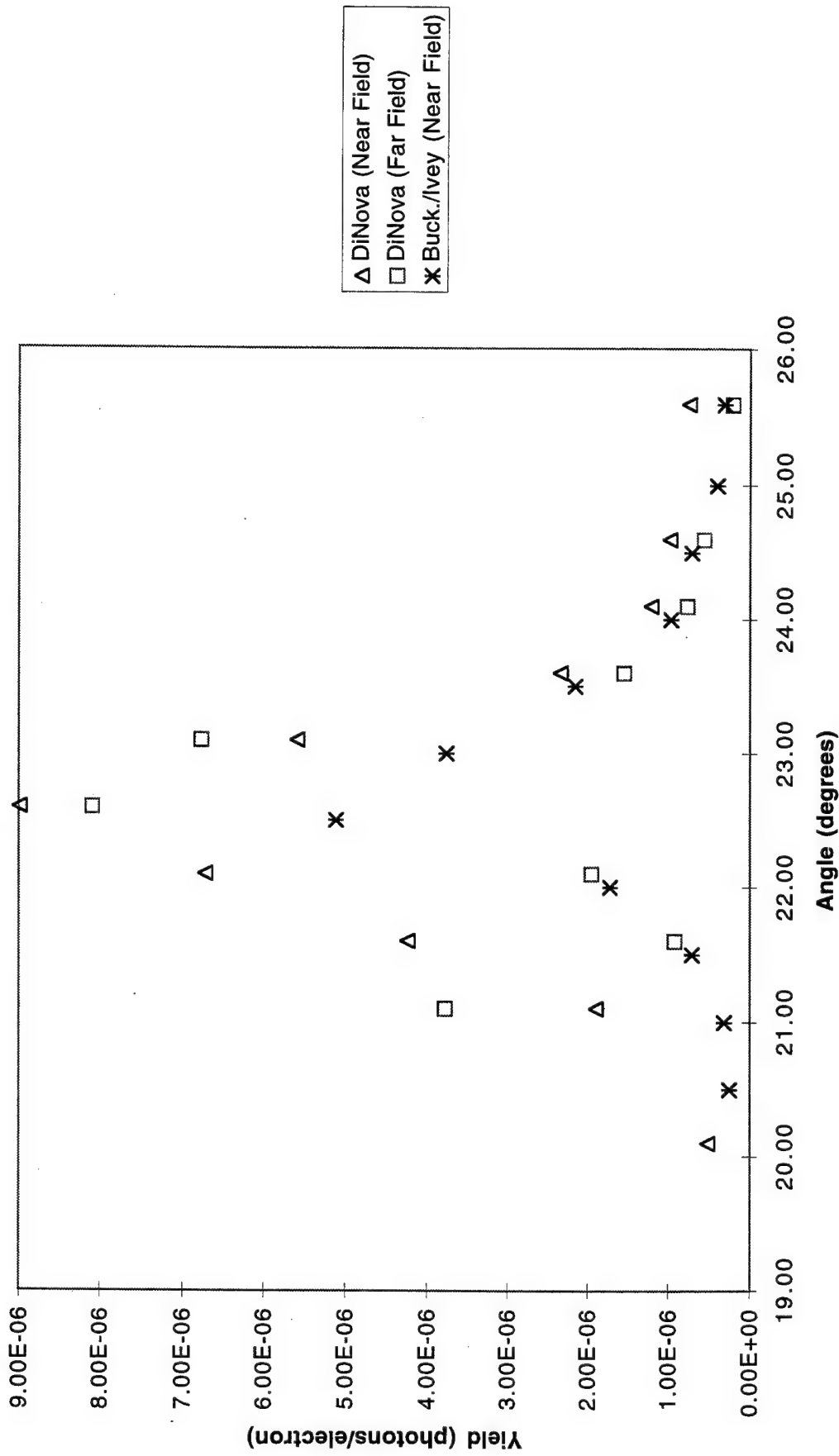


Figure (38). Observed Yield vs. Crystal Orientation Angle Corrected to a Solid Angle of 415 Micro-Steradians

## Photon Yield Comparison for all Experiments (0.45 Degree Mosaic Spread)

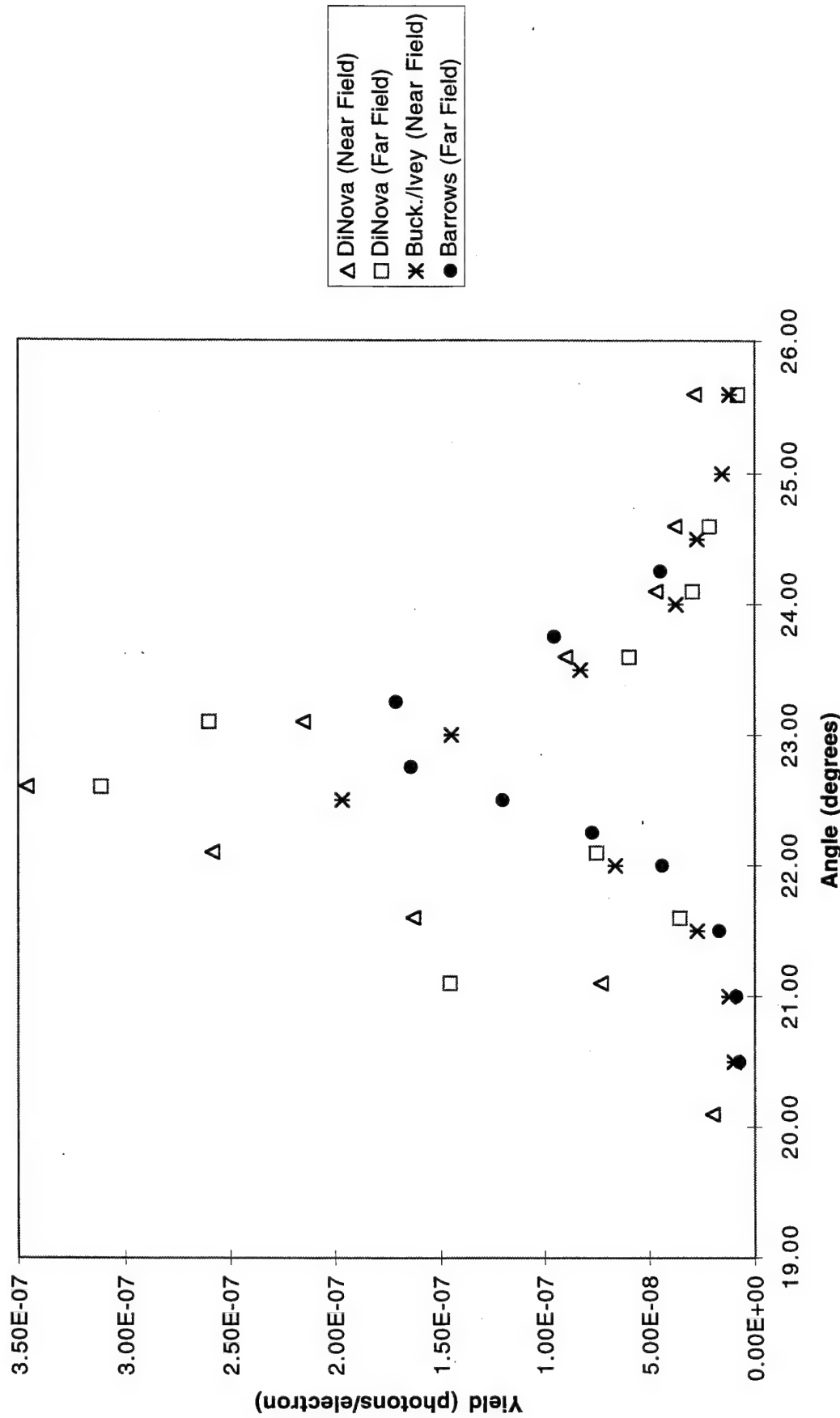


Figure (39). Observed Yield vs. Crystal Orientation Angle Corrected to a Solid Angle of 15.96 Micro-Steradians

## Photon Yield Comparison to Previous Experiment (0.45 Degree Mosaic Spread)

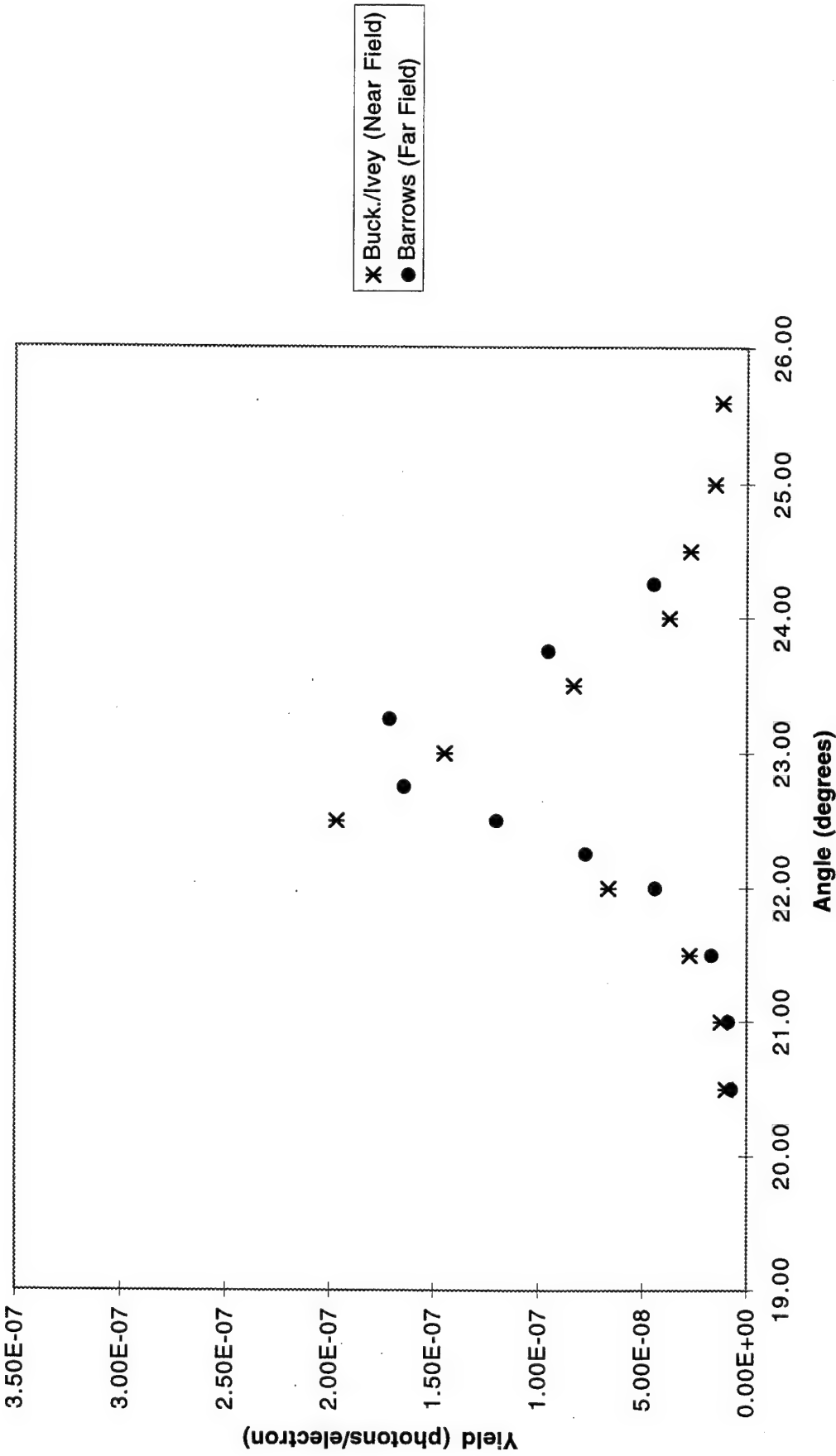


Figure (40). Observed Yield vs. Crystal Orientation Angle Corrected to a Solid Angle of 15.96 Micro-Steradians

## Photon Yield Comparison to Previous Experiment (1.31 Degree Mosaic Spread)

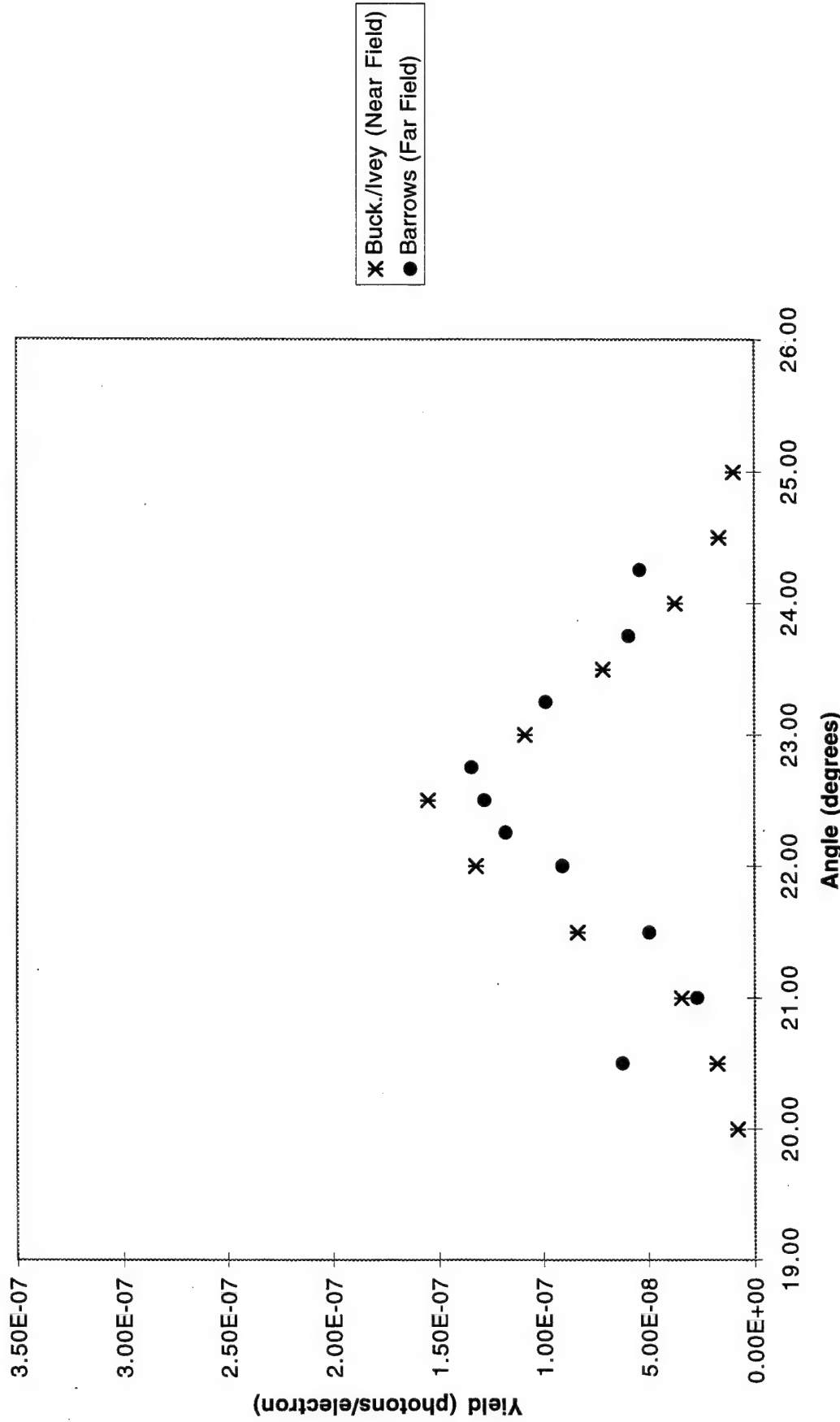


Figure (41). Observed Yield vs. Crystal Orientation Angle Corrected to a Solid Angle of 15.96 Micro-Steradians

## Photon Yield Comparison to Previous Experiment (2.5 Degree Mosaic Spread)

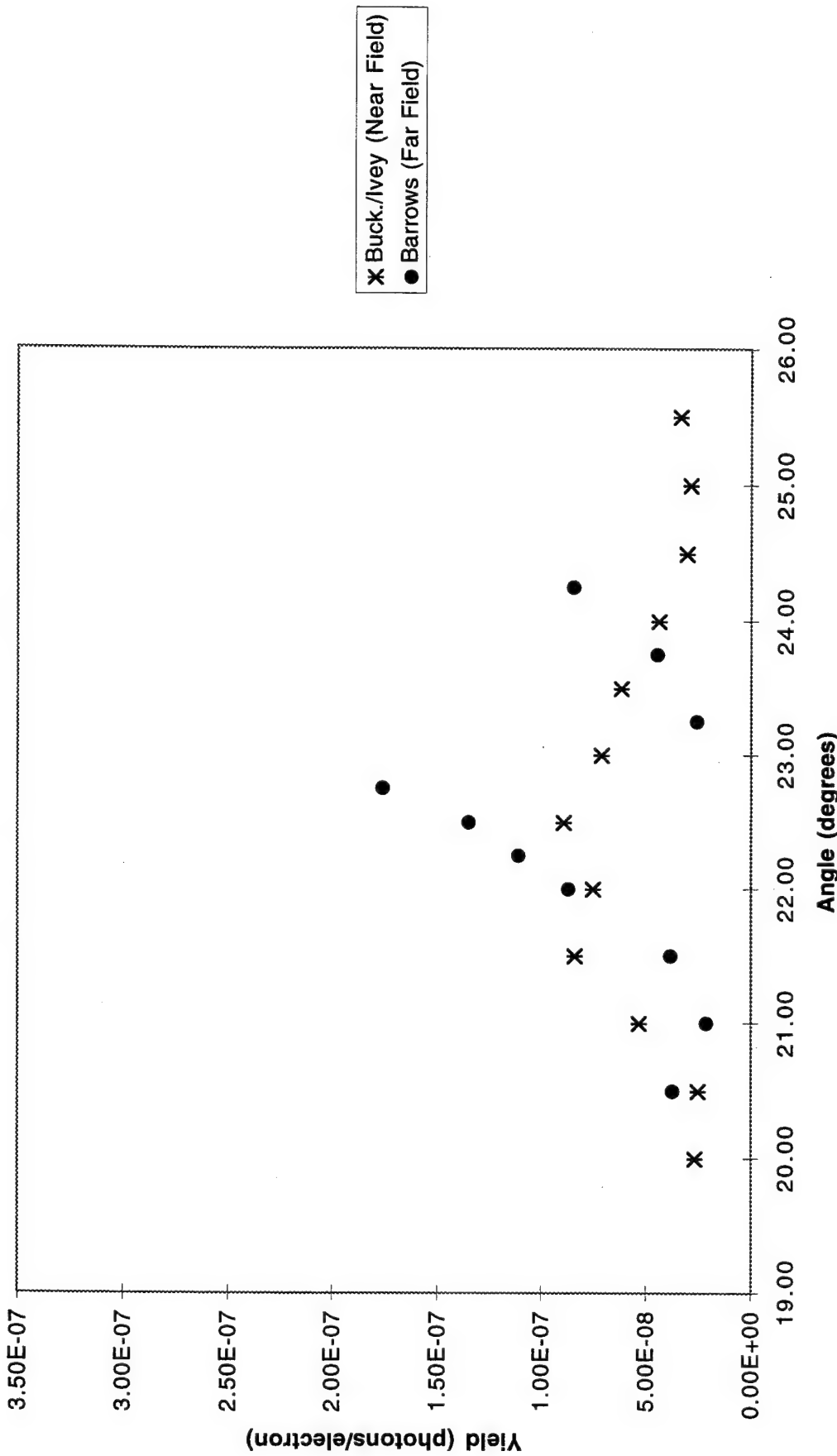


Figure (42). Observed Yield vs. Crystal Orientation Angle Corrected to a Solid Angle of 15.96 Micro-Steradians

## VI. DISCUSSION OF MOSAIC SPREAD

The radiation pattern of the PXR beam was shown in Figure (1) from a thin silicon crystal. Because of the different crystal structure, for thick mosaic graphite crystals the pattern shape would be different. How the pattern would appear for the crystals used in this experiment are not available since the calculation to obtain the pattern has not been performed. However, with mosaic crystals, it is known the microcrystallite structure varies significantly depending on the mosaic spread. The coherence condition for a perfect crystal is such that an integral number of virtual photon wavelengths fit along the path shown in Figure (2) and the resultant PXR beam pattern would remain the same no matter where the electron beam strikes the crystal. The unpredictability of the mosaic graphite microcrystallite structure would change the coherence conditions on different areas of the crystal, thus, changing the beam pattern.

The previous experiments used a much larger detector angular field of view, as discussed previously, in which the entire beam pattern was within the detector window. This experiment significantly narrowed the angular field of view in principle allowing the details of the PXR distribution to be more readily seen. A beam pattern with irregular peaks and valleys would result in the detector seeing different amounts of PXR using a narrow slit as the crystal was rotated. As mosaicity is increased, the irregularities would increase and would vary depending on where the electron beam was incident upon the crystal. Thus, PXR yield would be different at various points on the crystal due to changes in the coherence conditions. The narrow slit and the location of the incident electron beam contributed to the differences seen between the crystals. Figures (18-20) show this effect from the differences in mosaic spread. The shift in the peak yield from the Bragg angle ( $22.5^\circ$ ) can be attributed to the inaccuracies in determining the "home" position with the diffuse reflection of the laser and the narrow slit effect. Also, the intensity ratio plots would behave differently than expected as seen in Figures (24-26). Both the crystal yields from Buckingham and Ivey and from this experiment, as seen in

Figures (40-42), further illustrate the narrow slit and mosaic spread effects. The ZYA crystal yield plot is similar since the beam pattern was more consistent at different points on the crystal and the narrow slit did not affect the results as much. The ZYD and ZYH plots were progressively worse since the beam pattern was less consistent at different points and the slit began to affect the PXR detected. The results for the ZYH crystal for this experiment, presented in Figure (42), show that the electron beam was incident on an area of the crystal with a coherence condition different from that of Buckingham and Ivey's. DiNova's results on the ZYA crystal for both the "near" and "far" field were consistently higher by almost a factor of two as seen in Figure (38). The discrepancy is suspected to be an unaccounted normalization factor. However, the ZYA results from every experiment gave the highest PXR yields and the narrowest "rocking curves" as compared to the other crystals.

## VII. CONCLUSIONS AND RECOMMENDATIONS

The results from this experiment and re-analysis of previous experiments have shown that reproducible experimental results are extremely important. The thesis has uncovered the inconsistencies in the collection of data and the calculations of PXR yield which affected the yield and intensity results. Although the experiment should be modified to enhance the experimental outcome, care must be taken to ensure the other aspects of the experiment are performed in a similar manner. The collection of PXR data was very time intensive and limited the amount of data that could be collected from a crystal.

The methods used in calculating the PXR yield had a significant effect on the outcomes of each experiment as presented previously. The thin target assumption made in previous experiments and the omission of the crystal attenuation factor for the fluorescent x-rays led to these outcomes. Future experiments should incorporate the same equations used in this experiment for thick targets.

Each crystal in this experiment took two working days to collect the data. This led to errors in the crystal orientation angle, especially for the crystals with larger mosaicities, since determining the "home" position depended on the back reflection of the laser. Prior experiments used a mirror instead of the crystal face and it is recommended that future experiments use a mirror to determine the zero position.

Another systematic error in the experiment is the use of different programs to analyze the spectra and for attenuation calculations. PhotCoef and XCom [Ref. 21] were used in the analysis of the attenuation factors and only one should be used to minimize errors in obtaining the PXR yield. The attenuation factor differences were small (within 0.01 cm<sup>2</sup>/g), but for consistency the same program should be used.

The same should also apply for the curve fits of the data. QuattroPro [Ref. 22] was used by DiNova and PeakFit was used by Buckingham and Ivey and for this experiment to obtain the number of counts for the net areas. Again the errors would be small and the same program should be used in all experiments.

The foil backing on the crystals was changed to silver to prevent the overlap of the PXR fifth spectral order peak with the Cu K <sub>$\alpha$</sub>  line, as was the case in the previous experiments using the copper foil backing. This allowed a better calculation of the LINAC beam current and the resultant PXR yields. How this affected the differences in the PXR yields will be determined in future experiments utilizing a silver foil backing.

Lastly, the narrower detector angular field of view used in this experiment significantly increased the amount of time needed to collect the PXR spectrum data. Although the angular resolution was better, especially for large mosaic spreads, it made determination of the "home" position more difficult and led to an uncertainty in establishing the same crystal orientation to the electron beam on the succeeding day for the crystal data run.

Additional experiments should be run again on the mosaic graphite crystals using the same methods in this experiment to ensure the experimental errors are consistent so that a better comparison between the theory and experiment can be obtained.

## APPENDIX A. AVERAGE PEAK ENERGY APPROXIMATION

The linear attenuation coefficient is a function of energy and behaves in a non-linear fashion. The linear attenuation coefficient varies more for a change in energy across the lower order peaks than across the higher order peaks. In fact, the linear attenuation coefficient remains approximately constant across the higher energy peaks. Thus, an average energy across the lower energy peaks was required to determine the attenuation coefficient using PhotCoef. Analysis for the large number of channels (or energy) across the lower peaks proved to be cumbersome. Thus, an approximation was needed to evaluate the large amounts of data. The table below shows randomly selected energies of the first order peak for the ZYA crystal at 22.5 degrees. The centroid energy for the peak is 4.74 keV. The number of counts at each energy was obtained from the PCA-II ASCII data files. Also included are the linear attenuation coefficients at these energies for beryllium, kapton, carbon and air. Equation (14) was used to obtain the corrected counts at each energies.

Energy (keV)	Net Counts	Beryllium $\mu$ (cm <sup>2</sup> /g)	Kapton $\mu$ (cm <sup>2</sup> /g)	Carbon $\mu$ (cm <sup>2</sup> /g)	Air $\mu$ (cm <sup>2</sup> /g)	Corrected Counts
4.51	77	6.002	34.89	26.19	50.23	103.3
4.61	102	5.610	32.65	24.50	49.08	134.2
4.74	110	5.150	30.02	22.50	45.20	141.6
4.83	103	4.860	28.36	21.25	42.74	130.8
4.93	78	4.563	26.66	19.96	40.22	97.6

Table (1). Linear Attenuation Coefficients

Summing the Net Counts and the Corrected Counts in Table (1) resulted in a total count of 607.5 and 470.0, respectively. Equation (14) was solved using the total Net Count of 470.0 and the linear attenuation coefficients at the centroid energy given in Table

(1). A count of 605.1 resulted. This count of 605.1 was within 0.4% of the total Corrected Counts of 607.5 obtained by summing the Corrected Counts in Table (1). This turned out to be a very good approximation since the peaks were fitted with a Gaussian distribution in which the mean energy is the peak value of the distribution. Therefore, the peak centroid energies were used as the average energy across each peak in determining the corrected areas, and ultimately, the PXR yields as shown in Appendix B.

**APPENDIX B. TABLES OF PXR MEASUREMENTS**  
**(ZYA, 0.45 degree mosaic spread)**

Angle (degrees)	Peak Number (radians)	Peak Center (channel)	Peak Energy (keV)	Width @ HM (channels)	Background (counts)
20.50	1	194.44	4.40	39.09	241.43
0.3580	2	403.29	8.51	70.41	381.03
	Ag Peak	1096.94	22.17	33.54	96.31
21.00	1	196.87	4.45	30.38	408.33
0.3665	2	423.09	8.90	35.01	421.91
	Ag Peak	1097.36	22.17	36.67	290.06
21.50	1	192.08	4.36	33.82	263.16
0.3752	2	424.61	8.93	32.37	224.87
	3	660.94	13.59	46.14	281.40
	Ag Peak	1090.51	22.04	37.4	170.45
22.00	1	192.56	4.61	37.06	230.13
0.3840	2	428.21	9.24	38.12	208.58
	3	666.26	13.91	81.98	387.45
	Ag Peak	1080.32	22.05	32.95	113.00
22.25	1	194.05	4.64	33.81	347.18
0.3883	2	433.63	9.34	36.35	349.91
	3	674.42	14.07	33.77	303.27
	4	917.04	18.84	52.00	433.14
	Ag Peak	1081.34	22.07	37.07	292.44
22.50	1	211.24	4.74	33.93	402.47
0.3927	2	452.97	9.49	34.27	387.67
	3	693.84	14.23	39.11	421.00
	4	932.00	18.92	44.18	451.65
	Ag Peak	1096.37	22.16	34.35	338.32
22.75	1	202.30	4.80	34.78	224.38
0.3970	2	445.84	9.58	32.47	193.83
	3	686.71	14.32	37.40	205.44
	4	933.78	19.17	46.40	232.20
	Ag Peak	1084.76	22.14	33.98	159.90
23.25	1	207.48	4.90	33.60	313.29
0.4060	2	456.30	9.79	33.97	301.32
	3	704.30	14.66	34.78	292.77
	4	950.80	19.51	39.20	312.36
	Ag Peak	1086.54	22.17	34.47	266.13
23.75	1	212.24	4.72	36.23	309.64
0.4150	2	461.75	9.65	36.31	287.63
	3	716.75	14.69	38.48	280.25
	4	965.87	19.61	42.41	282.42
	Ag Peak	1086.68	22.00	40.57	257.90
24.25	1	220.18	4.88	41.91	554.70
0.4230	2	480.06	10.01	42.90	528.69
	3	732.07	14.99	47.41	542.36
	Ag Peak	1088.89	22.04	38.43	391.53

**APPENDIX B. TABLES OF PXR MEASUREMENTS**  
**(ZYA, 0.45 degree mosaic spread)**

Angle (degrees)	Uncorrected	Area	Area	Total	Atten. Coef.
	Area	Uncertainty	Uncertainty	Uncertainty	(Crystal)
	(counts)	(counts)	(percent)	(percent)	(cm <sup>2</sup> /g)
20.50	138.0	24.9	18.1	18.6	28.300
	66.6	28.8	43.2	43.5	3.810
	615.2	28.4	4.6		0.385
21.00	218.0	32.2	14.8	15.5	27.300
	109.1	30.9	28.3	28.7	3.330
	804.8	37.2	4.6		0.385
21.50	259.4	28.0	10.8	12.3	29.100
	101.4	23.5	23.2	23.9	3.300
	71.8	25.2	35.1	35.6	1.030
	499.1	29.0	5.8		0.388
22.00	658.9	33.5	5.1	7.6	24.500
	514.8	30.5	5.9	8.2	2.980
	271.3	32.3	11.9	13.2	0.971
	469.1	26.4	5.6		0.388
22.25	1785.1	49.8	2.8	5.7	24.000
	1657.5	48.6	2.9	5.8	2.890
	534.9	33.8	6.3	8.1	0.943
	128.5	31.5	24.6	25.1	0.494
	722.9	36.2	5.0		0.387
22.50	3626.9	66.6	1.8	4.6	22.500
	4146.8	70.2	1.7	4.6	2.760
	1735.7	50.8	2.9	5.2	0.917
	600.2	38.8	6.5	7.7	0.490
	943.8	40.3	4.3		0.385
22.75	2138.9	50.9	2.4	7.1	21.700
	2455.4	53.3	2.2	7.1	2.690
	1127.3	39.2	3.5	7.6	0.903
	393.8	29.3	7.4	10.0	0.478
	399.1	26.8	6.7		0.386
23.25	3322.1	62.8	1.9	6.0	20.300
	4464.4	71.2	1.6	5.9	2.520
	2019.9	51.0	2.5	6.2	0.853
	735.6	36.9	5.0	7.6	0.462
	592.1	33.5	5.7		0.385
23.75	1578.2	46.9	3.0	6.9	22.800
	1704.1	47.7	2.8	6.8	2.630
	710.4	35.6	5.0	8.0	0.849
	247.8	28.5	11.5	13.1	0.458
	515.2	32.1	6.2		0.389
24.25	1164.5	47.7	4.1	6.5	21.700
	957.7	44.9	4.7	6.9	2.370
	355.8	38.0	10.7	11.8	0.809
	792.4	39.7	5.0		0.388

**APPENDIX B. TABLES OF PXR MEASUREMENTS**  
**(ZYA, 0.45 degree mosaic spread)**

Angle (degrees)	Cry. Abs. Length (cm)	Atten. Fact. (Crystal)	Atten. Coef. (Kapton) (cm <sup>2</sup> /g)	Atten. Fact. (Kapton)	Atten. Coef. (Air) (cm <sup>2</sup> /g)	Atten. Fact. (Air)
20.50	0.016		37.591	0.875	56.368	0.884
	0.116		5.129	0.982	7.866	0.983
	1.150	0.708	0.460	0.998	0.611	0.999
21.00	0.016		36.329	0.879	54.509	0.888
	0.133		4.491	0.984	6.886	0.985
	1.150	0.714	0.460	0.998	0.611	0.999
21.50	0.015		38.642	0.872	57.917	0.881
	0.134		4.447	0.984	6.818	0.985
	0.430		1.367	0.995	2.035	0.996
	1.141	0.717	0.464	0.998	0.618	0.999
22.00	0.018		32.653	0.891	49.084	0.899
	0.148		4.019	0.986	6.161	0.987
	0.456		1.282	0.995	1.905	0.996
	1.142	0.723	0.464	0.998	0.618	0.999
22.25	0.018		32.019	0.893	48.148	0.900
	0.153		3.893	0.986	5.967	0.987
	0.469		1.243	0.996	1.844	0.996
	0.896		0.620	0.998	0.866	0.998
	1.143	0.725	0.463	0.998	0.617	0.999
22.50	0.020		30.022	0.899	45.196	0.906
	0.160		3.713	0.987	5.691	0.988
	0.483		1.205	0.996	1.786	0.996
	0.903		0.614	0.998	0.857	0.998
	1.149	0.728	0.461	0.998	0.612	0.999
22.75	0.020		28.903	0.902	43.540	0.910
	0.164		3.611	0.987	5.534	0.988
	0.490		1.184	0.996	1.754	0.996
	0.926		0.596	0.998	0.829	0.998
	1.148	0.731	0.461	0.998	0.613	0.999
23.25	0.022		27.158	0.908	40.957	0.915
	0.176		3.386	0.988	5.189	0.989
	0.519		1.110	0.996	1.641	0.996
	0.958		0.573	0.998	0.793	0.998
	1.150	0.737	0.460	0.998	0.611	0.999
23.75	0.019		30.408	0.898	45.767	0.905
	0.168		3.534	0.988	5.415	0.988
	0.521		1.104	0.996	1.631	0.996
	0.966		0.566	0.998	0.783	0.998
	1.138	0.739	0.466	0.998	0.620	0.999
24.25	0.020		27.495	0.907	41.457	0.914
	0.187		3.171	0.989	4.858	0.989
	0.547		1.045	0.996	1.540	0.997
	1.141	0.743	0.464	0.998	0.618	0.999

**APPENDIX B. TABLES OF PXR MEASUREMENTS**  
**(ZYA, 0.45 degree mosaic spread)**

<b>Angle (degrees)</b>	<b>Atten. Coef. (Be)</b>	<b>Atten. Fact. (Be)</b>	<b>Total Atten. Fact.</b>	<b>Detector Efficiency</b>	<b>Corrected Area</b>	<b>Atten. Coef. (Silver)</b>
					<b>(counts)</b>	<b>(cm<sup>2</sup>/g)</b>
20.50	6.476	0.942	0.729	0.99	191.2	
	0.964	0.991	0.957	1.00	69.6	
	0.212	0.998	0.995	0.90	687.0	13.908
21.00	6.255	0.944	0.737	0.99	298.8	
	0.863	0.992	0.962	1.00	113.4	
	0.212	0.998	0.995	0.90	898.7	13.908
21.50	6.661	0.940	0.723	0.99	362.5	
	0.856	0.992	0.962	1.00	105.4	
	0.368	0.997	0.987	1.00	72.7	
	0.213	0.998	0.995	0.90	557.3	14.130
22.00	5.610	0.949	0.760	0.99	875.9	
	0.786	0.993	0.966	1.00	533.1	
	0.353	0.997	0.988	1.00	274.5	
	0.213	0.998	0.995	0.90	523.9	14.113
22.25	5.499	0.950	0.764	0.99	2360.5	
	0.766	0.993	0.967	1.00	1714.6	
	0.345	0.997	0.988	1.00	541.2	
	0.240	0.998	0.994	0.97	133.3	
	0.213	0.998	0.995	0.90	807.2	14.079
22.50	5.150	0.954	0.777	0.99	4716.3	
	0.736	0.993	0.968	1.00	4283.2	
	0.338	0.997	0.989	1.00	1755.4	
	0.239	0.998	0.994	0.97	622.7	
	0.213	0.998	0.995	0.90	1053.9	13.925
22.75	4.954	0.955	0.784	1.00	2727.9	
	0.719	0.993	0.969	1.00	2534.0	
	0.334	0.997	0.989	1.00	1139.9	
	0.236	0.998	0.994	0.97	408.5	
	0.213	0.998	0.995	0.90	445.6	13.959
23.25	4.649	0.958	0.796	1.00	4175.3	
	0.681	0.994	0.971	1.00	4598.6	
	0.320	0.997	0.990	1.00	2041.1	
	0.231	0.998	0.994	0.96	770.7	
	0.212	0.998	0.995	0.90	661.2	13.908
23.75	5.217	0.953	0.774	0.99	2058.8	
	0.706	0.993	0.970	1.00	1757.5	
	0.319	0.997	0.990	1.00	717.8	
	0.230	0.998	0.994	0.96	259.7	
	0.213	0.998	0.995	0.90	575.3	14.200
24.25	4.780	0.957	0.793	1.00	1468.7	
	0.645	0.994	0.973	1.00	984.7	
	0.307	0.997	0.990	1.00	359.3	
	0.213	0.998	0.995	0.90	884.8	14.130

**APPENDIX B. TABLES OF PXR MEASUREMENTS**  
**(ZYA, 0.45 degree mosaic spread)**

Angle (degrees)	Eff. Thick. (Silver) (cm)	Peak Yield	Peak Yield	Experiment	Calculated
		(phot/elec)	Uncertainty (phot/elec)	Intensity	Intensity
20.50		7.27E-09	1.36E-09	1.000	1.000
		2.65E-09	1.15E-09	0.364	0.648
	0.00682				
21.00		8.75E-09	1.35E-09	1.000	1.000
		3.32E-09	9.52E-10	0.379	0.665
	0.00682				
21.50		1.69E-08	2.08E-09	1.000	1.000
		4.92E-09	1.17E-09	0.291	0.711
		3.39E-09	1.21E-09	0.200	0.289
	0.00671				
22.00		4.39E-08	3.32E-09	1.000	1.000
		2.67E-08	2.18E-09	0.609	0.625
		1.37E-08	1.81E-09	0.313	0.246
	0.00671				
22.25		7.72E-08	4.42E-09	1.000	1.000
		5.60E-08	3.25E-09	0.726	0.619
		1.77E-08	1.43E-09	0.229	0.242
		4.36E-09	1.09E-09	0.056	0.109
	0.00673				
22.50		1.20E-07	5.56E-09	1.000	1.000
		1.09E-07	4.99E-09	0.908	0.591
		4.46E-08	2.30E-09	0.372	0.228
		1.58E-08	1.22E-09	0.132	0.102
	0.00680				
22.75		1.64E-07	1.17E-08	1.000	1.000
		1.52E-07	1.08E-08	0.929	0.576
		6.86E-08	5.19E-09	0.418	0.220
		2.46E-08	2.46E-09	0.150	0.099
	0.00678				
23.25		1.71E-07	1.02E-08	1.000	1.000
		1.88E-07	1.11E-08	1.101	0.551
		8.36E-08	5.18E-09	0.489	0.207
		3.16E-08	2.39E-09	0.185	0.093
	0.00680				
23.75		9.52E-08	6.57E-09	1.000	1.000
		8.13E-08	5.55E-09	0.854	0.610
		3.32E-08	2.66E-09	0.349	0.233
		1.20E-08	1.57E-09	0.126	0.104
	0.00666				
24.25		4.46E-08	2.89E-09	1.000	1.000
		2.99E-08	2.05E-09	0.670	0.601
		1.09E-08	1.29E-09	0.245	0.223
	0.00668				

**APPENDIX B. TABLES OF PXR MEASUREMENTS**  
**(ZYD, 1.31 degree mosaic spread)**

Angle (degrees)	Peak Number	Peak Center	Peak Energy	Width @ HM	Background
(radians)		(counts)	(keV)	(channels)	(counts)
20.50	1	132.19	3.29	231.79	1266.03
0.3580	Ag Peak	1086.39	21.78	33.10	180.79
21.00	1	199.17	4.59	41.41	378.14
0.3670	2	435.90	9.17	57.69	482.12
	3	684.54	13.99	42.98	324.22
	Ag Peak	1086.56	21.79	33.30	207.39
21.50	1	197.40	4.55	38.29	267.17
0.3750	2	440.27	9.26	46.90	299.70
	3	684.09	13.98	75.96	440.62
	Ag Peak	1086.06	21.78	34.03	164.32
22.00	1	201.84	4.64	34.76	307.81
0.3840	2	442.23	9.30	42.33	353.94
	3	684.25	13.99	51.17	402.42
	4	932.90	18.81	48.36	355.62
	Ag Peak	1085.02	21.76	34.07	239.89
22.25	1	222.63	5.00	40.52	348.94
0.3880	2	465.24	9.69	43.57	356.94
	3	707.02	14.37	47.18	366.80
	4	952.03	19.12	41.01	301.47
	Ag Peak	1099.39	21.97	38.76	275.06
22.50	1	203.51	4.67	34.20	260.30
0.3930	2	446.76	9.38	38.03	272.28
	3	690.81	14.11	42.89	287.64
	4	936.90	18.90	43.77	273.55
	Ag Peak	1086.45	21.78	32.32	193.02
22.75	1	205.60	4.67	43.14	277.95
0.3970	2	452.39	9.44	48.39	293.84
	3	700.74	14.25	49.63	282.86
	4	945.87	19.00	46.33	246.99
	Ag Peak	1083.98	21.65	38.18	195.62
23.25	1	206.39	4.68	32.82	231.90
0.4060	2	455.64	9.51	36.45	239.20
	3	704.63	14.33	40.68	246.50
	4	956.72	19.21	59.27	328.96
	Ag Peak	1083.10	21.65	28.87	152.87
23.75	1	210.07	4.75	40.25	326.38
0.4150	2	462.66	9.64	42.32	314.75
	3	703.24	14.30	51.39	349.35
	Ag Peak	1081.93	21.63	31.12	180.23
24.25	1	211.88	4.79	57.89	359.50
0.4230	2	468.91	9.76	49.81	309.32
	3	695.95	14.16	173.50	1077.43
	Ag Peak	1085.02	21.69	32.38	201.08

**APPENDIX B. TABLES OF PXR MEASUREMENTS**  
**(ZYD, 1.31 degree mosaic spread)**

Angle (degrees)	Uncorrected	Area	Area	Total	Atten. Coef.
	Area	Uncertainty	Uncertainty	Uncertainty	(Crystal)
	(counts)	(counts)	(percent)	(percent)	(cm <sup>2</sup> /g)
20.50	657.8	56.5	8.6	10.5	68.400
	488.3	29.2	6.0		0.394
21.00	557.5	36.2	6.5	8.4	24.800
	407.8	37.0	9.1	10.6	3.050
	123.2	27.8	22.5	23.2	0.957
	591.0	31.7	5.4		0.394
21.50	702.6	35.2	5.0	8.3	25.500
	659.5	35.5	5.4	8.5	2.970
	357.2	35.2	9.9	11.9	0.958
	410.7	27.2	6.6		0.394
22.00	1749.1	48.6	2.8	6.5	24.000
	1919.7	51.3	2.7	6.4	2.930
	845.2	40.6	4.8	7.6	0.957
	333.1	32.3	9.7	11.3	0.495
	550.9	32.1	5.8		0.395
22.25	1437.5	46.2	3.2	9.5	19.100
	1725.9	49.4	2.9	9.4	2.600
	788.2	39.0	4.9	10.2	0.896
	302.6	30.1	9.9	13.4	0.480
	331.6	29.7	9.0		0.390
22.50	2208.3	52.2	2.4	6.4	23.600
	2752.8	57.4	2.1	6.3	2.860
	1264.4	42.9	3.4	6.9	0.937
	518.8	32.6	6.3	8.7	0.491
	496.8	29.7	6.0		0.394
22.75	1538.3	45.8	3.0	8.7	23.600
	2312.5	53.9	2.3	8.5	2.800
	1063.8	40.4	3.8	9.0	0.914
	394.6	29.8	7.6	11.1	0.486
	328.8	26.8	8.2		0.397
23.25	1169.9	40.4	3.5	8.7	23.400
	1450.1	43.9	3.0	8.6	2.740
	720.4	34.8	4.8	9.4	0.902
	293.1	30.8	10.5	13.2	0.476
	308.8	24.8	8.0		0.397
23.75	733.4	37.2	5.1	9.1	22.400
	700.2	36.5	5.2	9.2	2.640
	344.5	32.3	9.4	12.0	0.906
	353.3	26.7	7.6		0.398
24.25	635.9	36.8	5.8	10.0	21.800
	396.8	31.9	8.0	11.4	2.550
	343.8	50.0	14.5	16.6	0.929
	334.7	27.1	8.1		0.396

**APPENDIX B. TABLES OF PXR MEASUREMENTS**  
**(ZYD, 1.31 degree mosaic spread)**

Angle (degrees)	Cry. Abs. Length (cm)	Atten. Fact. (Crystal)	Atten. Coef. (Kapton) (cm <sup>2</sup> /g)	Atten. Fact. (Kapton)	Atten. Coef. (Air) (cm <sup>2</sup> /g)	Atten. Fact. (Air)
20.50	0.006		89.938	0.727	132.280	0.750
	1.123	0.656	0.473	0.998	0.632	0.999
21.00	0.018		33.084	0.889	49.721	0.897
	0.145		4.110	0.986	6.301	0.986
	0.462		1.262	0.996	1.874	0.996
	1.124	0.663	0.473	0.998	0.632	0.999
21.50	0.017		33.971	0.886	51.030	0.895
	0.149		3.993	0.986	6.121	0.987
	0.462		1.265	0.996	1.878	0.996
	1.123	0.668	0.473	0.998	0.632	0.999
22.00	0.018		32.019	0.893	48.148	0.900
	0.151		3.943	0.986	6.043	0.987
	0.462		1.262	0.996	1.847	0.996
	0.894		0.622	0.998	0.869	0.998
	1.121	0.674	0.474	0.998	0.634	0.999
22.25	0.023		25.550	0.913	38.574	0.919
	0.170		3.491	0.988	5.349	0.988
	0.494		1.173	0.996	1.737	0.996
	0.922		0.600	0.998	0.834	0.998
	1.136	0.680	0.467	0.998	0.622	0.999
22.50	0.019		31.402	0.895	47.236	0.902
	0.155		3.844	0.986	5.891	0.987
	0.472		1.233	0.996	1.829	0.996
	0.901		0.615	0.998	0.859	0.998
	1.123	0.680	0.473	0.998	0.632	0.999
22.75	0.019		31.402	0.895	47.236	0.902
	0.158		3.772	0.987	5.781	0.987
	0.484		1.200	0.996	1.778	0.996
	0.910		0.608	0.998	0.848	0.998
	1.114	0.680	0.478	0.998	0.640	0.999
23.25	0.019		3.120	0.989	46.937	0.903
	0.161		3.690	0.987	5.656	0.988
	0.491		1.182	0.996	1.750	0.996
	0.930		0.593	0.998	0.825	0.998
	1.114	0.686	0.478	0.998	0.640	0.999
23.75	0.020		29.831	0.900	44.914	0.907
	0.168		3.545	0.987	5.432	0.988
	0.488		1.189	0.996	1.415	0.997
	1.112	0.691	0.478	0.998	0.641	0.999
24.25	0.020		29.085	0.902	35.790	0.925
	0.174		3.417	0.988	4.171	0.991
	0.476		1.221	0.996	1.455	0.997
	1.117	0.696	0.476	0.998	0.637	0.999

**APPENDIX B. TABLES OF PXR MEASUREMENTS**  
**(ZYD, 1.31 degree mosaic spread)**

Angle (degrees)	Atten. Coef. (Be)	Atten. Fact. (Be)	Total	Detector Efficiency	Corrected	Atten. Coef. (Silver) (cm <sup>2</sup> /g)
			Atten. Fact.		Area (counts)	
20.50	15.959	0.863	0.470	0.97	1442.7	
	0.215	0.998	0.995	0.92	533.5	14.589
21.00	5.686	0.949	0.757	0.99	743.9	
	0.801	0.993	0.965	1.00	422.6	
	0.349	0.997	0.988	1.00	124.7	
	0.215	0.998	0.995	0.92	645.6	14.571
21.50	5.841	0.947	0.751	0.99	944.4	
	0.782	0.993	0.966	1.00	682.8	
	0.349	0.997	0.988	1.00	361.5	
	0.215	0.998	0.995	0.92	448.7	14.589
22.00	5.499	0.950	0.764	0.99	2312.9	
	0.774	0.993	0.966	1.00	1986.7	
	0.349	0.997	0.988	1.00	855.2	
	0.241	0.998	0.994	0.97	345.6	
	0.215	0.998	0.995	0.92	601.8	14.625
22.25	4.369	0.960	0.806	1.00	1782.4	
	0.699	0.994	0.970	1.00	1779.4	
	0.332	0.997	0.989	1.00	797.0	
	0.236	0.998	0.994	0.96	317.2	
	0.214	0.998	0.995	0.90	370.3	14.252
22.50	5.391	0.951	0.768	0.99	2905.1	
	0.758	0.993	0.967	1.00	2846.5	
	0.343	0.997	0.989	1.00	1279.1	
	0.239	0.998	0.994	0.96	543.8	
	0.215	0.998	0.995	0.92	542.7	14.589
22.75	5.391	0.951	0.768	0.99	2023.6	
	0.746	0.993	0.968	1.00	2389.7	
	0.337	0.997	0.989	1.00	1075.9	
	0.238	0.998	0.994	0.96	413.5	
	0.215	0.998	0.995	0.93	355.3	14.827
23.25	5.356	0.952	0.850	0.99	1390.7	
	0.732	0.993	0.968	1.00	1497.5	
	0.334	0.997	0.989	1.00	728.4	
	0.235	0.998	0.994	0.96	307.2	
	0.215	0.998	0.995	0.93	333.7	14.827
23.75	5.116	0.954	0.778	0.99	952.1	
	0.708	0.993	0.970	1.00	722.2	
	0.335	0.997	0.990	1.00	348.1	
	0.215	0.998	0.995	0.93	381.8	14.864
24.25	4.986	0.955	0.797	0.99	806.3	
	0.687	0.994	0.973	1.00	407.8	
	0.341	0.997	0.989	1.00	347.5	
	0.215	0.998	0.995	0.93	361.7	14.753

**APPENDIX B. TABLES OF PXR MEASUREMENTS**  
**(ZYD, 1.31 degree mosaic spread)**

<b>Angle (degrees)</b>	<b>Eff. Thickness (Silver) (cm)</b>	<b>Peak Yield</b>	<b>Peak Yield Uncertainty</b>	<b>Experiment Intensity</b>	<b>Calculated Intensity</b>
		<b>(phot/elec)</b>	<b>(phot/elec)</b>	<b>Ratios</b>	<b>Ratios</b>
20.50		6.24E-08	6.53E-09	1.000	1.000
	0.00651				
21.00		2.69E-08	2.27E-09	1.000	
		1.53E-08	1.61E-09	0.568	0.693
		4.51E-09	1.04E-09	0.168	0.289
	0.00651				
21.50		4.94E-08	4.10E-09	1.000	1.000
		3.57E-08	3.05E-09	0.723	0.721
		1.89E-08	2.25E-09	0.383	0.298
	0.00650				
22.00		9.08E-08	5.86E-09	1.000	1.000
		7.80E-08	5.00E-09	0.859	0.683
		3.36E-08	2.54E-09	0.370	0.280
		1.36E-08	1.54E-09	0.149	0.128
	0.00648				
22.25		1.18E-07	1.12E-08	1.000	1.000
		1.17E-07	1.10E-08	0.998	0.572
		5.26E-08	5.38E-09	0.447	0.225
		2.09E-08	2.80E-09	0.178	0.102
	0.00665				
22.50		1.28E-07	8.22E-09	1.000	1.000
		1.25E-07	7.93E-09	0.980	0.679
		5.63E-08	3.87E-09	0.440	0.276
		2.39E-08	2.08E-09	0.187	0.126
	0.00649				
22.75		1.34E-07	1.16E-08	1.000	1.000
		1.58E-07	1.34E-08	1.181	0.685
		7.12E-08	6.41E-09	0.532	0.278
		2.74E-08	3.04E-09	0.204	0.126
	0.00639				
23.25		9.87E-08	8.63E-09	1.000	1.000
		1.06E-07	9.12E-09	1.077	0.685
		5.17E-08	4.85E-09	0.524	0.276
		2.18E-08	2.89E-09	0.221	0.126
	0.00639				
23.75		5.93E-08	5.40E-09	1.000	1.000
		4.50E-08	4.13E-09	0.759	0.667
		2.17E-08	2.61E-09	0.366	0.264
	0.00637				
24.25		5.38E-08	5.36E-09	1.000	1.000
		2.72E-08	3.11E-09	0.506	0.658
		2.32E-08	3.86E-09	0.431	0.256
	0.00641				

**APPENDIX B. TABLES OF PXR MEASUREMENTS**  
**(ZYH, 2.5 degree mosaic spread)**

Angle (degrees)	Peak Number	Peak Center (channel)	Peak Energy (keV)	Width @ HM (channels)	Background (counts)
20.50	1	174.71	3.98	121.20	862.66
0.3578	Ag Peak	1088.87	22.04	37.57	267.41
21.00	1	196.14	4.56	38.92	392.72
0.3665	2	443.51	9.41	58.40	523.90
	3	692.90	14.29	67.49	529.26
	Ag Peak	1090.63	22.08	32.13	194.13
21.50	1	203.17	4.70	37.24	276.78
0.3752	2	440.56	9.35	40.60	268.73
	3	691.88	14.27	42.94	247.25
	4	917.40	18.69	24.19	120.59
	Ag Peak	1087.89	22.03	40.31	177.41
22.00	1	203.75	4.71	35.13	458.36
0.3840	2	446.72	9.47	40.97	487.52
	3	691.01	14.25	43.13	463.43
	4	934.60	19.02	33.72	323.50
	Ag Peak	1085.63	21.98	42.44	376.86
22.25	1	203.64	4.71	35.11	277.33
0.3883	2	446.86	9.47	37.91	267.99
	3	690.20	14.24	47.57	296.78
	4	933.98	19.01	35.14	190.00
	Ag Peak	1084.04	21.95	33.82	165.55
22.50	1	206.86	4.61	38.85	364.63
0.3927	2	450.77	9.43	42.51	398.98
	3	695.39	14.27	54.79	514.23
	4	935.76	19.02	52.26	490.48
	Ag Peak	1090.24	22.07	35.37	331.96
22.75	1	204.60	4.73	41.39	275.86
0.3971	2	450.46	9.54	43.36	288.99
	3	694.20	14.32	44.82	298.72
	4	937.07	19.07	44.50	296.58
	Ag Peak	1084.40	21.96	35.86	239.00
23.25	1	193.35	4.56	34.05	679.70
0.4058	2	434.24	9.31	47.24	852.62
	3	687.47	14.32	77.59	1244.35
	Ag Peak	1083.02	22.13	34.37	443.24
23.75	1	199.89	4.69	33.75	416.14
0.4145	2	441.29	9.45	43.22	489.68
	3	683.14	14.23	43.86	453.00
	Ag Peak	1085.47	22.18	26.54	229.89
24.25	1	199.22	4.67	34.71	240.73
0.4232	2	445.95	9.55	39.61	253.53
	3	687.38	14.31	38.79	227.98
	Ag Peak	1085.65	22.18	31.18	156.33

**APPENDIX B. TABLES OF PXR MEASUREMENTS**  
**(ZYH, 2.5 degree mosaic spread)**

Angle	Uncorrected	Area	Area	Total	Atten. Coef.
	Area (degrees)	Uncertainty (counts)	Uncertainty (percent)	Uncertainty (percent)	(Crystal) (cm <sup>2</sup> /g)
20.50	589.3	48.1	8.2	10.3	38.400
	513.4	32.4	6.3		0.388
21.00	368.9	34.0	9.2	11.0	25.300
	340.1	37.3	11.0	12.5	2.830
	141.6	34.6	24.5	25.2	0.908
	498.6	29.8	6.0		0.387
21.50	471.5	32.0	6.8	10.3	23.100
	334.7	29.5	8.8	11.7	2.880
	133.0	25.1	18.8	20.4	0.911
	57.9	17.3	29.9	30.9	0.501
	341.3	26.4	7.7		0.388
22.00	1730.1	51.4	3.0	7.2	22.900
	1773.7	52.4	3.0	7.2	2.780
	721.5	40.6	5.6	8.6	0.914
	190.3	28.9	15.2	16.6	0.485
	550.9	36.1	6.6		0.389
22.25	1290.6	43.0	3.3	8.6	22.900
	1459.9	44.7	3.1	8.5	2.780
	681.8	35.7	5.2	9.5	0.916
	160.7	23.3	14.5	16.5	0.485
	321.4	25.5	7.9		0.390
22.50	2068.3	52.9	2.6	8.0	24.500
	2136.6	54.2	2.5	8.0	2.810
	971.0	44.7	4.6	8.8	0.911
	280.0	35.5	12.7	14.8	0.485
	440.5	33.2	7.5		0.387
22.75	2357.2	53.9	2.3	8.2	22.700
	2967.8	59.5	2.0	8.1	2.720
	1216.1	42.6	3.5	8.6	0.903
	473.6	32.7	6.9	10.4	0.482
	372.3	29.2	7.8		0.390
23.25	924.9	47.8	5.2	6.6	25.300
	712.5	49.2	6.9	8.1	2.920
	270.9	52.5	19.4	19.8	0.903
	1065.2	44.2	4.1		0.386
23.75	799.0	40.4	5.1	7.8	23.200
	755.0	41.6	5.5	8.1	2.800
	295.2	34.7	11.7	13.2	0.917
	527.7	31.4	6.0		0.385
24.25	808.6	35.9	4.4	9.7	23.600
	877.8	37.2	4.2	9.6	2.710
	279.4	27.1	9.7	13.0	0.905
	284.0	24.4	8.6		0.385

**APPENDIX B. TABLES OF PXR MEASUREMENTS**  
**(ZYH, 2.5 degree mosaic spread)**

Angle (degrees)	Cry. Abs. Length (cm)	Atten. Fact.	Atten. Coef.	Atten. Fact.	Atten. Coef.	Atten. Fact.
		(Crystal)	(Kapton)	(Kapton)	(Air)	(Air)
20.50	0.012		50.889	0.835	75.904	0.848
	1.141	0.639	0.464	0.998	0.618	0.999
21.00	0.017		33.746	0.887	50.698	0.895
	0.156		3.808	0.987	5.836	0.987
	0.487		1.191	0.996	1.764	0.996
	1.144	0.646	0.463	0.998	0.616	0.999
21.50	0.019		30.800	0.896	46.347	0.904
	0.154		3.880	0.986	5.948	0.987
	0.486		1.195	0.996	1.771	0.996
	0.883		0.631	0.998	0.884	0.998
	1.140	0.652	0.465	0.998	0.619	0.999
22.00	0.019		30.603	0.897	46.056	0.905
	0.159		3.737	0.987	5.727	0.988
	0.484		1.200	0.996	1.778	0.996
	0.912		0.607	0.998	0.845	0.998
	1.137	0.657	0.466	0.998	0.621	0.999
22.25	0.019		30.603	0.897	46.056	0.905
	0.159		3.737	0.987	5.727	0.988
	0.483		1.202	0.996	1.782	0.996
	0.912		0.607	0.998	0.847	0.998
	1.135	0.659	0.467	0.998	0.623	0.999
22.50	0.018		32.653	0.891	49.084	0.899
	0.157		3.784	0.987	5.799	0.987
	0.486		1.195	0.996	1.771	0.996
	0.912		0.607	0.998	0.845	0.998
	1.143	0.664	0.463	0.998	0.617	0.999
22.75	0.019		30.214	0.898	45.480	0.906
	0.163		3.656	0.987	5.621	0.988
	0.490		1.184	0.996	1.754	0.996
	0.918		0.603	0.998	0.840	0.998
	1.135	0.665	0.467	0.998	0.623	0.999
23.25	0.017		33.746	0.887	50.698	0.895
	0.152		3.930	0.986	6.024	0.987
	0.490		1.184	0.996	1.754	0.996
	1.147	0.674	0.461	0.998	0.613	0.999
23.75	0.019		30.999	0.896	46.641	0.903
	0.158		3.760	0.987	5.763	0.988
	0.483		1.205	0.996	1.786	0.996
	1.151	0.680	0.460	0.998	0.611	0.999
24.25	0.019		31.402	0.895	47.236	0.902
	0.163		3.645	0.987	5.585	0.988
	0.489		1.186	0.996	1.757	0.996
	1.151	0.685	0.460	0.998	0.611	0.999

**APPENDIX B. TABLES OF PXR MEASUREMENTS**  
**(ZYH, 2.5 degree mosaic spread)**

Angle (degrees)	Atten. Coef.	Atten. Fact.	Total	Detector	Corrected	Atten. Coef.
	(Be) (cm <sup>2</sup> /g)	(Be)	Atten. Fact.	Efficiency	Area (counts)	(cm <sup>2</sup> /g)
20.50	8.821	0.922	0.481	0.98	922.0	
	0.213	0.998	0.992	0.90	573.3	14.130
21.00	5.802	0.948	0.613	0.99	494.9	
	0.752	0.993	0.945	1.00	351.5	
	0.336	0.997	0.983	1.00	143.2	
	0.213	0.998	0.992	0.90	556.7	14.061
21.50	5.286	0.952	0.640	0.99	617.2	
	0.764	0.993	0.944	1.00	346.2	
	0.336	0.997	0.983	1.00	134.5	
	0.242	0.998	0.991	0.97	60.0	
	0.213	0.998	0.992	0.90	381.1	14.147
22.00	5.251	0.953	0.641	0.99	2260.8	
	0.740	0.993	0.946	1.00	1832.4	
	0.337	0.997	0.983	1.00	729.7	
	0.238	0.998	0.991	0.98	195.4	
	0.213	0.998	0.992	0.90	615.1	14.234
22.25	5.251	0.953	0.641	0.99	1686.5	
	0.740	0.993	0.946	1.00	1508.2	
	0.338	0.997	0.982	1.00	689.5	
	0.238	0.998	0.991	0.98	165.0	
	0.214	0.998	0.992	0.90	358.9	14.287
22.50	5.610	0.949	0.623	0.99	2749.6	
	0.748	0.993	0.945	1.00	2208.3	
	0.336	0.997	0.983	1.00	981.9	
	0.238	0.998	0.991	0.98	287.5	
	0.213	0.998	0.992	0.90	491.8	14.079
22.75	5.183	0.953	0.645	0.99	3070.2	
	0.727	0.993	0.947	1.00	3064.1	
	0.334	0.997	0.983	1.00	1229.6	
	0.237	0.998	0.991	0.98	486.3	
	0.214	0.998	0.992	0.90	415.8	14.269
23.25	5.802	0.948	0.613	0.99	1240.8	
	0.772	0.993	0.943	1.00	737.3	
	0.334	0.997	0.983	1.00	273.9	
	0.213	0.998	0.992	0.90	1189.4	13.976
23.75	5.321	0.952	0.638	0.99	1047.5	
	0.744	0.993	0.946	1.00	780.2	
	0.338	0.997	0.982	1.00	298.6	
	0.212	0.998	0.992	0.90	589.3	13.891
24.25	5.391	0.951	0.634	0.99	1063.7	
	0.725	0.993	0.947	1.00	906.2	
	0.335	0.997	0.983	1.00	282.5	
	0.212	0.998	0.992	0.90	317.1	13.891

**APPENDIX B. TABLES OF PXR MEASUREMENTS**  
**(ZYH, 2.5 degree mosaic spread)**

Angle (degrees)	Eff. Thick. (Silver) (cm)	Peak Yield (phot/elec)	Peak Yield Uncertainty (phot/elec)	Experiment Intensity	Calculated Intensity
				Ratios	Ratios
20.50		3.73E-08	3.85E-09	1.000	1.000
	0.00672				
21.00		2.10E-08	2.30E-09	1.000	1.000
		1.49E-08	1.86E-09	0.710	0.762
		6.06E-09	1.53E-09	0.289	0.317
	0.00674				
21.50		3.82E-08	3.93E-09	1.000	1.000
		2.15E-08	2.52E-09	0.561	0.690
		8.33E-09	1.70E-09	0.218	0.289
		3.72E-09	1.15E-09	0.097	0.132
	0.00670				
22.00		8.69E-08	6.26E-09	1.000	1.000
		7.04E-08	5.07E-09	0.811	0.695
		2.81E-08	2.42E-09	0.323	0.287
		7.51E-09	1.24E-09	0.086	0.131
	0.00666				
22.25		1.11E-07	9.57E-09	1.000	1.000
		9.94E-08	8.46E-09	0.894	0.695
		4.54E-08	4.32E-09	0.409	0.287
		1.09E-08	1.79E-09	0.098	0.131
	0.00663				
22.50		1.35E-07	1.08E-08	1.000	1.000
		1.08E-07	8.63E-09	0.803	0.740
		4.82E-08	4.26E-09	0.357	0.307
		1.41E-08	2.08E-09	0.105	0.141
	0.00672				
22.75		1.76E-07	1.44E-08	1.000	1.000
		1.76E-07	1.42E-08	0.998	0.696
		7.06E-08	6.06E-09	0.401	0.285
		2.79E-08	2.91E-09	0.158	0.130
	0.00663				
23.25		2.57E-08	1.70E-09	1.000	1.000
		1.53E-08	1.23E-09	0.594	0.750
		5.68E-09	1.13E-09	0.221	0.317
	0.00676				
23.75		4.44E-08	3.47E-09	1.000	1.000
		3.31E-08	2.69E-09	0.745	0.702
		1.27E-08	1.67E-09	0.285	0.290
	0.00680				
24.25		8.44E-08	8.17E-09	1.000	1.000
		7.19E-08	6.89E-09	0.852	0.725
		2.24E-08	2.91E-09	0.266	0.296
	0.00679				



**APPENDIX C. YIELD COMPARISON BETWEEN PREVIOUS AND CURRENT EXPERIMENTS**  
**(ZYA, 0.45 degree mosaic spread)**

Angle (degrees)	Prev. Yield-NF (DiNova)	Prev. Yield-FF (DiNova)	Previous Tin Eff. Thick. (DiNova)	Corrected Tin Eff. Thick. (DiNova)	Previous Tin (DiNova)	Corrected ZYA Atten. Fact. (DiNova)	Corrected ZYA Atten. Fact. (DiNova)	Previous ZYA Atten. Fact. (DiNova)
20.10	1.39E-06		0.002928	0.005828	0.7827	0.7541	0.7541	0.9019
20.50								
21.00								
21.10	5.26E-06	8.77E-07	0.002948	0.005639	0.7815	0.7638	0.7638	0.9013
21.50								
21.60	1.19E-05	2.16E-07	0.002958	0.005549	0.7808	0.7684	0.7684	0.9009
22.00								
22.10	1.91E-05	4.64E-07	0.002968	0.005463	0.7801	0.7727	0.7727	0.9006
22.25								
22.50								
22.60	2.59E-05	1.95E-06	0.002979	0.005379	0.7794	0.7769	0.7769	0.9003
22.75								
23.00								
23.10	1.63E-05	1.65E-06	0.002990	0.005298	0.7787	0.7810	0.7810	0.8999
23.25								
23.50								
23.60	6.89E-06	3.82E-07	0.003001	0.005220	0.7780	0.7848	0.7848	0.8996
23.75								
24.00								
24.10	3.61E-06	1.90E-07	0.003013	0.005144	0.7772	0.7886	0.7886	0.8992
24.25								
24.50								
24.60	2.96E-06	1.40E-07	0.003025	0.005070	0.7765	0.7921	0.7921	0.8988
25.00								
25.60	2.28E-06	5.32E-08	0.003049	0.004930	0.7748	0.7989	0.7989	0.8980

**APPENDIX C. YIELD COMPARISON BETWEEN PREVIOUS AND CURRENT EXPERIMENTS**  
**(ZYA, 0.45 degree mosaic spread)**

Angle (degrees)	Prev. Yld.-NF (Buck./Ivey) (phot/elec)	Previous Tin Eff. Thick. (Buck./Ivey)	Corrected Tin Eff. Thick. (Buck./Ivey)	Omitted ZYA Atten. Fact. (Tin) (Buck./Ivey)	Atten. Fact. (Tin) (Buck./Ivey)	Corr. Yld-NF (wrt Buck/Ivy) (DiNova) (phot/elec)
20.10						5.13E-07
20.50	1.21E-06	0.04340	0.01164	0.7581	0.0264	
21.00	1.50E-06	0.04241	0.01161	0.7629	0.0287	
21.10						1.89E-06
21.50	3.29E-06	0.04147	0.01158	0.7675	0.0311	
21.60						4.23E-06
22.00	7.81E-06	0.04058	0.01155	0.7719	0.0335	
22.10						6.71E-06
22.25						
22.50	2.27E-05	0.03972	0.01152	0.7761	0.0360	
22.60						8.99E-06
22.75						
23.00	1.63E-05	0.03890	0.01149	0.7802	0.0385	
23.10						5.59E-06
23.25						
23.50	9.12E-06	0.03812	0.01146	0.7841	0.0412	
23.60						2.33E-06
23.75						
24.00	3.99E-06	0.03737	0.01143	0.7878	0.0438	
24.10						1.21E-06
24.25						
24.50	2.85E-06	0.03665	0.01140	0.7914	0.0465	
24.60						9.78E-07
25.00	1.56E-06	0.03597	0.01136	0.7949	0.0493	
25.60	1.18E-06	0.03518	0.01132	0.7989	0.0526	7.35E-07

**APPENDIX C. YIELD COMPARISON BETWEEN PREVIOUS AND CURRENT EXPERIMENTS**  
**(ZYA, 0.45 degree mosaic spread)**

Angle <b>(degrees)</b>	Corr. Yld-FF <b>(wrt Buck/Ivy)</b>	Corr. Yld-NF <b>(DiNova)</b>	Corr. Yld-NF <b>(phot/elec)</b>	Corr. Yield-FF <b>(wrt Barrows)</b>	Corr. Yield-FF <b>(DiNova)</b>	Corr. Yield-FF <b>(phot/elec)</b>	Corr. Yield <b>(wrt Barrows)</b>	Corr. Yield <b>(Buck./Ivey)</b>	Corr. Yield <b>(phot/elec)</b>	Yield-Far Fld <b>(Barrows)</b>	Yield-Far Fld <b>(Buck./Ivey)</b>	Yield-Far Fld <b>(phot/elec)</b>
20.10			1.97E-08									
20.50		2.46E-07					9.46E-09			7.27E-09		
21.00	3.78E-06	3.13E-07		7.29E-08		1.45E-07				1.20E-08		8.75E-09
21.50		7.05E-07										
21.60	9.19E-07		1.63E-07			3.53E-08				2.71E-08		1.69E-08
22.00		1.72E-06		2.58E-07		7.50E-08				6.60E-08		4.39E-08
22.10	1.95E-06											
22.25		5.11E-06		3.46E-07		3.11E-07				1.97E-07		7.72E-08
22.50											1.20E-07	
22.60	8.09E-06											
22.75												1.64E-07
23.00		3.76E-06		2.15E-07		2.60E-07				1.44E-07		
23.10	6.76E-06											
23.25												1.71E-07
23.50		2.15E-06								8.27E-08		
23.60	1.55E-06			8.98E-08		5.95E-08						
23.75												9.52E-08
24.00		9.61E-07										
24.10	7.60E-07		4.65E-08		2.92E-08					3.70E-08		
24.25												4.46E-08
24.50		7.01E-07									2.70E-08	
24.60	5.53E-07			3.76E-08		2.13E-08						
25.00		3.92E-07									1.51E-08	
25.60	2.05E-07	3.03E-07	2.83E-08	7.88E-09	7.88E-09	1.17E-08						

**APPENDIX C. YIELD COMPARISON BETWEEN PREVIOUS AND CURRENT EXPERIMENTS**  
**(ZYD, 1.31 degree mosaic spread)**

Angle <b>(degrees)</b>	Prev. Yld-NF <b>(Buck./Ivey)</b>	Previous Tin <b>Eff. Thickness</b> <b>(Buck./Ivey)</b>	Corrected Tin <b>Eff. Thickness</b> <b>(Buck./Ivey)</b>	Omitted ZYD <b>Atten. Fact.</b> <b>(Buck./Ivey)</b>	Corr Yield <b>(wrt Barrows)</b> <b>(Buck./Ivey)</b>	Yield-Far Fld <b>(phot/elec)</b> <b>(phot/elec)</b>
20.00	1.10E-06	0.04503	0.01168	0.7127	7.82E-09	
20.50	2.35E-06	0.04397	0.01165	0.7183	1.72E-08	6.24E-08
21.00	4.49E-06	0.04297	0.01163	0.7238	3.38E-08	2.69E-08
21.50	1.08E-05	0.04202	0.01160	0.7290	8.36E-08	4.94E-08
22.00	1.66E-05	0.04111	0.01157	0.7340	1.32E-07	9.08E-08
22.25						1.18E-07
22.50	1.90E-05	0.04024	0.01154	0.7388	1.55E-07	1.28E-07
22.75						1.34E-07
23.00	1.30E-05	0.03941	0.01151	0.7434	1.09E-07	
23.25						9.87E-08
23.50	8.34E-06	0.03862	0.01148	0.7479	7.13E-08	
23.75						5.93E-08
24.00	4.22E-06	0.03786	0.01145	0.7521	3.69E-08	
24.25						5.38E-08
24.50	1.83E-06	0.03714	0.01142	0.7563	1.64E-08	
25.00	1.04E-06	0.03644	0.01139	0.7602	9.50E-09	

**APPENDIX C. YIELD COMPARISON BETWEEN PREVIOUS AND CURRENT EXPERIMENTS**  
**(ZYH, 2.5 degree mosaic spread)**

Angle (degrees)	Prev. Yld-NF (Buck./Ivey)	Previous Tin (Buck./Ivey)	Corrected Tin (Buck./Ivey)	Omitted ZYH (Buck./Ivey)	Corr Yield (wt Barrows) (Buck./Ivey) (phot/elec)	Yield-Far Fld (Barrows)
20.00	3.85E-06	0.04561	0.01169	0.6940	2.63E-08	
20.50	3.53E-06	0.04455	0.01167	0.7000	2.49E-08	3.73E-08
21.00	7.31E-06	0.04353	0.01164	0.7057	5.31E-08	2.10E-08
21.50	1.12E-05	0.04256	0.01161	0.7111	8.36E-08	3.82E-08
22.00	9.79E-06	0.04164	0.01159	0.7164	7.51E-08	8.69E-08
22.25						1.11E-07
22.50	1.13E-05	0.04076	0.01156	0.7215	8.89E-08	1.35E-07
22.75						1.76E-07
23.00	8.80E-06	0.03993	0.01153	0.7263	7.10E-08	
23.25						2.57E-08
23.50	7.45E-06	0.03912	0.01150	0.7310	6.16E-08	
23.75						4.44E-08
24.00	5.14E-06	0.03835	0.01147	0.7355	4.35E-08	
24.25						8.44E-08
24.50	3.47E-06	0.03762	0.01144	0.7399	3.00E-08	
25.00	3.21E-06	0.03691	0.01141	0.7441	2.84E-08	
25.50	3.67E-06	0.03624	0.01138	0.7481	3.32E-08	



**APPENDIX D. TABLES OF EXPERIMENT AND THEORY INTENSITY RATIOS**  
 (ZYA, 0.45 degree mosaic spread)

0.45 Degree Mosaic Spread Intensity Ratio Data From Experiment and Theory						
Angle	Experiment Data	Experiment Data	Theory with Scattering	Theory without Scattering	Theory with Scattering	Theory without Scattering
(degrees)	N(2)/N(1)	N(3)/N(1)	N(2)/N(1)	N(2)/N(1)	N(3)/N(1)	N(3)/N(1)
20			0.702	0.708	0.411	0.415
20.5	0.364		0.756	0.772		0.462
21	0.379		0.86	0.969	0.526	0.612
21.5	0.291	0.2	0.972	1.24	0.61	0.844
22	0.609	0.313				
22.25	0.726	0.229	1.077	1.443	0.69	1.013
22.5	0.908	0.372				
22.75	0.929	0.418	0.972	1.24	0.61	0.844
23						
23.25	1.101	0.489	0.86	0.969	0.526	0.612
23.5						
23.75	0.854	0.349	0.756	0.772	0.449	0.462
24						
24.25	0.67	0.245	0.702	0.708	0.411	0.415
24.5			0.676	0.679	0.393	0.395
25			0.662	0.654	0.384	0.385
25.5						

Page 1 of 1

**APPENDIX D. TABLES OF EXPERIMENT AND THEORY INTENSITY RATIOS  
(ZYD, 1.31 degree mosaic spread)**

1.31 Degree Mosaic Spread Intensity Ratio Data From Experiment and Theory						
Angle (degrees)	Experiment Data	Experiment Scattering	Theory with Scattering	Theory without Scattering	Theory with Scattering	Theory without Scattering
	N(2)/N(1)	N(3)/N(1)	N(2)/N(1)	N(2)/N(1)	N(3)/N(1)	N(3)/N(1)
20			0.665	0.678	0.388	0.394
20.5			0.68	0.705	0.396	0.413
21	0.568		0.696	0.771	0.407	0.462
21.5	0.723	0.383	0.714	0.964	0.42	0.607
22	0.859	0.37	0.733	1.222	0.432	0.828
22.25	0.998	0.447				
22.5	0.98	0.44	0.75	1.422	0.443	0.991
22.75	1.181	0.532				
23			0.733	1.222	0.432	0.828
23.25	1.077	0.524				
23.5			0.714	0.964	0.42	0.607
23.75	0.759	0.366				
24			0.696	0.771	0.407	0.462
24.25	0.506	0.431				
24.5			0.68	0.705	0.396	0.413
25			0.665	0.678	0.388	0.394

**APPENDIX D. TABLES OF EXPERIMENT AND THEORY INTENSITY RATIOS**  
**(ZYH, 2.5 degree mosaic spread)**

2.5 Degree Mosaic Spread Intensity Ratio Data From Experiment and Theory						
Angle (degrees)	Experiment Data	Experiment $N(3)/N(1)$	Theory with Scattering	Theory without Scattering	Theory with $N(2)/N(1)$	Theory without $N(3)/N(1)$
20			0.657	0.679	0.678	0.395
20.5			0.671	1.44	0.39	1.004
21	0.71	0.289	0.814	0.777	0.473	0.464
21.5	0.561	0.218	0.665	0.969	0.386	0.611
22	0.811	0.323	0.668	1.246	0.39	0.835
22.25	0.894	0.409				
22.5	0.803	0.357	0.671	1.438	0.39	1.004
22.75	0.998	0.401				
23			0.668	1.246	0.39	0.835
23.25	0.594	0.221				
23.5			0.665	0.969	0.386	0.61
23.75	0.745	0.285				
24			0.814	0.777	0.473	0.464
24.25	0.852	0.266				
24.5			0.671	1.438	0.39	1.004
25			0.657	0.679	0.378	0.395
25.5			0.653	0.665	0.376	0.385

Page 1 of 1



## LIST OF REFERENCES

1. Fiorito, R.B., Rule, D.W., Maruyama, X.K., DiNova, K.L., Evertson, S.J., Osborne, M.J., Snyder, D., Rieydyk, H., Piestrup, M.A. and Ho, A.H., "Observation of Higher Order Parametric X-Ray Spectra in Mosaic Graphite and Single Silicon Crystals", Physical Review Letters, v.71, no.5, pp.704-707, August 1993.
2. Rule, D.W., Fiorito, R.B., Piestrup, M.A., Gary, C.K. and Maruyama, X.K., "Production of X-Rays by the Interaction of Charged Particle Beams with Periodic Structures in Crystalline Materials", paper no. 25 presented at SPIE's International Symposium on Optical Science and Engineering Conf. no. 1552 Short Wavelength Radiation Sources, San Diego, California, 21-26 July 1991.
3. Baryshevsky, V.G., Cherepitza, S.V., Danilov, V.A., Feranchuk, I.D., Safronov, P.F., Adishchev, Yu.N., Potylitzin, A.P., Vorobiev, S.A. and Pak, S.D., "Experimental Observation of Parametric X-Rays from Ultrarelativistic Electrons", J.Physics D: Applied Physics, v.19, pp.171-176, 1986.
4. Maruyama, X.K., DiNova, K.L., Snyder, D., Piestrup, M.A., Qiang, Li, Fiorito, R.B. and Rule, D.W., "A Compact Tunable X-Ray Source Based on Parametric X-Ray Generation by Moderate Energy LINACS", Particle Accelerator Conference, 17-20 May 1993, Washington, D.C.
5. Fiorito, R.B., Rule, D.W., Maruyama, X.K., Buckingham, W.M., Ivey, L.R. and Piestrup, M.A., "Absolute Spectral and Angular Distribution Measurements of Parametric X-Radiation in Graphite Crystals with Varying Degrees of Mosaicity", Proceedings of the 2nd International Symposium on Radiation from Relativistic Electrons in Periodical Structures, Sept. 4-8 1995, Tomsk, Russia.
6. DiNova, K.L., "Enhanced Higher Order Parametric X-Radiation Production", Masters Thesis, Naval Postgraduate School, Monterey, California, December 1992.
7. Buckingham, W.M. and Ivey, L.R., "Effects of Mosaicity On Parametric X-Radiation Production", Masters Thesis, Naval Postgraduate School, Monterey, California, December 1994.
8. Feranchuk, I.D. and Ivashin, A.D., "Theoretical Investigation of the Parametric X-Ray Features", J Physique, v.T46, no.11, pp. 1981-1986, November 1985.
9. Adishchev, Yu.N., Didenko, A.N., Mun, V.V., Pleshkov, A.P., Potylitsin, A.P., Tomchakov, V.K., Uglow, S.R. and Vorobiev, S.A., "Measurements of Parametric X-Rays from Relativistic Electrons in Silicon Crystals", Nuclear Instruments and Methods in Physics Research, v.B21, pp.49-55, 1987.

10. Cullity, B.D., Elements of X-Ray Diffraction, 2nd Edition, Addison-Wesley Publishing Company, Inc., 1978.
11. FAX on UCAR Graphite Monochromators from Advanced Ceramics Corporation, Lakewood, OH, January 1994.
12. The Nucleus, Inc., "Personal Computer Analyzer Series II", copyright 1992.
13. Jandel Scientific, "PeakFit v3.10", S/N 601101, copyright 1989-1991 by AISN Software.
14. Applied Inventions Corporation, "PhotCoef", S/N 19304061, copyright 1989-1993.
15. Experimental Calculations provided by R.B. Fiorito, Naval Surface Warfare Center, Silver Spring, Maryland, October 1995.
16. Canberra Instruction Manual, Si(Li) Detector System Series 7300, S/N 1191404, revised January 1991.
17. Cullen, D.E., Chen, M.H., Hubbell, J.H., Perkins, S.T., Plechaty, E.F., Rathkopf, J.A. and Scofield, J.H., Tables and Graphs of Electron-Interaction Cross Sections from 10 eV to 100 GeV, Lawrence Livermore National Laboratory, October 1989.
18. Microsoft Excel, "Microsoft Office v4.2.1", copyright 1983-1995.
19. Osborne, M.J., "Higher Order Parametric X-Rays", Masters Thesis, Naval Postgraduate School, Monterey, California, December 1991.
20. Fiorito, R.B., Rule, D.W., Piestrup, M.A., Maruyama, X.K., Silzer, R.M., Skopik, D.M. and Shchagin, A.V., "Polarized Angular Distributions of Parametric X-Radiation and Vacuum-Ultraviolet Transition Radiation from Relativistic Electrons", Physical Review Letters, v.51, no.4, pp 2759-2762, April 1995.
21. Berger, M.J. and Hubbell, J.H., "XCOM: Photon Cross Sections on a Personal Computer", National Bureau of Standards and Technology, NBSIR 87-3597, Gaithersburg, Maryland, 1987.
22. Borland International, "QuattroPro v4.0" software, copyright 1992.

## INITIAL DISTRIBUTION LIST

1. Defense Technical Information Center.....2  
8725 John J. Kingman Rd., STE 0944  
Ft. Belvoir, VA 22060-6218
2. Dudley Knox Library.....2  
Naval Postgraduate School  
Monterey, California 93943-5101
3. Mr. D. Snyder, Code 61PH.....1  
Department of Physics  
Naval Postgraduate School  
Monterey, California 93943-5002
4. Mr. H. Rietdyk, Code PH.....1  
Department of Physics  
Naval Postgraduate School  
Monterey, California 93943-5002
5. Dr. X.K. Maruyama, Code PH/MX.....5  
Department of Physics  
Naval Postgraduate School  
Monterey, California 93943-5002
6. CDR R.M. Harkins, Code PH/Hr.....1  
Department of Physics  
Naval Postgraduate School  
Monterey, California 93943-5002
7. LT J.E. Barrows, USN.....2  
P.O. Box 872  
Hereford, Arizona 85615
8. Dr. R.B. Fiorito, Code R36.....1  
Naval Surface Warfare Center  
10901 New Hampshire Avenue  
Silver Spring, Maryland 20903-5000
9. Dr. M.A. Piestrup.....1  
2181 Park Boulevard  
Palo Alto, California 94306